Use of Thermal Analysis to Control the Solidification Morphology of Nodular Cast Irons and Reduce Feeding Needs

Von der Fakultät für Ingenieurwissenschaften der Universität Duisburg-Essen,
Abteilung Maschinenbau und Verfahrenstechnik
zur Erlangung des akademischen Grades

eines

Doktors der Ingenieurwissenschaften

Dr.-Ing.

genehmigte Dissertation

von

Vitor Emanuel Azevedo dos Anjos
aus
Porto (Portugal)

Gutachter: Univ.-Prof. Dr.-Ing. Rüdiger Deike

Prof. Dr. Eng°. Carlos Ribeiro (Universität Porto – Portugal)

Tag der mündlichen Prüfung: 22 Juli 2015

Preface

The work presented in this thesis started to be developed in 2011, at the Faculty for Engineering of the University of Duisburg-Essen in the Department of Mechanical and Process Engineering and at my employer, the company OCC GmbH.

The thesis focus on the determination of the real solidification morphology of nodular cast iron melts, determined through the use of thermal analysis technic, and its relation with the potential to avoid or minimize the occurrence of volume contraction defects.

The inspiration for this thesis work, resulted from the working experience that I've had on service for OCC GmbH through the years, providing consultancy service for many German and foreign foundries. The experimental work was performed both in Germany and Portugal.

Naturally, during this three year of development of this thesis work, simultaneously with my work obligation to OCC GmbH, there are many influence personalities to thank for.

It is the greatest honour to be able to work under the supervision of Prof. Dr.-Ing. Rüdiger Deike. It was an honour that he accepted the application and supervision of this project. I would like to thank Prof. Deike for all the availability, guidance, help and assistance on providing means and advices to the enrichment of this work.

This work would not be possible without the support from my employee. OCC GmbH is driven by the continuous research and development of new products and innovative concepts to provide cutting head technology equipment and softwares to the foundries. Following this philosophy, they have given me all the assistance needed to perform this work. I, therefore, would like to thank to all my working colleagues and specially the two managing directors and my friends, Diplom-Physiker Wolfgang Baumgart and Ulrich Jantzen. Also from OCC GmbH, a special thanks to my fellow metallurgists Joao Cunha and Francisco Costa Lopes, for the long brain-storming sessions and share of field experiences.

The performance of all trials here presented, was only possible due to the interest and participation of some of the most respectable foundries in Germany and Portugal. From Germany, I would like to thank to the foundry Heidelberger Druckmachinen AG in Amstetten, especially to Dipl.-Ing. Christian Knigge and B.Eng.(FH) Florian Nusser and also to the foundry ACO Passavant Guss GmbH in Aarbergen, specially to Dipl.-Ing. Ingo Schmidt and Dipl.-Ing.

Giacomo Piantoni. From Portugal, I thank to the foundry DuritCast SA in Águeda, especially to Eng. Antonio Esteves, Eng. Rogerio Lopes, Eng. Pedro Cardoso, Eng. André Ribeiro and Eng. André Afonso.

I thank also to two young engineers, Eng. Joao Teixeira and Eng. Carlos Gomes, for their hard work on the participation of the execution of some of the trials and sample preparation.

My deepest thanks go also to Prof. Dr. Carlos Silva Ribeiro from the Faculty of Engineering of the Porto University in Portugal, firstly for accepting the invitation to be one of the reviewer of this thesis, and ultimately for being the person that guide me to the foundry field when I was still his student, for introducing me to OCC GmbH for my first job and for all the support given to me in the planning and execution of the trials performed in Portugal.

Above all, I would like to thank to my entire family, for being my support through all moment of my live and being always available, particularly to my parents Victor Anjos and Ana Maria Anjos, to my dear sister Ana Luisa.

My final grateful note goes to Juliana and Kratos, for all the support, love and above all, for choosing to share with me this amazing experience that is life!

Duisburg, 2015

Abstract

The production of nodular graphite cast iron, is gaining more volume in the global foundry production.

Foundries, very often face complicated casting defects, such as shrinkage and porosity defects, that are often difficult to predict during production but their origin is often associated with process variation of parameters that are not measured, and therefore, not controlled. Also, foundry personnel often use in practice, theoretical concepts that were formulated and are valid in very special conditions, but not exactly match the real foundry conditions. Foundry often struggle with shrinkage and porosity defects that apparently appear randomly in the castings, because some influential changes in the solidification morphology of the melt occurred and was not detected.

One method to overcome some of the limitations of more conventional process control tools such as spectrometer, wedge test and fast metallographic melt sample analysis, is the implementation of thermal analysis technics.

The correct use of thermal analysis technics can provide useful information on the melt's real solidification characteristic, within 1 to 2 minutes in the most modern equipment.

In this work, the real solidification morphology of several melts of nodular graphite cast iron were measured using thermal analysis technic to establish a supported parallelism between the morphology of the cooling curve and the real solidification morphology of the melt, regardless of the theoretical concept of Carbon Equivalent established by the Fe-C equilibrium phase diagram. Process parameters that often cause the change in the melts solidification morphology such as the carbon content and the inoculation quality of the melt were manipulated.

The validation of the correspondence between the solidification curve characteristic points and the real solidification morphology of the melt was made through the performance of quenching tests and microstructure observation using colour metallography. The results revealed that the solidification morphology of the melt is not correctly traduced by the C.E. value calculated based on the Carbon and Silicon content of the melt, due to other process variables that directly affect solidification. Nevertheless, using thermal analysis the effect of those process variables can be seen and the real solidification morphology of the melt determined.

This work includes also an adaptation of technics usually used in Aluminium alloys to estimate the occurrence of the dendritic coherency point and the influence that liquidus temperature has on the dendritic growth of austenite dendrites. Through thermal analysis it is possible to estimate if a given melt will have tendency to form a long and branched dendritic structure or not, depending on the solidification morphology of the curve and the liquidus temperature. Lower liquidus temperature proves to result in lower developed dendritic structures.

All these concepts on control of the melts solidification structure and control on the dendritic growth development were tested in real foundry conditions to determine what real solidification morphology, maximizes the expansion properties of the nodular cast iron melt and therefore reduces the feeding requirements. Results show that hypoeutectic solidification morphologies for high carbon contents (with C.E. higher than the given from the equilibrium phase diagram for eutectic compositions) and eutectic solidification morphologies are effectively the ones where the self-feeding properties of the melt in a casting are maximized.

Kurzfassung

Die Produktion von Gusseisen mit Kugelgraphit gewinnt immer mehr Bedeutung in der globalen Gusseisenproduktion.

Gießereien stehen dabei oft Problemen mit Gussfehlern, wie Schrumpfungen und Porositäten gegenüber, die in der Produktion nur schwer vorhersehbar sind, aber deren Ursprünge oftmals mit der Variation der Prozessparameter zusammenhängen, welche nicht gemessen werden und daher nicht kontrolliert werden können. Außerdem benutzt das Gießereipersonal in der Praxis häufig theoretische Konzepte, die für spezielle Bedingungen entwickelt und gültig sind, aber nicht exakt zu den realen Gießereibedingungen passen. Dabei kämpfen Gießereien oft mit Schrumpfungs- und Porositätenfehlern, die scheinbar zufällig in den Gussteilen auftauchen, weil einige maßgebende Änderungen in der Erstarrungsform der Schmelze stattfinden, die nicht erkannt werden.

Eine Methode, die begrenzten Möglichkeiten der konventionellen Prozessüberwachungswerkzeuge, wie Spektrometer, Gießkeiltest und schnelle metallurgische Schmelzprobenanalyse zu überwinden, ist die Implementierung einer optimierten thermischen Analyse.

Die korrekte Anwendung der Thermoanalyse mit modernen Messsystemen liefert wertvolle Informationen der Erstarrungscharakteristik einer Schmelze innerhalb von ein bis zwei Minuten.

In dieser Arbeit wurden für Gusseisen mit Kugelgraphit die realen Erstarrungsmorphologien verschiedener Schmelzen unter Verwendung der thermischen Analyse untersucht, um dabei Parallelen zwischen der Form der Abkühlkurven und der wahren Erstarrungsform der Schmelze zu erhalten, ungeachtet des theoretischen Konzeptes des Kohlenstoffäquivalentes (C.E.), welches sich aus dem Fe-C Gleichgewichtsphasendiagrammes ergibt. Prozessparameter, die hauptsächlich die Erstarrungsform der Schmelze beeinflussen, wie Kohlenstoffgehalt und die Qualität der Impfung, wurden variiert.

Die Überprüfung der Übereinstimmung zwischen charakteristischen Punkten der Abkühlkurve und der wahren Erstarrungsform der Schmelze erfolgte mittels Abschrecktests und Gefügeuntersuchungen durch Farbätzung-Metallographie. Die Ergebnisse zeigten dabei, dass wegen anderer Prozessvariablen, die die Erstarrung direkt beeinflussten, sich die Erstarrungsform

der Schmelze nicht genau aus dem C.E.-Wert ableiten ließ, der sich aus der Berechnung an Hand des Kohlenstoff- und Siliziumgehaltes der Schmelze ergab. Ungeachtet dessen konnten die Effekte dieser Prozessvariablen durch Verwendung der Thermoanalyse erkannt werden und damit die wirkliche Erstarrungsform der vorliegenden Schmelze vorhergesagt werden.

Diese Arbeit enthält außerdem eine Anpassung der Thermoanalyseanwendung, die gewöhnlich bei Aluminiumlegierungen zur Erstarrungsvorhersage (dendritic coherency point) verwendet wird und den Einfluss beschreibt, den die Liquidustemperatur auf das Dendritenwachstum von austenitischen Dendriten hat. Mit den Ergebnissen der Thermoanalyse ist eine Vorhersage möglich, ob eine gegebene Schmelze tendenziell ein lange, verzweigte Dendritenstruktur bildet, abhängig von der Form der Temperaturkurve der Erstarrung und der Liquidustemperatur. Eine geringere Liquidustemperatur erweist sich dabei als Ursache für geringer entwickelte Dendritenstrukturen.

Die hier vorgestellten Konzepte zur Kontrolle der Erstarrungsstruktur und der Entwicklung des Dendritenwachstums einer Schmelze wurden unter realen Gießereibedingungen getestet, um festzustellen, welche reale Erstarrungsform die Expansionseigenschaften einer Sphärogusseisenschmelze maximiert, so dass der Speiserbedarf reduziert werden kann. Die Ergebnisse zeigen, dass untereutektische Erstarrungsformen für hohe Kohlenstoffgehalte (mit C.E.-Werten höher als der Wert für die eutektische Zusammensetzung im Fe-C Gleichgewichtsdiagramm) und eutektische Erstarrungsformen diejenigen sind, bei denen die selbstspeisenden Eigenschaften einer Schmelze beim Gießen maximal sind.

Index

1. Prelude

The production of nodular graphite cast iron is growing on a world wide scale, proving that its advantages and properties are in demand in nowadays industry structure.

Therefore is natural that foundries increase their production of castings in these alloys and some foundries start now to include these alloys in their offer to the market.

Nevertheless, production of nodular graphite cast iron as some particularities that often make its production complex. One of those particularities is the higher tendency to the appearance of shrinkage and porosity defects in the castings. These is in fact one of the most concerning problem for the producers, that often struggle to keep the problem under control.

The appearance of these shrinkage and porosity problem is often of complex determination, because sometimes they are a consequence of more than one parameter, and possibly some of the influent parameters is not controlled property or not controlled at all. Therefore, the process control of as many process variables possible is required.

Very often in foundries, melt quality evaluation is performed using chemical analysis of the composition of the different elements of the melt, that although vital for the process control, does not give all real needed information on thermodynamic and kinetic properties of the melt that can only be determined if the solidification of the melt is analysed. More traditional methods such as a fast metallographic sample and wedge test, can give additional information, but that information is not centralized, requires several sample preparation procedures, is time consuming and still do not provide all relevant melt quality information.

One way to have a more accurate evaluation of the melt quality is through the study of the solidification curve of a sample from the melt. The solidification curves are the basis for the construction of the equilibrium phase diagram, and also for the Fe-C equilibrium diagram used often in cast iron foundries. The solidification curve is sensitive to the melt's thermodynamic and kinetics characteristics, providing therefore relevant information that is not available in traditional test methods. Nevertheless, often foundries use the Fe-C equilibrium phase diagram to predict the solidification morphology of the melt based on the Carbon, Silicon, and sometimes

also Phosphor, ignoring that the equilibrium phase diagram was obtained for equilibrium conditions that do not exist in real foundry conditions. This results in assumption regarding the melt quality and solidification behaviour suggested by the equilibrium diagrams that are not verified in reality.

The solidification morphology of the melt is of extreme importance, once the relative order of solidification of the different phases, their morphology and amount will influence the final casting quality and appearance of shrinkage and porosity defects. Special attention must be given to the solidification sequence of graphite particles, due to the expansion that they give when solidify (due to the low density) and the influence that this phenomenon has to compensate the natural shrinkage of the iron when it solidifies.

Thermal analysis technic, through the evaluation of the solidification curve of a melt's sample, allows the observation of the real solidification morphology of the melt during production. This is vital information for the evaluation of the melt quality and also to the active correction of the melt during processing, once the evaluation of the melt quality through this technics take only a few minutes.

So, in order to take advantage of this technic for a improved process control, it is necessary to make a serious study of the solidification curve morphology and characteristic points to correlate them with important solidification characteristics of the melt that have impact on shrinkage and porosity defects, such as moment of precipitation and growth of graphite, dendritic structure development, time of dendritic coherency point, among others.

2. Motivation and Objectives

The motivation for the executions of this work rose from the first years of experience in the use and implementation of thermal analysis technics. During the implementation of the thermal analysis technics, at customers that had difficulties controlling shrinkage and porosity defects in castings, often it was questioned about what is the best melt quality to avoid shrinkage and reduce feeding needs. Very often this question could not be answered in an exact way and often the answer was like "it depends on the casting geometry and on the type nature of sand mould resistance that you use". Although the answer is true, often this was not the answer the customers were expecting to their question.

What they really wanted to know was simply what should the melt characteristics and solidification morphology be for them to have a melt with the lowest feeding needs possible, for then to use it as a starting point to afterwards adjust feeding and gating systems.

Very often in application of thermal analysis technics in foundries to improve the process control and its stability, it has been experienced that some foundries follow strictly the equilibrium phase diagram to predict the solidification morphology of the melt, regardless of the facts that the equilibrium diagram was obtained in different conditions to the ones in the real foundry and the fact that inoculation conditions are also not taken in account in the diagram. Furthermore, important variables such as the liquidus temperature and the undercooling of the melt are not properly corrected during process as they change from ladle to ladle, even if they came from the same base iron melt. Often no carbon correction is done to compensate the fading of carbon in the base iron melt or no adjustments are done of the inoculation addition in the ladle to compensate also the changes of the inoculation of the melt for extended holding times and temperatures of the base melt in the furnaces. In general foundries are not aware of the impact that some important variables such as inoculation has in the real solidification morphology of the melt.

Taking these work experiences in account and knowing the potentialities of the use of thermal analysis techniques, the objective of this thesis is to demonstrate how to predict the real solidification morphology of the melt in foundry conditions, beyond the normal use of equilibrium phase diagram, with special attention to the effect of inoculation, using thermal

analysis. Also an objective is to explore and demonstrate how solidification morphology can affect the feeding requirement or maximize the expansion due to graphite growth during solidification.

The purpose of this work is to make a contribution to scientific knowledge and simultaneously to provide information that can be useful for foundries to improve their process control strategies and optimize the process efficiency.

3. State of Knowledge

3.1. Characterization of nodular cast iron

Ductile cast iron is a ferrous alloy material, with a wide range of applications in the past, present and future times.

The use of cast iron alloys to produce castings began approximately 2500 years ago according to registers that indicate that the earliest dated iron casting is that of a lion figure produced in China in approximately 600 B.C., found in Luhe County – Jiangsu [1] [2]. The production of cast iron in industrial amounts, started only on the beginning of the 18th century at Coalbrookdale in England [3].

Nowadays, the use of cast iron is of primordial importance to the industry in different fields of application that range from automotive and nautical, mechanical power, transmission equipment, industrial equipment and machinery, energy generators, among others [3].

Cast iron alloys are composed principally by Iron (Fe), Carbon (C) and Silicon (Si), where carbon content is higher than the maximum amount that can be retained in solid solution in Austenite[1] at the eutectic temperature transformation. Other alloying elements such as, for example, Phosphor (P), Sulphur (S), Manganese (Mn), Copper (Cu), Tin (Sn), Nickel (Ni) and Chromium (Cr) are also used to manipulate the mechanical and corrosion properties of the material. Same other elements found in the melt, such as Bismuth (Bi), Antimony (Sb), Calcium (Ca), Titanium (Ti), etc, are present as trace or residual elements with origin on the charge materials used to elaborate the cast iron melt.

At the eutectic transformation from cast iron alloys, the carbon content that exceeds the maximum content possible to dissolve in the austenite, will precipitate in the form of graphite[2]

[1] Austenite (g-Iron) – Metallic allotropic form of iron, with a face-centered cubic crystal structure, exists normally in cast iron alloys only above the 727°C (eutectoide temperature). Can be present at room temperature in case of some especially alloyed melts. It solidifies from liquid alloy in dendrite form or surrounding the graphite particles. Soft and ductile, approximately 200 HB [15]

[2] Graphite - Free carbon; soft; improves machinability and damping properties; reduces shrinkage and may reduce strength severely, depending on shape [15].

for the stable eutectic solidification and as cementite [3] (Fe_3C) in the case of metastable solidification [3].

Cast irons are classified in two main groups, according to the solidification morphology of carbon, being classified as White Cast Iron when carbon solidifies as cementite (Fe_3C) and Grey Cast Iron when carbon solidifies as graphite. Within the grey cast iron class, there is still a classification according to the shape of the graphite particles that form during solidification, being classified as:

- Lamellar Graphite Cast Iron (also denominated simply as grey iron);
- Nodular Graphite Cast Iron (also denominated Ductile Iron or Spheroidal Graphite Cast Iron);
- Compacted Graphite Cast Iron (also denominated Vermicular Graphite Cast Iron);
- Malleable Iron

The classification of the graphite particle form in cast iron follows the norm DIN-EN-ISO 945-1:2008, where the possible shapes of the graphite particles are presented and divided into 6 groups, as presented in **Figure 1**.

From the DIN-EN-ISO945-1:2008, the Form-I and Form-II correspond to lamellar graphite cast iron. Form-III is the one from compacted graphite cast iron, although it can also be found in nodular cast irons with low magnesium contents. Form-IV represents the typical graphite shape from malleable irons. Form-V corresponds to a graphite shape found often in nodular cast iron, when the magnesium content is slight low or the melt is bad inoculated. Form-VI corresponds to the graphite shape typical for nodular cast irons [4].

[3] Cementite (Fe_3C) – Iron carbides. Complex orthorhombic crystal structure. Hard, intermetallic phase, 800–1400 HV depending upon substitution of elements for Fe; imparts wear resistance; reduces machinability [15].

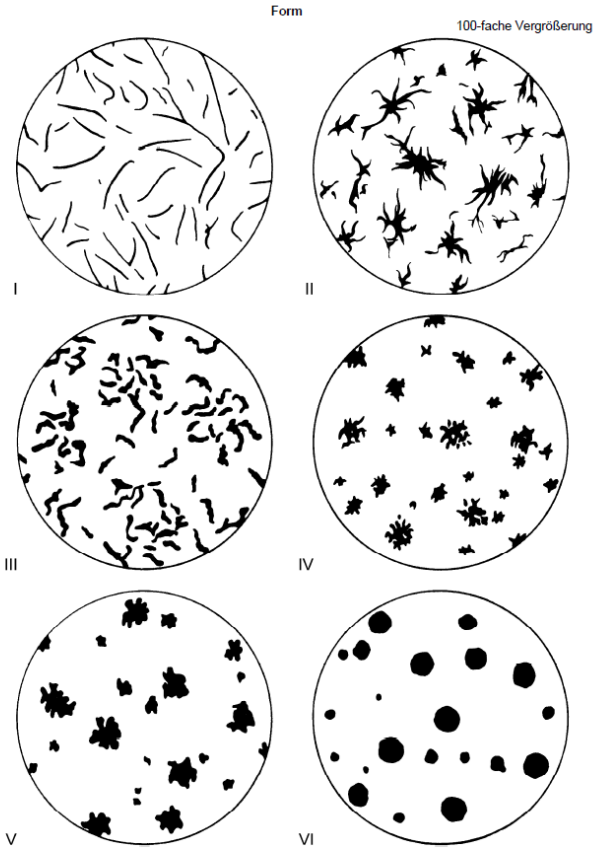

Figure 1 - Classification of the graphite particle shape from cast iron, according to the norm DIN-EN-ISO 9445-1:2008.

Nodular cast iron was first reported by C. Adey (RWTH Aachen) in 1937, and until then only "grey cast iron" (lamellar graphite cast iron) was produced industrially (apart also from white cast iron). The industrial production of nodular cast iron started approximately only 65 year ago in the USA, Canada and Great-Britain [5].

According to cast iron production data, for the year of 2012, provided by the *"47th Census of World Casting Production"*, cast iron products represent approximately 72% from all castings produced worldwide. In case of nodular cast iron, it represents 25,0% from total castings production [6]. The nodular cast iron production, for the time period of 2006 to 2012, increased in average 4,2% per year, reaching in 2012 a production volume of 25,17 million metric tonnes. This evolution tendency for nodular cast iron is presented in **Figure 2** [7-14].

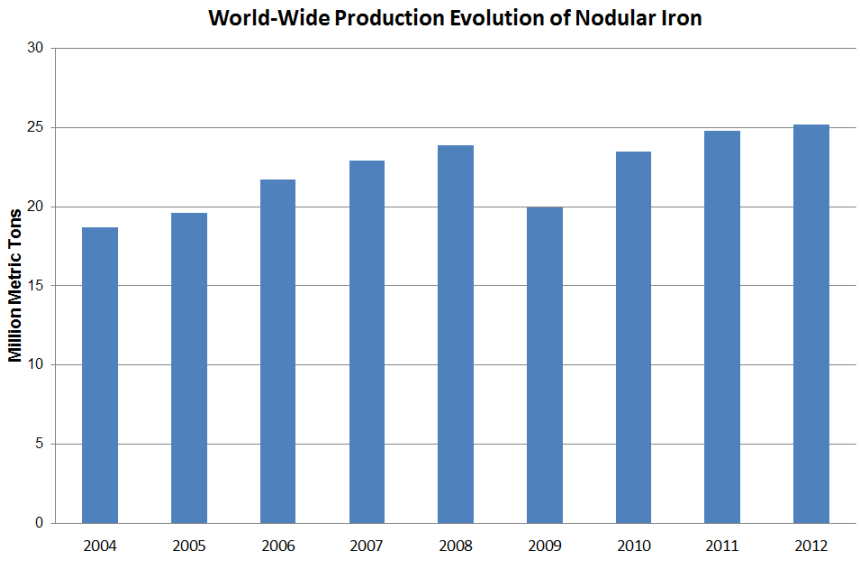

Figure 2 – Nodular cast iron production evolution world-wide from 2004 until 2012.

Nodular cast iron is characterized by having carbon in the shape of spheres, distributed across the iron matrix (see **Figure 3**) [15]. **Figure 3.b** shows a detailed observation of a graphite nodule, using SEM[4], where the spherical shape of the graphite particle is visible and also that no physical connection between the graphite particle and the matrix exists.

The size and number of graphite particle depends greatly on the solidification time and thickness section of the castings [3] (see **Figure 4**) but also in the inoculation properties of the melt [16].

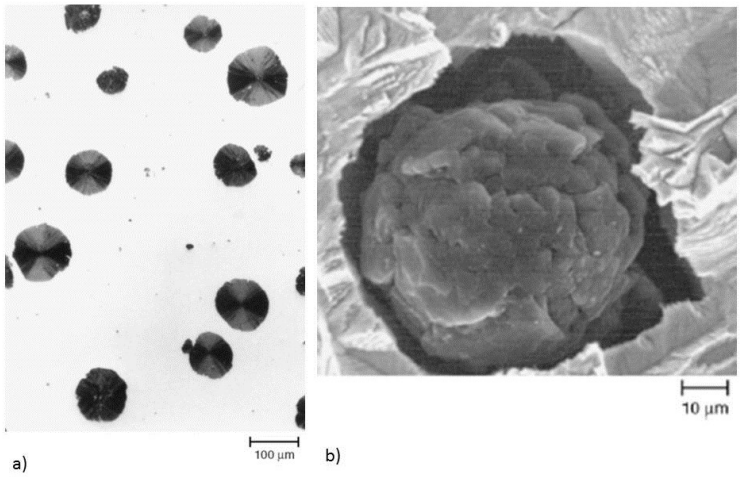

Figure 3 –a) As-cast ductile iron. As-polished; b) Nodular graphite in as-cast ductile iron examined with SEM. Sample was deeply etched with 50% HCl [15].

[4] SEM – Scanning Electron Microscopy

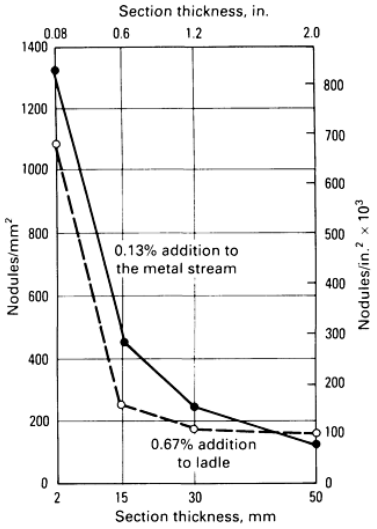

Figure 4 – Number of nodular graphite particles in ductile irons inoculated with standard foundry grade ferrosilicon (75% Si) added either to the ladle or to the metal stream [3].

The matrix of nodular cast iron can be formed by 100% ferritic[5] to 100% pearlitic[6] (see **Figure 5**). Like in other cast iron alloys, the nature of the matrix depends on the addition of alloying elements (such as Cu and Sn to increase the pearlite content), cooling speed or wall thickness (higher cooling rates increase the pearlite content) and graphite particle density (higher graphite particle density increase the amount of ferrite) [3] [15].

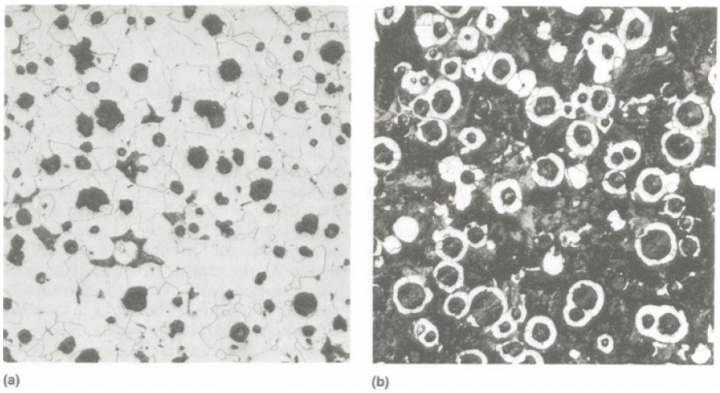

Figure 5 - Microstructures of nodular cast iron, etched with Nital. (a) As-cast ferritic. (b) As-cast pearlitic [15].

[5] Ferrite - Body-centered cubic crystal structure of iron with elements in solid solution, which is a stable equilibrium, low-temperature phase. Soft, 80–90 HB; contributes to high ductility but lower strength [15].
[6] Pearlite - A metastable lamellar aggregate of ferrite and cementite due to eutectoid transformation of austenite. Contributes to increase strength without brittleness; has good machinability and approximately 230 HB [15].

The mechanical properties are particularly attractive if higher strength and ductility is desired for a given application. According to the norm DIN EN 1563:2012-03 (see **Table 1**), lowest class for nodular cast iron is the GJS-350-22 with a tensile strength of 350MPa and 22% of elongation (fully ferritic matrix) and the highest class is the GJS-900-2 with a tensile strength of 900MPa and 2% of elongation (fully pearlitic matrix) [17]. Although the tensile strength depends on the matrix nature (ferritic/pearlitic) also the shape of the graphite particles has a strong impact on the final resistance of the material. As the graphite particles start to lose their spherical shape (also denominated by nodularity at image analysis reports) and start to get irregular (see **Figure 6**; more graphite Form V and even Form III) the tensile strength starts to decrease and the performance of the casting is compromised (see **Figure 7**) [3].

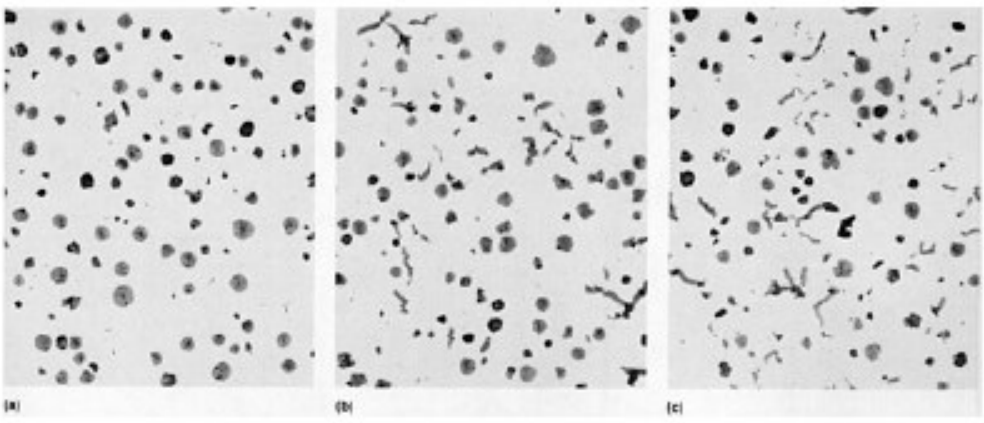

Figure 6 - Microstructures of nodular cast irons of varying nodularity. (a) 99% nodularity. (b) 80% nodularity. (c) 50% nodularity. All un-etched. Magnification of 36× [3].

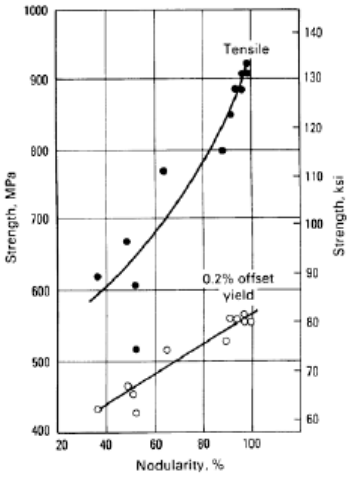

Figure 7 - Tensile and yield strength of ductile iron versus visually assessed nodularity [3].

Nevertheless, despite this increase in strength, nodular cast iron has low thermal conductivity when compared with lamellar and compacted cast iron that limits its applications for parts that require rapid and constant cooling such as motor blocks and cylinder heads. The thermal conductivity in nodular cast iron ranges only from 33,5W/m•K to 36,5 W/m•K, while in lamellar cast iron typically ranges from 45,3 W/m•K to 65,7 W/m•K (values for tests conducted at 100°C) [3].

Table 1 - Main mechanical properties from tensile strength test for the different grades of Nodular cast iron according to the norm DIN EN1563:2012-03.

Werkstoffbezeichnung		Maßgebende Wanddicke	0,2 %-Dehn-grenze	Zugfestigkeit	Dehnung
		t	$R_{p0,2}$	R_m	A
		mm	MPa	MPa	%
Kurzzeichen	Nummer		min.	min.	min.
EN-GJS-350-22-LT [a]	5.3100	$t \leq 30$	220	350	22
		$30 < t \leq 60$	210	330	18
		$60 < t \leq 200$	200	320	15
EN-GJS-350-22-RT [b]	5.3101	$t \leq 30$	220	350	22
		$30 < t \leq 60$	220	330	18
		$60 < t \leq 200$	210	320	15
EN-GJS-350-22	5.3102	$t \leq 30$	220	350	22
		$30 < t \leq 60$	220	330	18
		$60 < t \leq 200$	210	320	15
EN-GJS-400-18-LT [a]	5.3103	$t \leq 30$	240	400	18
		$30 < t \leq 60$	230	380	15
		$60 < t \leq 200$	220	360	12
EN-GJS-400-18-RT [b]	5.3104	$t \leq 30$	250	400	18
		$30 < t \leq 60$	250	390	15
		$60 < t \leq 200$	240	370	12
EN-GJS-400-18	5.3105	$t \leq 30$	250	400	18
		$30 < t \leq 60$	250	390	15
		$60 < t \leq 200$	240	370	12
EN-GJS-400-15	5.3106	$t \leq 30$	250	400	15
		$30 < t \leq 60$	250	390	14
		$60 < t \leq 200$	240	370	11
EN-GJS-450-10	5.3107	$t \leq 30$	310	450	10
		$30 < t \leq 60$	ist zwischen Hersteller und Käufer zu vereinbaren		
		$60 < t \leq 200$			
EN-GJS-500-7	5.3200	$t \leq 30$	320	500	7
		$30 < t \leq 60$	300	450	7
		$60 < t \leq 200$	290	420	5
EN-GJS-600-3	5.3201	$t \leq 30$	370	600	3
		$30 < t \leq 60$	360	600	2
		$60 < t \leq 200$	340	550	1
EN-GJS-700-2	5.3300	$t \leq 30$	420	700	2
		$30 < t \leq 60$	400	700	2
		$60 < t \leq 200$	380	650	1
EN-GJS-800-2	5.3301	$t \leq 30$	480	800	2
		$30 < t \leq 60$	ist zwischen Hersteller und Käufer zu vereinbaren		
		$60 < t \leq 200$			
EN-GJS-900-2	5.3302	$t \leq 30$	600	900	2
		$30 < t \leq 60$	ist zwischen Hersteller und Käufer zu vereinbaren		
		$60 < t \leq 200$			

ANMERKUNG Die mechanischen Eigenschaften der Proben, die aus gegossenen Probestücken durch mechanische Bearbeitung hergestellt wurden, können von den mechanischen Eigenschaften des eigentlichen Gussstückes abweichen. Richtwerte der Eigenschaften dieser Sorten bei Zugbeanspruchung sind im Anhang B angegeben.

[a] LT für tiefe Temperaturen.

[b] RT für Raumtemperatur.

3.2. Production of nodular cast iron

The production of nodular cast iron can be performed using different melting and pouring methods, depending on the availability and costs of raw materials, environmental legislations, production volume requirements, casting size and available technology.

3.2.1. Base iron melt preparation

Melting is usually performed using medium frequency electrical induction furnaces for medium to low production volumes. The base iron charge composition for these types of furnaces to produce nodular cast iron are normally composed by steel scrap, special-quality pig-iron supplied for nodular iron production (S<0,03%, P<0,08%, Mn<0,5% or lower depending on the pig-iron grade) and nodular cast iron returns.

For high production volumes, cupola melting furnaces are used. Due to the requirement of low sulphur content for the base iron melt (S<0,02%), it is are normally subjected to a desulphurization step that can use calcium carbide (CaC_2) added to a treatment ladle as lumps or magnesium (pure Mg or FeSiMg alloys with high Mg content) that can be added as lumps or as wire [3].

Nevertheless, Sulphur content in the base iron melt (or after desulfurization in the case of cupola furnace melts) should not be below 0,008% [18].

The chemical composition of the base iron melt is than adjusted to the desirable grade through the addition of alloying elements, such as Cu, Sn, Mn, Si, among other. Lower grades of nodular cast iron, according to the DIN EN 1563:2012-03 such as the GJS350-22 to GJS450-10 should have a ferritic matrix and therefore low content of Cu and Sn. Grades that should have a fully pearlitic matrix have high content of Cu (up to 0,9%) eventually also Sn (up to 0,09%).

3.2.2. Nodularization treatment

The production of nodular cast iron requires a content of magnesium, when pouring, between 0,04% to 0,06%. To achieve this Mg content in the melt, a modification treatment is performed to the melt after tapping it from the melting furnace or the holding furnace. This modification treatment (also called nodularization or simply Mg-treatment) consists in the addition of Mg to reduce the O and S content in the melt and to achieve a desirable content of Mg to promote the growth of the graphite particles with a nodular shape and therefore obtain nodular cast iron.

Typical compositions of Mg-alloys for melt treatment are presented in **Table 2**.

Table 2 - Magnesium content of treatment materials [19].

Alloy Type	Mg Content
Mg-Fe-Si alloy	3-20%
Ni-Mg alloy	5-15%
Mg ingot	>99%
Mg-Fe briquettes	5-15%
Cored wire	40-95%

In processes where the base iron melt is produced using a cupola furnace, often the desulfurization process and nodularization process are performed simultaneously. This technique is applied often using a Georg Fischer converter (see **Figure 8**), where metallic magnesium is used to make the melt desulfurization and modularization simultaneously. Due to the high amount of magnesium added, and the fact that the melt's temperature when Mg is added is higher than the Magnesium's boiling temperature (Mg boiling temperature is 1090°C; melt temperature when Mg is added ranges between 1420°C up to 1520°C depending on the process and casting to be produced) the reaction will be very violent due to the magnesium vaporization and vigorous burn in contact with air. [3] For that reason a converter is used to ensure the safety of the process. Wire-treatment can also be used for desulfurization, where a cored wire containing a FeSiMg alloy with high Mg content is used. A treatment machine cabinet is used to perform treatment where a ladle-cover is positioned over the ladle to avoid or minimize splashing of melt during treatment.

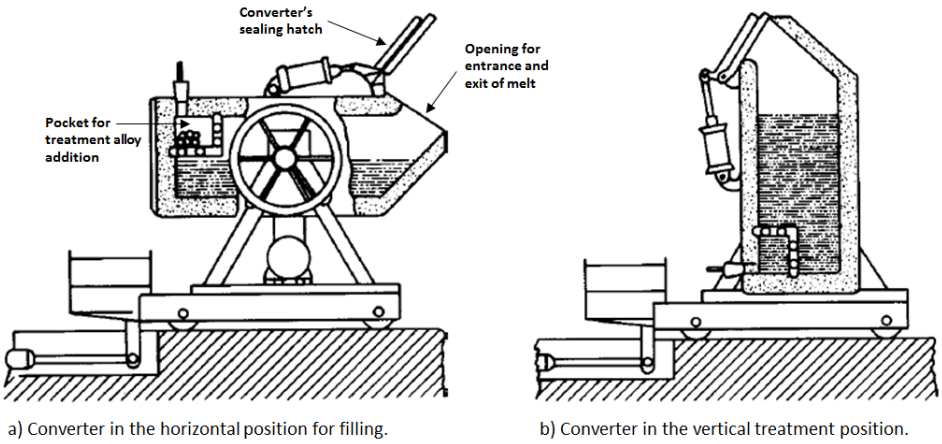

Figure 8 - Illustration of the working principal of a Georg Fischer converter [3].

For low sulphur melts, where no previous desulfurization process is needed, traditional treatment methods such as Sandwich, Tundish-cover or wire-treatment are employed. On both Sandwich (see **Figure 9a** and **Figure 9b**) and Tundish-cover (see **Figure 9c**) methods, the treatment FeSiMg alloy is placed in a pocket on the bottom of the ladle before the melt is tapped into it. The difference between these two methods is the fact that on the Sandwich method no cover is used on the ladle.

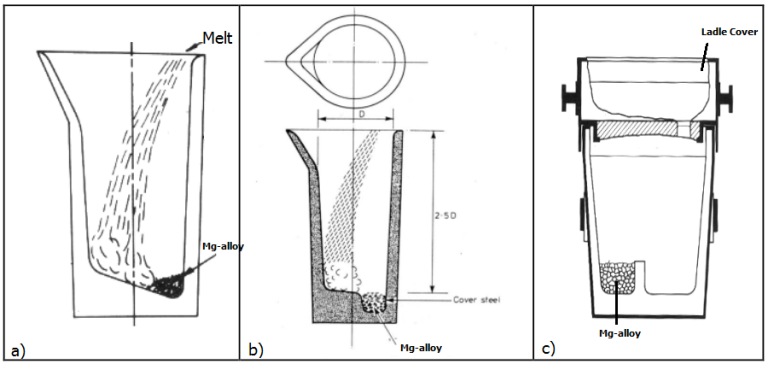

Figure 9 - Ladle design for traditional methods of Sandwich (b) and Tundish-Cover (c) melt treatment [20].

Although Sandwich and Tundish-cover treatment methods are more usual, wire-treatment is gaining popularity. It consists in the addition of the nodularization alloys in the form of a cored-wired to the melt inside the treatment ladle, using a wire-feeder machine, as illustrated in **Figure 10**. Once the addition of the treatment-wire is performed using a machine, this treatment process

can be more automatized and requires less operator intervention. One of the advantages of wire-treatment is the more accurate calculation of the amount of treatment alloy added to the melt, due to fact that in wire-treatment method the melt is tapped into the ladle before the alloy additions, and so the exact melt weight and melt temperature can be considered in the treatment alloys calculation. In Sandwich and Tundish-cover methods the alloys are placed in the ladle before tapping and if the melt weight and temperature change according do not comply with the target, no compensation of the alloy additions is made.

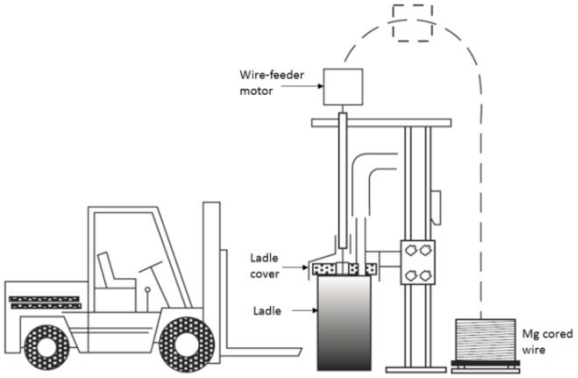

Figure 10 - Illustration of a wire-feeder machine for addition of Mg cored-wire [19].

In terms of treatment efficiency, measures by the ratio between the amount of Mg added and the final content of Mg in the melt (also called Mg-recovery), the Sandwich and Tundish-cover treatment methods can have an Mg-recovery of approximately 60 % to 80%, while the wire-treatment method can have around 40% to 60% [20] [21].

An additional treatment process exists, named "In-mould", that consists in the addition of the Mg-alloys inside of a reaction chamber moulded in the running system of the mould's in-gate (see **Figure 11**) [19].

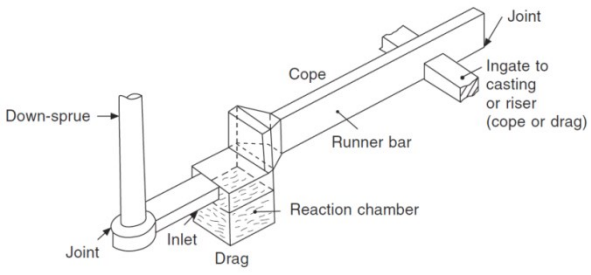

Figure 11 - Illustration of the "In-mould" system for nodularization treatment [19].

3.2.3. Inoculation treatment

The practice of inoculation[7] in nodular cast iron production can be performed at several different stages of the production process, and with more than one step of addition. The main methods of inoculant addition are:

- Ladle inoculation: addition of inoculant in the treatment ladle, normally simultaneously or after the Mg-alloys addition (lumps or wire);
- Late stream inoculation: addition of inoculant during pouring of the melt into the mould, directly in the metal pouring stream (see **Figure 12**);
- Mould inoculation: Addition of inoculant in a pocket built in the running system of the mould.

The type of inoculant (depending of the chemical composition) and the moment of inoculant addition (single addition or multiple additions) depend on the type of process used, type of castings produced and also in the foundries own experience.

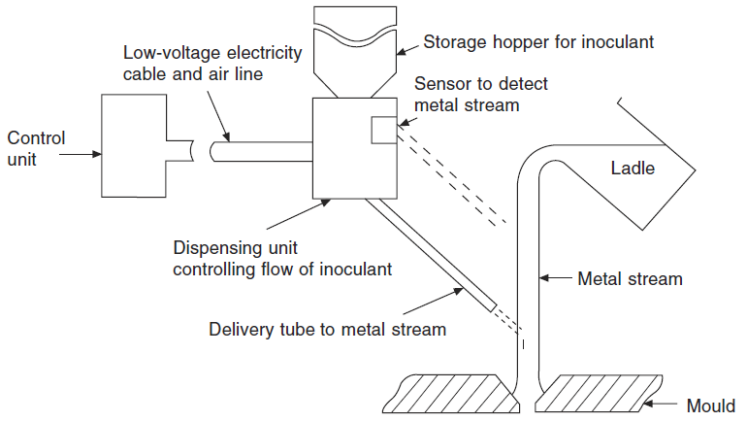

Figure 12 - Illustration of a late stream inoculant addition system [19].

The chemical composition of the different inoculants available in the market will influence its adequacy for the different moments of addition. Different inoculants have different reaction times, dissolution times and fading times, depending on the nature of the active elements that they have.

[7] Inoculation – Process step in cast iron production for adding FeSi based alloy containing also Al, Ca and some other active elements such as Ba or Bi among other, to promote the heterogeneous nucleation of graphite particles from the melt.

Figure 13 shows some of these properties for some of the active elements often used in inoculants, in terms of fading (**Figure 13a** measured by the number of nodules per mm^2 over time), and on a general overview on inoculation effect, fading and side effects (**Figure 13b**). For example, inoculants containing Ba have a good fading resistance although their inoculation effect is not as strong as Sr. Nevertheless inoculants containing Sr have a much faster fading than Ba. This indicates that Ba-containing inoculants are good for ladle inoculation and Sr for late inoculation.

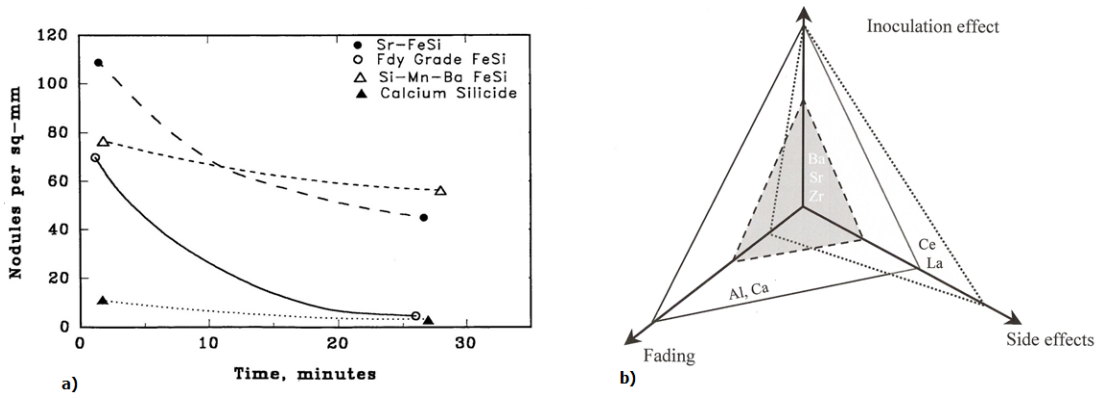

Figure 13 - Effect of active elements on the inoculant's performance; a) comparison of fading time; b) illustration of general performance changes in inoculants due to the active elements used [22].

3.2.4. Process control

Typically, process control during production of nodular graphite cast iron uses the following techniques:

- Base iron melt preparation:
  - Chemical analysis (spectrometer and C/S combustion analyser for C[%] and S[%]),
  - Thermal Analysis (for determination of C.E.[%], C[%] and Si[%]),
  - Temperature measurement
- After treatment/pouring:
  - Chemical analysis (spectrometer),
  - Fast metallographic sample (pouring of a sample from the melt into a small sand form for later observation of the microstructure),

- Wedge sample (evaluation of the white solidification area from wedge sample to evaluate inoculation)
- Temperature measurement

The most advanced and modern production processes, use thermal analysis test after treatment or at pouring in order to improve the melt quality assessment. This technique replaces more traditional testing methods such as the fast metallographic sample and the wedge sample. Such technique is used in the attempt to estimate:

- Metallographic characteristics, such as nodularity, nodule count, tendency to form carbides (Fe_3C), pearlite and ferrite content;
- Mechanical properties, such as tensile strength;

The use of the thermal analysis sampling points is strategically placed in key points of the process to allow an active and effective correction of the melt before pouring. They can be placed close to the treatment machine for evaluation of the treatment efficiency or at the pouring line to estimate the final casting characteristics.

3.2.5. New developments

In recent year some new developments have been made with the aim of improving and modernizing the nodular cast iron production.

At the 2011 GIFA exhibition in Düsseldorf, the company Foseco presented their own converter for treatment of nodular cats iron melt, named INITEK® (see **Figure 14**), using their own treatment alloys NODULANT®, a FeSi based Mg-alloy and INODEX®, a FeSi based initializer. They claim that their process usage allows an economy on the use of Mg alloy by consuming only 0,065% to 1% max. from the total melt weight and magnesium recovery rates of up to 97% [23].

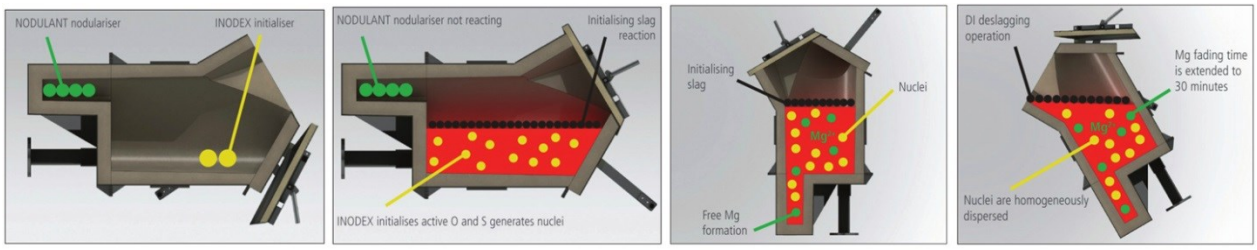

a) The converter is loaded with the necessary metal treatment alloys.

b) The melt in poured inside the converter and the initializing reaction with the INODEX takes place.

c) The converter is rotated to the vertical position to start the nodularizing treatment.

d) After nodularizing and deslagging operation, the nodular graphite cast iron is ready to be poured into the molds or pouring vessel.

Figure 14 - Illustration of the working principal of the INITEK converter from FOSECO [23].

Following a new concept of "ladle metallurgy" the company OCC GmbH developed in 2012 a treatment machine named TreatMaster that combines a wire-treatment machine with a bulk-dosing machine for melt alloying and treatment to produce nodular graphite cast iron (see **Figure 15**). The concept is based on the preparation of a single base iron melt for nodular graphite casts iron, with low copper, tin and silicon, usually for the production of low grade nodular iron. The melt is tapped into a ladle and taken to the treatments machine. The operator indicated the grade of nodular iron that is intended, and the machine automatically weights and adds the alloying elements to the ladle.

Alloying elements can be FeSi, Cu, Sn, C among other upon requirement from the customer. After the alloying addition, the Mg-alloy cored wire and the inoculant cored wire are added to perform the nodularizing and inoculation treatment. Such process allows the foundry to reduce the variety of base iron melt recipes and increases the process flexibility by allowing the foundry to produce different nodular iron grades from the same base iron melt [24] [25].

Figure 15 - Photograph from OCC's TreatMaster for ladle metallurgy [25].

On the process control area, apart from the use of thermal analysis, several companies start to offer dedicated process control software. The aim of such softwares is to gather information throughout the foundry process and use it to give information to the operator on corrective actions needed. An example of such software is the Navigator software from the company OCC GmbH. The Navigator software (see **Figure 16**) gather information related to spectrometer analysis (chemical composition of the melt), tapping and treatment temperatures, thermal analysis results and alloy specifications to calculate automatically the required alloying and treatment addition to the melt in order to obtain the desired melt quality results. The software directly controls the wire treatment machine and bulk dosing machine for ladle additions [26] [27]. The melt quality evaluation is also performed by the software using a built-in metallurgical quality evaluation model that used the thermal analysis information from a sample taken from the treated melt into a closed thermal analysis cup named AccuVo®, which the company OCC GmbH claims to be more accurate in the obtainment of results than a regular open cup [28].

Other companies such as SinterCast with the System 3000 [29], Foseco with the ITACA® software [30] and NovaCast with the ATAS MetStart™ [31] offer similar software solution for process control.

Figure 16 – Print-screen from the main window of the software Navigator, used for process control of the nodular graphite cast iron production [26].

3.3. Review on solidification mechanisms of ductile cast iron

Solidification is an extremely important step in material processing, especially in cast iron alloys used as-casted. In this type of castings, the microstructure that results from the solidification process is the one that will give the material's final mechanical properties, once no further manipulation (heat treatment for example) will be applied to further change the material's microstructure. Nevertheless, the influence of solidification in the microstructure does not affect only the mechanical properties, but can also be the origin of defects formation such as shrinkage or porosity [32].

Once solidification is the step that defines the microstructure of cast iron (as-casted), it is important to know and understand the different microstructures that can result from the solidification of a nodular cast iron. One of the most important tools for the study and understanding of the microstructure development are the equilibrium phase diagrams. Phase diagram define the different phases that coexist in a equilibrium system, as well as the composition of those phases over a range of temperature (assuming that the effect of pressure in the system's thermodynamic is always constant). Once chemical equilibrium is involved during solidification, phase diagrams have a thermodynamic basis on its construction. Unfortunately, due to their thermodynamic basis, phase diagrams indicate what should happen during solidification and not what really will happen, once the behaviour of the real system is affected by kinetic processes such as solute, heat transfer and nucleation [3] [33].

3.3.1. The Fe-C equilibrium phase diagram

Cast iron materials, either grey (for all types of graphite shape) or white cast irons follow the solidification steps indicated in the Fe-C equilibrium phase diagram (see **Figure 17**). Once cast irons are characterized by being alloys that solidify with a eutectic transformation of liquid in austenite + graphite (or Fe_3C), it means that the melt has more than 2,11% of carbon, once that is the upper content of carbon that can be dissolved in the austenite.

The eutectic point in the diagram is achieved for a carbon content of approximately 4,3%. This is the point where the liquid solidifies forming two solid phases. This eutectic transformation point can occur at two different temperatures, depending on the nature of the phase rich in carbon.

The eutectic transformation temperature of 1152°C, corresponds to the stable eutectic transformation, where carbon solidifies as graphite (discontinuous line at the eutectic transformation stage in **Figure 17**). The eutectic transformation temperature of 1145°C, corresponds to the metastable eutectic transformation (continuous line at the eutectic transformation stage in **Figure 17**) where carbon solidifies as iron carbides (Fe_3C). For compositions of carbon higher than the one of the eutectic composition, there are also two solidus lines. The discontinuous solidus line corresponds again to the solidification of graphite and the continuous solidus line to the solidification of iron carbides (Fe_3C).

All melts with a carbon content lower than 4,3% are named hypoeutectic and all melts with a carbon content higher than 4,3% are named hypereutectic. Melts with 4,3% of carbon are simply named eutectic.

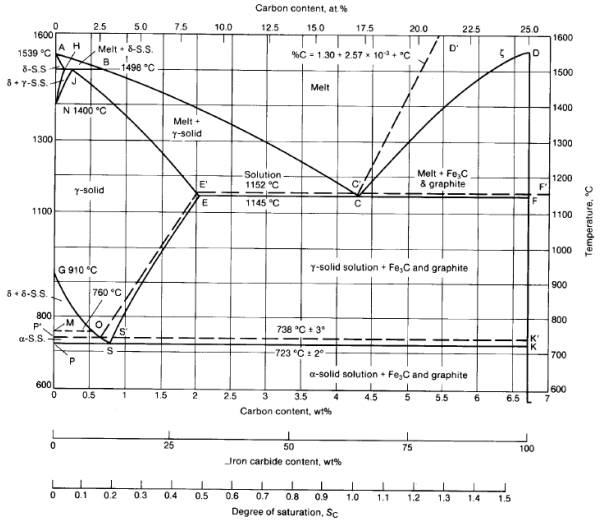

Figure 17 - The Fe-C equilibrium phase diagram.

3.3.1.1. Hypoeutectic solidification sequence

As described above, hypoeutectic melt compositions have carbon contents lower than the eutectic point, as in the example from **Figure 18**. As the melt temperature decreases, it will start to solidify once the liquidus temperature (T.Liq.) for that melt composition is reached. In the case of hypoeutectic alloys, that is represented by the liquidus line for the austenite. When the melt temperature drops below the liquidus line the solidification of primary austenite phase start. This primary austenite grows usually from the liquid with a characteristic dendritic shape.

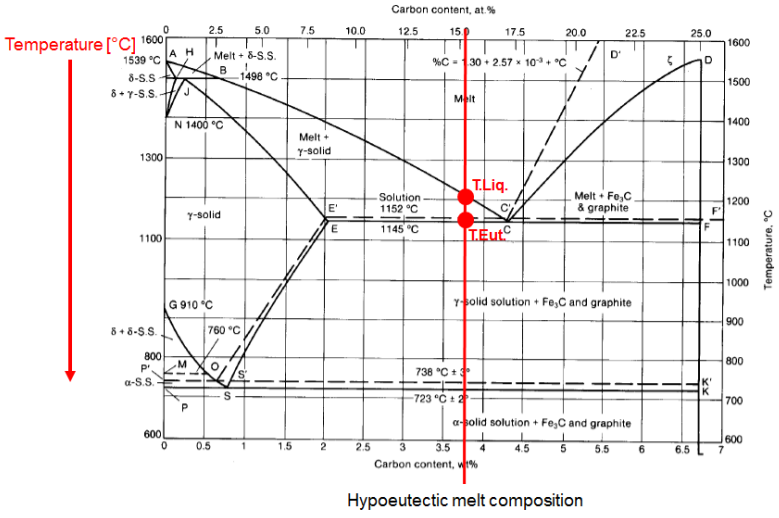

Figure 18 - Fe-C diagram showing the solidification path of a hypoeutectic melt composition.

As the temperature continues to decrease, bellow the liquidus line, austenite continues to nucleate and grow. The remaining melt composition changes as carbon content increases. This increase of carbon content in the melt is due to the segregation of carbon from the newly formed austenite crystals into the melt. Therefore, the carbon content in the melt will follow the austenite liquidus line until the eutectic transformation point is reached (see **Figure 19**) [34]. The carbon content on the austenite can be determined at each temperature during cooling, by reading the carbon content in the X-axis for the interception point between a given temperature line with the Solidus line for the austenite field. In the same way, the carbon content in the remaining liquid melt can be determined at each temperature during cooling, but this time by the intersection of the temperature line with the austenite liquidus line.

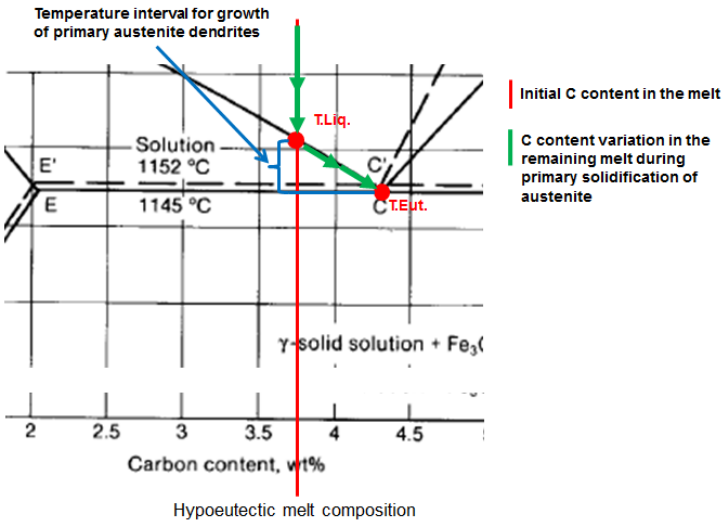

Figure 19 - Detailed section of the Fe-C diagram close to the eutectic point to shows how the carbon content in the melt changes during primary solidification and growth of austenite in hypoeutectic melt compositions.

Once the eutectic transformation temperature is reached, the reaming melt will then solidify completely, according to the stable (Liquid = $\gamma Fe + C_{graphite}$) or metastable (Liquid = $\gamma Fe + Fe_3C$) eutectic transformation depending on the kinetic properties of the melt.

Detailed description of the primary austenite solidification is given in chapter 3.3.2.

3.3.1.2. Hypereutectic solidification sequence

In opposition to hypoeutectic melts, hypereutectic melt compositions have carbon contents higher than the eutectic point, as presented in **Figure 20**.

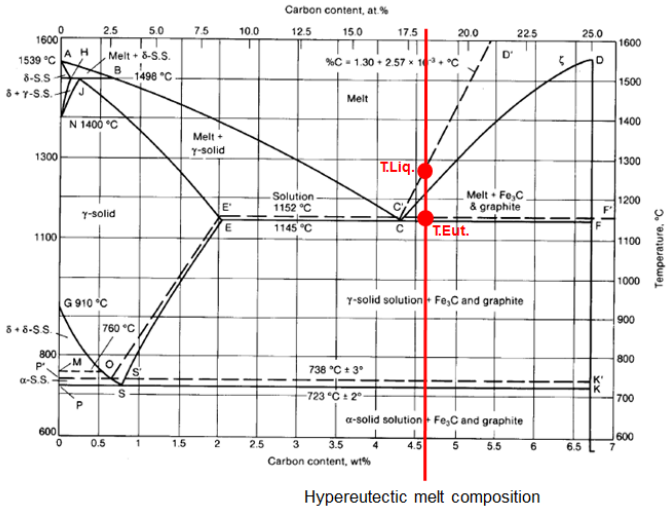

Figure 20 - Fe-C diagram showing the solidification path of a hypereutectic melt composition.

From the phase diagram in **Figure 20**, it can be observed that there are two liquidus lines for hypereutectic composition. The discontinuous line represents the stable solidification of carbon as graphite and the continuous line the metastable solidification of carbon as Fe_3C. Depending on the kinetic properties of the melt, its preparation (inoculation) and the cooling rate, affecting a given portion of melt, the solidification will follow only one of those two liquidus lines, and not both simultaneously.

Considering the case of a melt that will solidify according to the stable solidification of carbon into graphite, as the liquid melt temperature decreases, solidification starts once the temperatures drops below the liquidus line. At this point graphite will nucleate and grow freely in the liquid, as the primary solidifying phase. During this primary graphite solidification period, between graphite liquidus line and the eutectic transformation line, the carbon content on the remaining liquid will decrease due to the diffusion of carbon from the melt into the growing graphite particles. The carbon content in the melt will then follow the graphite liquidus line until the eutectic composition is reached (see **Figure 21**).

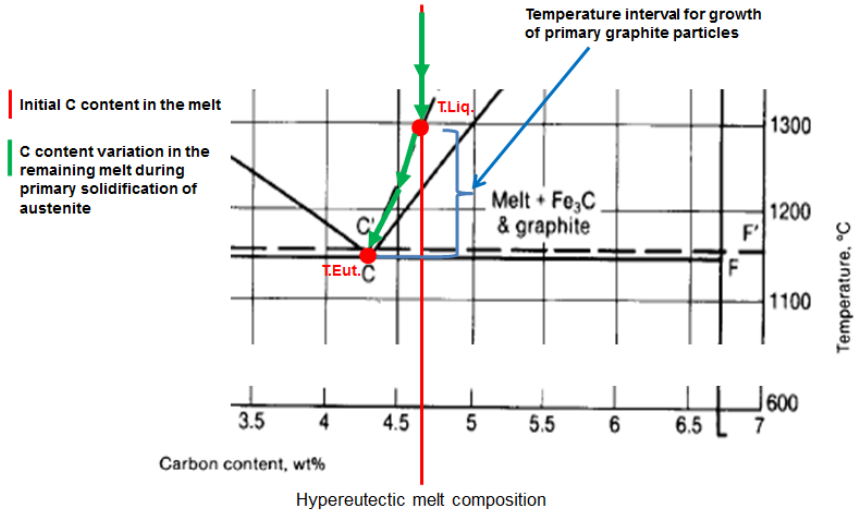

Figure 21 - Detailed section of the Fe-C diagram close to the eutectic point to shows how the carbon content in the melt changes during primary solidification and growth of graphite in hypereutectic melt compositions.

Once again, when the remaining melt reaches the eutectic composition, the eutectic transformation will occur according to the stable (Liquid = $\gamma Fe + C_{graphite}$) or metastable (Liquid = $\gamma Fe + Fe_3C$) eutectic transformation depending on the kinetic properties of the melt.

Detailed description of the primary graphite solidification in nodular cast iron will be given in chapter 3.3.3.

3.3.1.3. Eutectic solidification sequence

The iron melts denominated by eutectic melts, are the ones that have exactly the same carbon content as the eutectic point (see **Figure 22**).

This means that the melt will cool down until its lowest possible liquidus temperature, and at that point the entire melt will solidify according to the eutectic transformation. Once again this transformation will occur according to the stable (Liquid = $\gamma Fe + C_{graphite}$) or metastable (Liquid = $\gamma Fe + Fe_3C$) eutectic transformation depending on the kinetic properties of the melt.

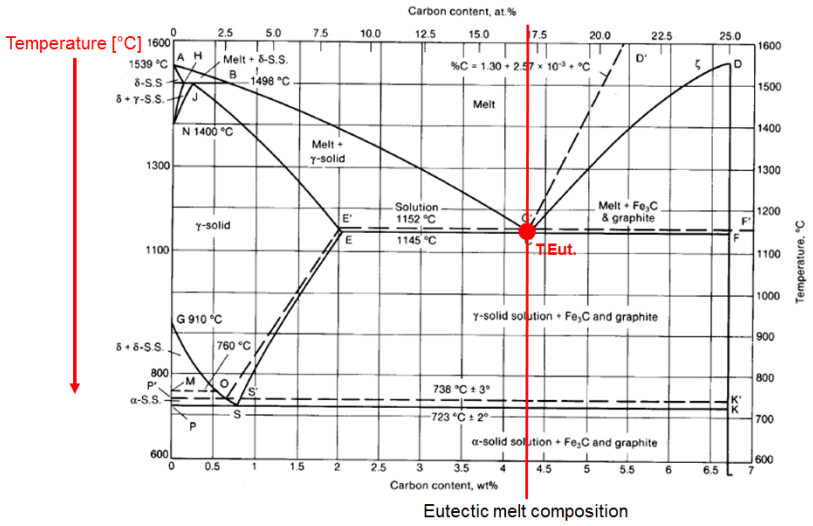

Figure 22 - Fe-C diagram showing the solidification path of a eutectic melt composition.

Once in the eutectic transformation, no primary leading phase exists, no significant segregation to the liquidus will occur.

Detailed description of the eutectic solidification of nodular cast iron will be given in chapter 3.3.4.

3.3.1.4. Influence of Si and other elements on the Fe-C diagram

Cast irons are complex alloys that have a significant content of Si. Silicon is a graphitization element, increasing the carbon activity in the molten metal, promoting the stable solidification of carbon into graphite, instead of the metastable with formation of Fe_3C [3].

The presence of Si on cast iron, causes changes in the Fe-C equilibrium diagram, and makes it necessary to consider a ternary phase diagram of Fe-C-Si. One of the main changes caused by Si is the reduction of the carbon content in the eutectic point. **Figure 23** shows that as Si content increases, the carbon content in the eutectic decreases (moves to the left). That movement causes also a reduction of the austenite field area (γ) on the diagram. This means that as the Si content in the melt increases, the solubility of carbon in the austenite decreases.

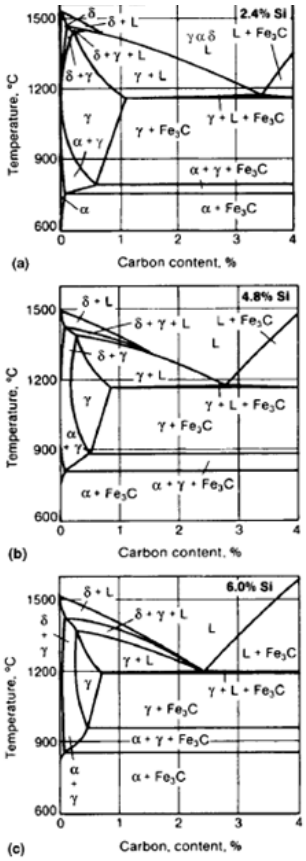

Figure 23 - Influence of Si content in the Fe-C equilibrium diagram temperatures, for silicon contents of 2,4%(a), 4,8%(b) and 6,0%(c) [3].

The change in the carbon content in the eutectic point can be calculated as a function of the Si content in the melt according to **Equation 1**.

$$C_{eutectic}[\%] = 4{,}30 - \frac{1}{3}Si[\%] \quad \text{(Eq. 1)}$$

Due to the influence of Si on the eutectic point and carbon content of the Fe-C equilibrium phase diagram, a variable named Carbon Equivalent (C.E.) was defined. This C.E. represents an fictional carbon content in the Fe-C equilibrium phase diagram considering that the present of Si in the melt acts as more carbon. Using this C.E. value instead of the real carbon content of the melt, it is possible to use the binary Fe-C phase diagram (in the X-axis the C.E. value should be considered instead of the original C content) to determine if the melt is hypoeutectic, eutectic or hypereutectic. The eutectic point is considered to have a C.E. value of 4,3%. The calculation of the C.E. values is presented in **Equation 2 [35]**.

$$C.E.[\%] = C[\%] + \frac{1}{3}Si[\%] \quad \textbf{(Eq. 2)}$$

Often the C.E. equation is re-written to include also the influence of phosphor in a similar way to the influence of silicon. The C.E. will then be calculated according to the **Equation 3**.

$$C.E.[\%] = C[\%] + \frac{Si[\%]+P[\%]}{3} \quad \textbf{(Eq. 3)}$$

Another change in the Fe-C equilibrium phase diagram caused by Si is the change of the stable and metastable eutectic temperatures. As the silicon content in the melt increases, the stable eutectic temperature (Liquid = γFe + $C_{graphite}$) increases and the metastable eutectic temperature (Liquid = γFe + Fe_3C) decreases (see **Figure 24**). The final results will be a bigger temperature interval between these two temperatures.

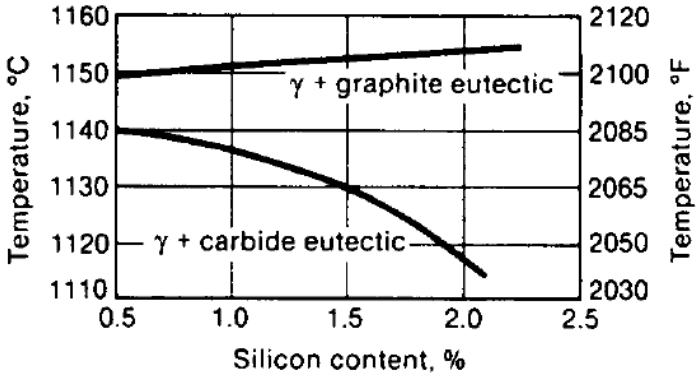

Figure 24 - Influence of Si in the stable and metastable eutectic temperatures of the Fe-C equilibrium phase diagram [3].

Apart from the significant influence of Si on the solidification of cast iron melts, other elements also present in the melt can influence the Fe-C diagram. All this others elements can equally be classified as graphitizing elements such as nickel, copper and cobalt (will like Si decrease the metastable eutectic temperature and increase the stable eutectic temperature) and other elements such as Cr and V will have the contrary effect in the eutectic temperatures, acting as non-graphitizing elements [3]. **Figure 25** shows the effect of several alloying elements in the stable (represented as T_{EG}) and metastable (represented as T_{EM}) eutectic temperature of the Fe-C equilibrium phase diagram [36].

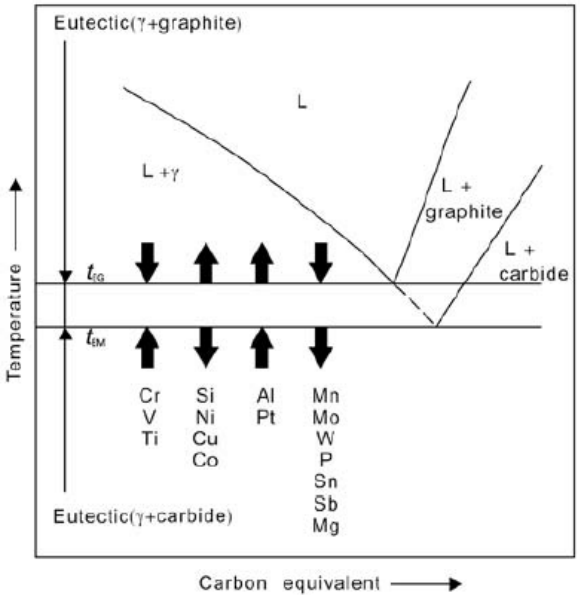

Figure 25 - Effect of alloying elements on eutectic stable and metastable temperature of the Fe-C diagram [36].

3.3.1.5. Non-equilibrium Fe-C phase diagram

Although a valuable tool, the Fe-C equilibrium phase diagram has no direct transposition to foundry practice, once it is based in thermodynamic calculation and long solidification periods, not accounting the influence of several process parameters that affect the solidification process in foundry practice. These parameters are the cooling rate, nucleation state of the iron melt, pre-processing of the melt (superheating and holding time), and presence of impurities. These variables will significantly influence casting solidification structure, not only influence the temperature and composition boundaries in the diagram but also the development of the solidification structure. Due to the influence of these variables and the associated difficulties in controlling them, the prediction and description of the structure developing during non-equilibrium is much more complicated than the one of equilibrium conditions [36].

In order to overcome this limitation on the application of equilibrium phase diagrams to the foundry practice, the solidification phase diagram were created, to describe only the relationship in the liquid-solid transition region considering some non-equilibrium conditions. These solidification diagrams were created based on thermal analysis curves measured under more realistic circumstances to the ones existing in the foundry practice [37].

These solidification diagram, although sometimes difficult to read, have the objective to give more accurate information on the solidification structure of cast iron than the equilibrium phase diagram. **Figure 26** presents the solidification diagrams for the metastable and stable solidification of cast iron as a function of the Si content of the melt. From the stable solidification diagrams it is visible how the eutectic point moves to the left and the eutectic temperature raises as the Si content increases. For the metastable it is possible to observe how the metastable eutectic temperature decreases with the increase of Si content in the melt.

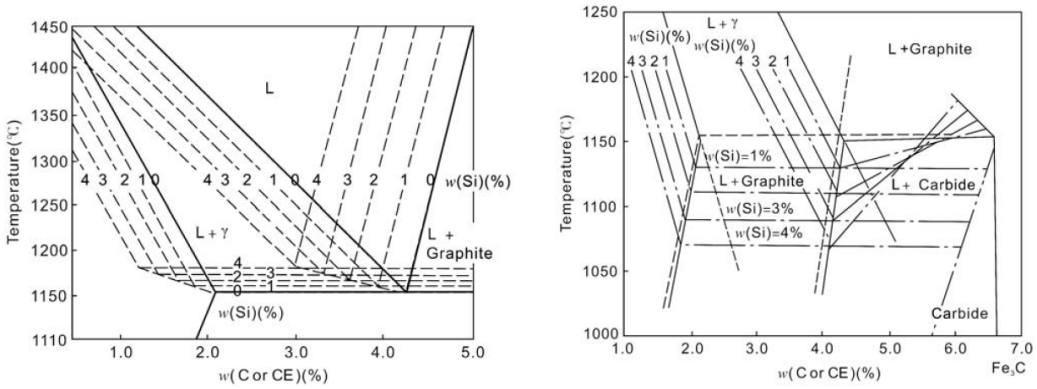

Figure 26 - Fe-C solidification phase diagram showing the stable (left) and metastable (right) solidification [37].

Due to the non-equilibrium solidification of a melt and caused specially due to undercooling effects, also the eutectic point if affected. In case of undercooling at the eutectic temperature, the liquidus line for the austenite liquidus and the graphite liquidus are extended bellow the theoretical eutectic temperature, as presented in **Figure 27**. This means that the graphite liquidus temperature will be extended to the left of the eutectic point (E) and the austenite liquidus will be extended to the right of the eutectic point. Between these newly extended liquidus lines, a new region is defined as a non-equilibrium eutectic region also denominated as quasi-eutectic region, where both graphite and austenite can solidify (eutectic structure is formed), like in the example for a melt with composition ***C*** that undercools until the temperature ***t*** in **Figure 27** [36].

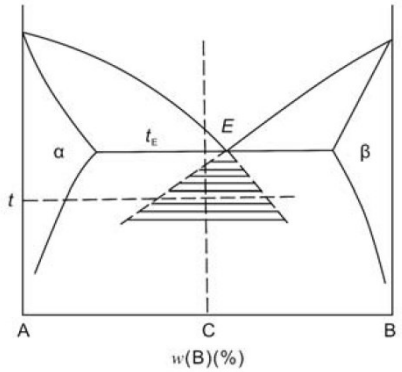

Figure 27 - Illustration of the centralized non-equilibrium eutectic region [36].

This eutectic region can be symmetrical, normally for metal-metal eutectic alloys (see **Figure 28a**), or non-symmetrical for non-metal/metal eutectic like the case of cast iron (see **Figure 28b**). In non-symmetrical eutectic regions the eutectic point is not contained in the eutectic region, once this region presents a deviation to the side of the eutectic phase that has the highest melting point (in case of Fe-C the deviation is to the right in the direction of the carbon side) [36].

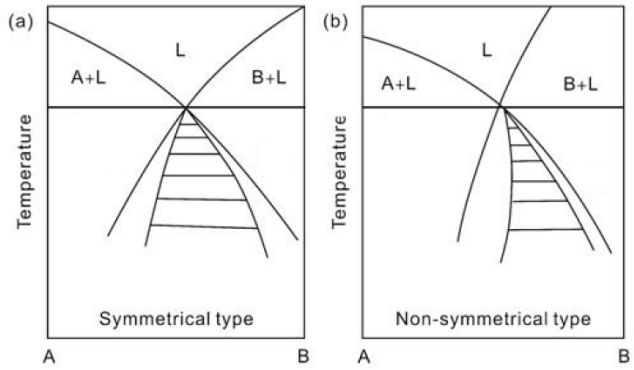

Figure 28 - Classification of the eutectic region according to his symmetry to the eutectic point [36].

3.3.2. Nucleation and growth of primary austenite

As in any material, the knowledge of the solidification process is important to optimize mould filling, casting soundness and the desired microstructure.

Primary austenite, also referred to as pro-eutectic austenite, is characterized as being the first crystals to nucleate and grow from the liquid in melts with hypoeutectic compositions [3] [32].

The study of the austenite dendritic structure has received considerably less attention from investigators, when compared to the studies conducted on graphite and eutectic nucleation and morphology. This might happen because the austenite structure is not readily observed from as-polished as-casted cast iron sample due to the solid state transformation of austenite as it cools bellow the eutectoid temperature [3] [38]. In order to overcome this problem and allow a detailed view of the austenite structure, investigators have to use special laboratory techniques such as colour etching [15] [39], DAAS[8] and ESBD[9] [38], directional solidification and quenching [32] [40].

Primary austenite nucleates heterogeneously from the liquid melt, using different kinds of nucleus. This nucleus can be often oxides present in the melt such as SiO_2 or other agent particles added to the melt in the form of preconditioning such as SiC or inoculant particles (FeSi and CaSi) [41]. These conclusions were taken for grey iron samples, as no study was found that studies the same effect in nodular cast irons, but similarities in the nucleation principal of dendrites can exist.

The growth of primary austenite in cast irons follows a typical non-planar (sometimes also called instable) solidification interface or front. The most usual non-planar interfaces are cellular and dendritic microstructures (columnar or equiaxed), presented **Figure 29**, that often lead to micro-segregation and formation of secondary phases.

[8] DAAS – Direct Austempering After Solidification
[9] ESBD – Electron Back Scatterring Diffraction

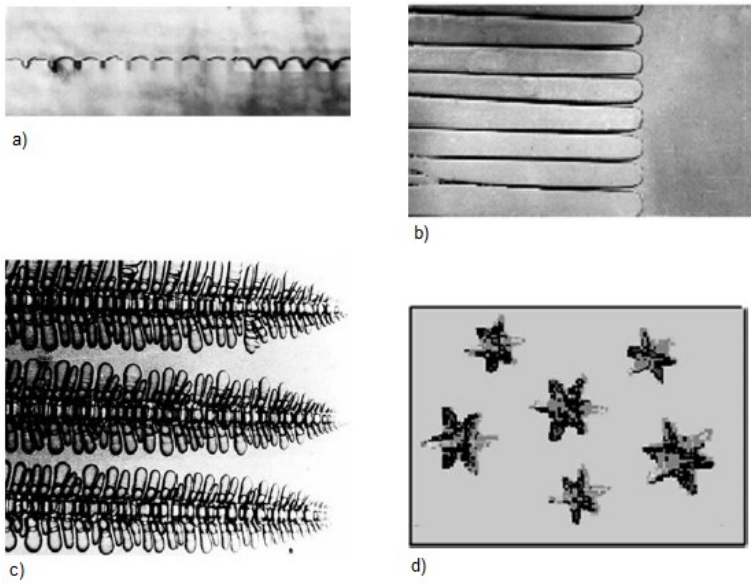

Figure 29 - Solidification structures resulting from non-planar solidification interfaces. a) Surface cellular; b) Deep cellular; c) Dendritic; d) Equiaxed dendrites [3].

3.3.2.1. Main causes for non-planar solidification front

The main causes for the instability of a solidification front and determination of the type of structure that solidifies (cellular or dendritic) are thermal instability and the solutal instability that rises in the solid/liquid (S/L) interface. To describe the principles of the non-planar solidification interface, it is necessary to consider that at the solidification interface, a perturbation is formed and if this perturbation is damped on time, the solidification front is planar, but if the perturbation is amplified in time the interface will be non-planar.

The thermal instability in the solidification interface happens due to temperature gradients (G_T) that can be positive or negative.

Positive temperature gradients are installed when the melt temperature at the S/L interface is lower than the melt temperature at the bulk liquid melt. Normally, the solidification starts in the interface between the mould wall and the liquid melt. In these cases, the latent heat release is dissipated by the solid, through the mould wall, causing the temperature of the melt at the S/L interface to be lower than the temperature on the bulk liquid melt, resulting in a positive temperature gradient.

Under positive thermal gradients columnar growth will prevail, and the morphology of this columnar front can be planar (stable), shallow cellular, deep cellular or dendritic (instable). The S/L interface will be planar if V>Va (where V is the interface growth velocity and Va the velocity of absolute stability) or when V<Vc (where Vc is the velocity of constitutional undercooling). In these assumptions the thermal gradient and the composition are taken to be constant.

In cases where Vc<V<Va, the planar interface will became instable and a shallow cellular, deep cellular or dendritic structure will be formed, similar to the structures represented in **Figure 29** [3]. It is therefore understandable that morphology of the columnar growth is intimate related to the cooling temperature and velocity of interface solidification.

In opposition to this case, a negative temperature gradient means that the temperature of the melt at the S/L interface is higher than the temperature in the bulk liquid. This inversion on the temperature gradient occurs if the melt is subjected to a high undercooling in its bulk liquid area (away from the mould/liquid interface).

In these conditions, nucleation can start in the bulk liquid area of the melt with the formation of small particles that, due to the isotropic condition in the liquid, will have a spherical shape. Due to the latent heat of fusion evolution at the S/L interface of this spherical particle, the liquid temperature at the interface will raise. This will cause a local negative temperature gradient because the liquid at the interface will be at a higher temperature than the liquid away of the surface.

If a perturbation forms at the S/L interface it will contact with a liquid that has a lower temperature than its melting temperature causing an undercooled environment that will potentiate the further growth of the perturbation. Once this perturbation can occur at any direction from the initial solidified sphere, equiaxed dendrites will grow. Therefore, negative temperature gradients will promote the growth of equiaxed dendritic structures [32].

Nevertheless, the temperatures gradients are not the only influence on the non-planar solidification fronts and will be influence also by the solutal instability at the S/L interface related to constitutional undercooling.

Constitutional undercooling, results from solute distribution differences between the solid and the liquid phase at the S/L interface and the solute diffusion in the liquid phase. Observing the **Figure 30** , that represents graphically this effect, considering an alloy with a final composition C_0 that has a liquidus temperature T_L and Solidus T_S. The concentration of solute in the liquid ahead of the solidification front (liquid close to be solidified) has a composition C_0/k, where k is the equilibrium partition coefficient that expresses the ratio between the solid and the liquid composition at the interface ($K=C_{Solid}/C_{Liquid}$). At the upper left equilibrium diagram represented in **Figure 30**, the above variables are represented.

For a given temperature of the melt during solidification T*, the liquid melt is expected to have a composition given by C_L*, with a solute composition that is higher than the solute composition at the beginning of solidification (C_0), that results from solute that is being rejected by the solid phase to the liquid. The variation of the solute composition at the S/L interface and the melt bulk at a given temperature T*, is represented in the lower left graphic from **Figure 30**. The composition of the solute increases at the S/L interface from C_0 in the solid to C_0/k in the liquid, according to the equilibrium diagram. Nevertheless, from the S/L interface into the melt bulk, there is a decrease of the solute concentration related to the solute diffusion in the liquid phase.

The melt thickness, from the S/L surface to the bulk melt where the solute concentration is above the C_L* for a melt temperature T* is defined as diffusion boundary layer (dc). During this diffusion layer the solute concentration changes from C_0/k to C_L, and according to the equilibrium diagram this composition have a liquidus temperature associated. This means that the liquidus temperature in the melt will change from the S/L interface into the bull melt region. This phenomenon is represented in the upper right graphic from **Figure 30**, where it is seen that the liquidus temperature of the melt increases from the S/L interface to the bulk melt region. Therefore, at the S/L interface it is possible to define a liquidus temperature gradient G_L [32].

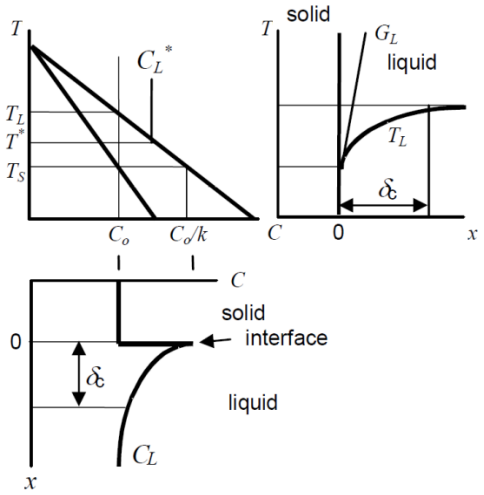

Figure 30 - Representation of the solute concentration and liquidus temperature at the front of the S/L interface [32].

Once the melt is also subjected to a thermal gradient (G_T) that defines the melt temperature at a given position from the S/L interface to the bulk melt, it is than possible to represent together both the thermal gradient and the Liquid temperature gradient in the S/L interface, as in **Figure 31**. If $G_T > G_L$, it means that ahead of the S/L interface the melt temperature is higher that it's liquidus temperature. On the contrary, if $G_T < G_L$, it means that over a certain distance ahead of the S/L interface the melt temperature is bellow it's liquidus temperature, because of the solute concentration in the diffusion layer and in this region the melt is considered to be constitutionally undercooled (UC – Constitutional Undercooling) [32].

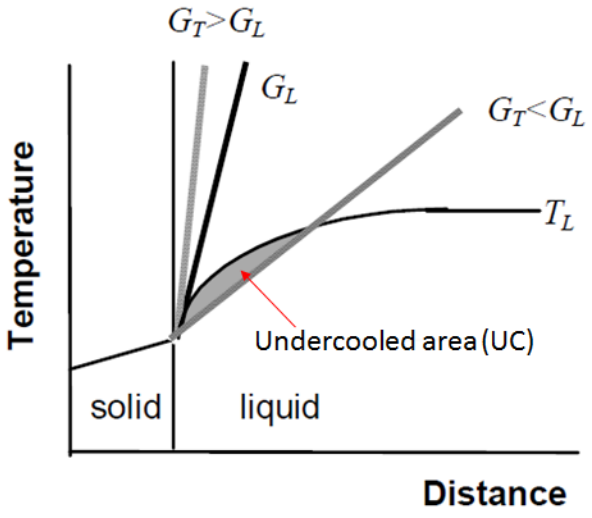

Figure 31 - Representation of the constitutional undercooling [32].

If the melt ahead of the S/L interface is under constitutional undercooling, this means that any instability growing from a planar interface will enter in contact with a liquid that has a temperature bellow its liquidus temperature, giving conditions for this instability to grow even further and faster. The interface will enter in non-planar (irregular) growth mechanism. Nevertheless the morphology of the non-planar S/L interface will depend on the magnitude of the constitutional undercooling installed. If the constitutional undercooling is small, the growth will be mainly in the solidification direction resulting in a cellular interface.

As the constitutional undercooling increases, the spacing between the cells will also increase and a constitutional undercooling can also occur between the columnar cells, causing also growth in a direction perpendicular to the main growth direction. This will allow the instabilities on the sides of the cells to grow and a dendritic structure will develop. **Figure 32** illustrates the effect of growing thermal gradients in the constitutional undercooling and influence in the morphology of the non-planar solidification structure. As the thermal gradient decreases the solidification morphology changes from planar to cellular ($G_{p/c}$), to dendritic ($G_{c/d}$) to equiaxed ($G_{d/e}$). If the thermal gradient is almost flat, (G_T=0), almost no columnar growth will be possible and the structure will be mainly equiaxed [32].

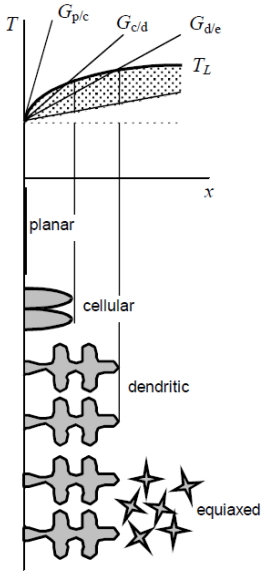

Figure 32 - Representation of the influence of increasingly higher constitutional undercooling in the morphology of the non-planar solidification interface [32].

On foundry practice, in a casting, it is possible that both columnar and equiaxed dendritic structures exist, forming a region called columnar-to-equiaxed transition (CET) area, illustrated in **Figure 33**. The columnar structure forms normally first at the mould walls, and grow towards the bulk liquid, following the opposite direction from the heat release flow. The CET area will form if enough large equiaxed grains nucleate and grow ahead of the columnar front. This equiaxed region will ultimately contact and obstruct the columnar growth [32].

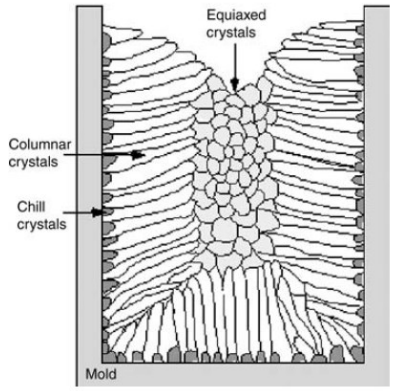

Figure 33 - Representation of the grain structure of columnar and equiaxed grains in a ingot casting [3].

The main parameters for the formation of this equiaxed austenite crystal zones is the nucleation and growth speed. A high nucleation potential for this equiaxed regions is reached either by the addition of enough heterogeneous nucleus or simply be effect of the imposed constitutional undercooling that develops on the front of the columnar growth region. If there is no constitutional undercooling ahead of the columnar front, no equiaxed grain nucleation is expected. On the contrary, if the constitutional undercooling on the front of the columnar region is high, there might be conditions for the nucleation of the equiaxed grains (see **Figure 34**). In this condition, if the required nucleation undercooling is smaller than the constitutional undercooling in the columnar solidification front, the nucleation and growth of the equiaxed crystals will occur [3] [32].

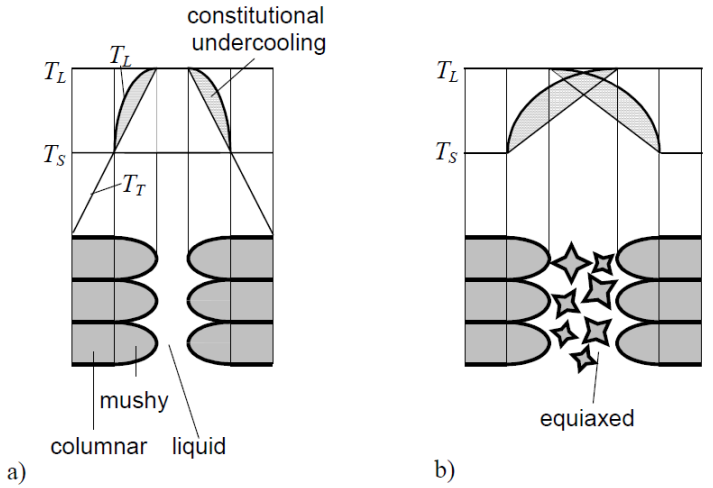

Figure 34 - Representation of the needed constitutional undercooling conditions for the formation of CET . a) no formation of CET due to low constitutional undercooling. b) formation of CET due to high constitutional undercooling in the columnar front [32].

3.3.2.2. Chemical Segregation during Austenite Growth

During solidification, a non-uniform distribution of solute elements leads to micro-segregation. Due to this micro-segregation effect it is natural that crystal that solidify earlier and crystal that solidify later, will present slightly different chemical compositions.

The segregation coefficient (K_s) represents this micro-segregation effect of elements in, for example, the austenite of nodular iron, through the following equation:

$$Ks = \frac{C_{Austenite}}{C_{LTF}} \quad \textbf{(Eq. 4)}$$

where, $C_{Austenite}$ is the element concentration in the centre of the austenite dendrite, and C_{LTF} is that same element concentration in the last freezing zone (LTF). The last freezing zones correspond to the intercellular region of the microstructure that is the last liquid fraction to solidify.

Segregation coefficients higher than 1 (Ks>1) correspond to elements that are segregated from the solid to the liquid, called positive segregation elements. Segregation coefficients lower than 1 (Ks<1) correspond to elements that are retained in the solid phase and not segregate to the liquid, called negative segregation elements.

Table 3, shows the segregation coefficient values for some of the main chemical elements in nodular cast iron [3].

Table 3 - Segregation coefficient for the austenite structure in nodular cast iron.

Element	Si	Mn	Mg	Cu	Cr	Ni	Mo
Ks for nodular iron (sand mold, ø30mm bar)	2,27	0,29-0,59	0,387	5,10	0,108	1,82	0,0053

3.3.2.3. Dendritic coherency

Dendritic coherency is a phenomenon in solidification of alloys with dendritic growth that correspond to the moment when the individual dendrites first impinge with their neighbours and is often referred to in the bibliography as "dendritic coherency point" or simply DCP [42] [43].

The importance of this solidification happening of dendritic coherency is that, it will influence greatly the ability of the liquid met to flow in the casting.

During solidification, there's the formation of so called "mushy zones" that correspond to areas of coexistence of liquid and solid phases. As long as the solid phase is free (in suspension) to flow with the liquid and the existing columnar structure is short, there will be a good flow of melt through the mould cavity. However, once dendritic coherency is reached, a rigid structure is formed, similar to an interconnected skeleton. After the occurrence of the dendritic coherency, the flow of melt is only possible through the inter-dendritic spacing of the solid structure, that will became smaller as the solidification proceeds and the dendrites continue to ramify and course. An illustration of this phenomenon is presented in **Figure 35**, where on the upper figure no dendritic coherency has occurred and the liquid can flow with no restriction, and on the bottom figure the coherency has occurred and the liquid flow is restricted [32] [42].

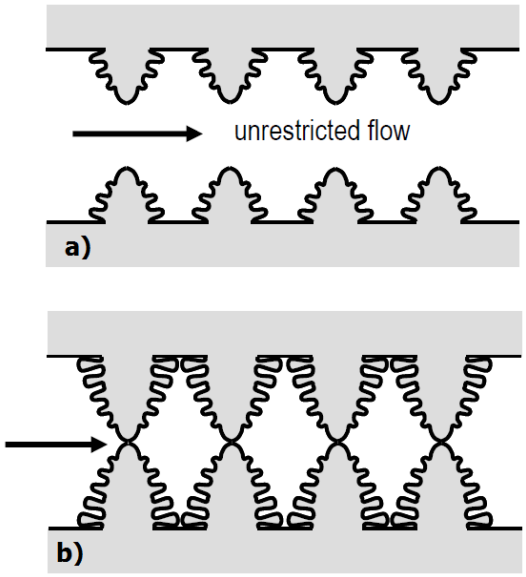

Figure 35 - Representation of the dendritic coherency phenomenon, on columnar solidification structure on a casting with parallel walls. a) before dendritic coherency, no restriction to liquid flow; b) after dendritic coherency, restriction on liquid flow [32].

3.3.3. Nucleation and growth of primary graphite

The nucleation and growth of primary graphite particles occur in hypereutectic cast iron melts, where graphite is the first solid phase to be formed from the liquid phase.

The nucleation of the graphite particles results from a heterogeneous nucleation process, because this requires substantially less energy to occur than homogeneous nucleation [3]. The heterogeneous nucleation of graphite will need a stable subtract (nuclei) from which graphite will start to solidify. Typical subtracts can be graphite particles and other carbon based particles present in the melt or complex oxide or sulphide particles. The most common description of the formation of complex oxide and sulphide nuclei for ductile iron, was initially proposed by M. Jacobs et.al in 1974 and later further developed by T. Skaland et.al. [44]. It assumes that a multi-layer sulphide-oxide inclusion of approximately 1µm diameter is the nuclei that serve as base for the growth of graphite in ductile iron. The nuclei is formed by sulphides (MgS or CaS) covered by Mg silicates (such as $MgO.SiO_2$). These particles will then be further "coated" by hexagonal silicates of other elements such as Al, Ca, Sr, Ba among others (also referred to as active inoculation elements) that form a coherent/semi-coherent low energy interface where the carbon can more easily attach to. The incorporation of the active elements in the melt is done through the

addition of inoculant alloys. Inoculant alloys are mainly FeSi alloys with small concentrations of the active elements. There are several different inoculants available with different active elements and contents. **Figure 36** shows the structure proposed by Skaland, of the multi-layer sulphide-oxide nuclei [44].

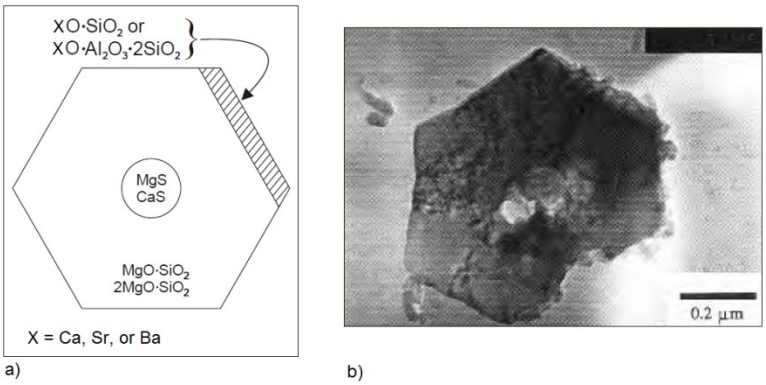

Figure 36 - a) Schematic representation of a nucleus particle containing complex sulfide and oxide phases after nodularizing and inoculation of ductile iron; b) Transmission electron micrograph of duplex sulfide/oxide inclusion in ductile iron [44].

The nucleation and growth of primary graphite particles in the liquid, will start at the available nucleus once the melt temperature goes bellow the graphite liquidus temperature for a given melt composition. Due to the addition of Mg to the melt of ductile iron (to reach final content between 0,04% to 0,06%), used to react and reduce the concentration of O and S, the growth of the graphite particles is assumed to the preferential on the direction $[1\,0\,\bar{1}\,0]$, which will cause the graphite particles to have a circumferential growth and, therefore, to have a nodular shape right after precipitation from the liquid [3] [45] [46].

According to Lesoult et.al [34] model, on the description of pro-eutectic stage of solidification of hypereutectic cast irons based on previous models from Oldfield [47], after nucleation from the liquid phase and upon further cooling of the melt, the graphite particles will continue to grow due to the diffusion of carbon from the liquid to the surface of the graphite particle. This migration of the carbon particles from the liquid surrounding the graphite particle to the particle itself, will cause a change in carbon content of the melt close of the nodule, illustrated in the **Figure 37**.

At the figure, the carbon content in the melt (w^{i}_{C}) is represented as being lower close to the graphite particle when compared to the bulk melt content (w^{00}_{C}), during the time of growth of the particle.

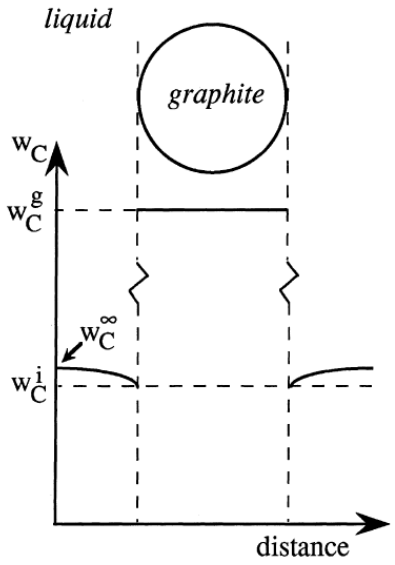

Figure 37 - Illustration of the variation of the carbon content in the liquid close to a pro-eutectic graphite particle [34].

As the melt continues to cool down, the graphite particles will continue to grow and the liquid melt will progressively lose carbon. This variation of carbon in the liquid melt during cooling will approximately follow the graphite liquidus line. The deviation from the real variation of carbon in the melt and the graphite liquidus line is due to the undercooling and real diffusion coefficients of elements in the melt, that do not match the ones from the original Fe-C equilibrium diagram, as represented schematically in **Figure 38a**. Using this same figure as reference, it is comprehensive that the growth of graphite will proceed until the melt temperature reaches the extrapolation of the austenite liquidus line. Once this line is reached, the pro-eutectic graphite particles will be readily encapsulate by an austenite shell and further growth of the graphite particle will only be possible due to diffusion of carbon atoms through the austenite capsule. Also at that point, further undercooling might be necessary to originate the necessary driving force for the start of the eutectic transformation, after which the thermal analysis curve will reveal a recalescence, typical from the eutectic phase transformation [34].

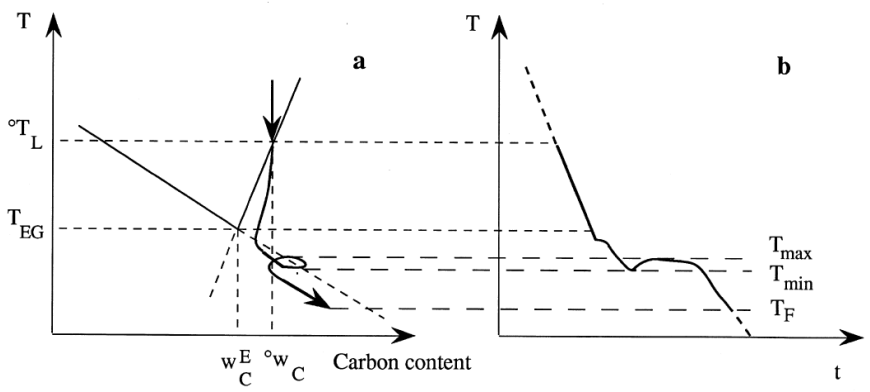

Figure 38 - Schematic of the hypereutectic solidification of ductile iron a) solidification path in the FeC diagram, b) proposed cooling curve [34].

Although the above description of the hypereutectic solidification of cast iron is in agreement with the phase transformation steps of the Fe-C equilibrium diagram, it does not include a verification made by several researchers (Lesoult et.al [34], Rivera et.al [48], Yeung et. al. [49]) for the presence of off-eutectic austenite, often in a dendrite shape, in cast iron with hypereutectic compositions that solidify in non-equilibrium conditions (see **Figure 39**). The microstructure is then formed by a complex coexistence of primary graphite nodules, austenite shells surrounding the graphite particles (both primary and eutectic) and independent primary austenite particles, usually dendritic [50].

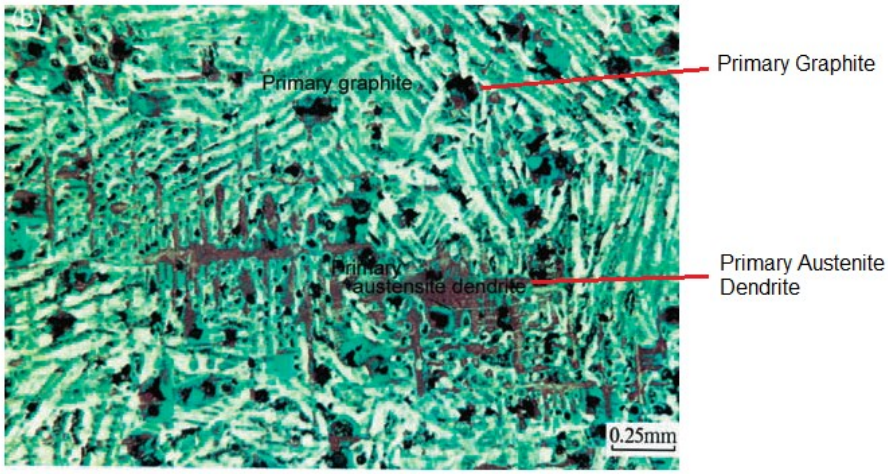

Figure 39 - Non equilibrium structure of hypereutectic cast iron, revealed by color etching, revealing both primary nodules and primary dendritic structure [39].

The non-equilibrium solidification of hypereutectic cast iron can be explained using the concept of the eutectic coexistence region, represented in **Figure 40**. The difference between the solidification processes described earlier for the **Figure 38** and now, is that when the temperature undercools bellow the extrapolated austenite liquidus line, due to the deviation to the right of the eutectic coexistence region, there is a primary solidification of austenite (point 2 in **Figure 40**), instead of the presumable solidification of the eutectic phase. This will cause the off-eutectic austenite to nucleate and grow. As this off-eutectic austenite grows the carbon concentration on the remaining liquid will increase and it will later enter in the eutectic coexistence region (point 3 in **Figure 40**) and the eutectic transformation will take place [34] [39] [50].

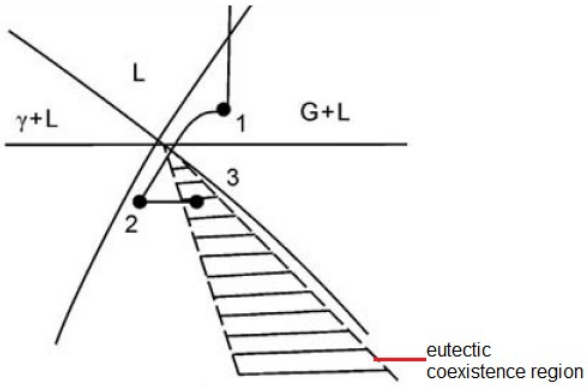

Figure 40 - Representation of the non-equilibrium solidification diagram showing the solidification path of a hypereutectic cast iron [39].

3.3.4. Nucleation and growth of eutectic phase

According to its definition, the stable eutectic transformation refers to the solidification of the liquid in two distinct phases: graphite and austenite.

The literature defines that eutectic solidification in cast irons can occurs following one of three different mechanisms, according to their growth morphology. The eutectic transformation can be:

- Regular Cooperative Growth: the two solid phases of the eutectic grow together as a diffusion couple, with the same growth velocity. This is typical for white cast irons.
- Irregular Cooperative Growth: the two solid phases of the eutectic grow together as a diffusion couple, with different growth velocity. This is typical for lamellar cast iron.

- Divorced Growth: the two solid phases of the eutectic grow separately; there is no direct exchange of solute between the two solid phases and no trijunction (austenite/graphite/liquid). This is typical for nodular cast irons.

In the case of nodular cast iron, the divorced eutectic is characterized by the independent growth of both austenite and graphite phases [3] [51].

The solidification of the eutectic is therefore characterized by eutectic austenite dendrites, independent graphite nodules in the early stage of solidification and combined austenite and graphite cells. The austenite grows always in contact with the liquid, but the graphite only grows in contact with the liquid for a very limited time after nucleation (like the one described for primary graphite particles in the previous chapter). As the graphite particle grows above a diameter of approximately 10 to 15 μm, it will be enveloped in an austenite shell that will isolate the particle from the liquid, and further growth will only be possible by solid-state diffusion of carbon from the liquid to the graphite particle through the austenite shell [32]. **Figure 41** shows the changes of carbon content in the melt around the graphite particle and through the austenite shell. At the graphite particle the carbon content is 100% until the austenite shell. In the austenite shell the carbon content is much lower, and at the graphite/austenite interface it has a concentration given by the solidification's diagram line of the austenite field below the eutectic temperature (point "e" on **Figure 41a**) and close to the austenite/liquid interface is given by the extrapolation of the solidus line of the austenite below the eutectic point (point "d" on **Figure 41a**). The carbon content in the austenite therefore increases from the austenite/graphite interface to the austenite/liquid interface. At the liquid close to the austenite/liquid interface the carbon concentration will be the one from the eutectic point [39].

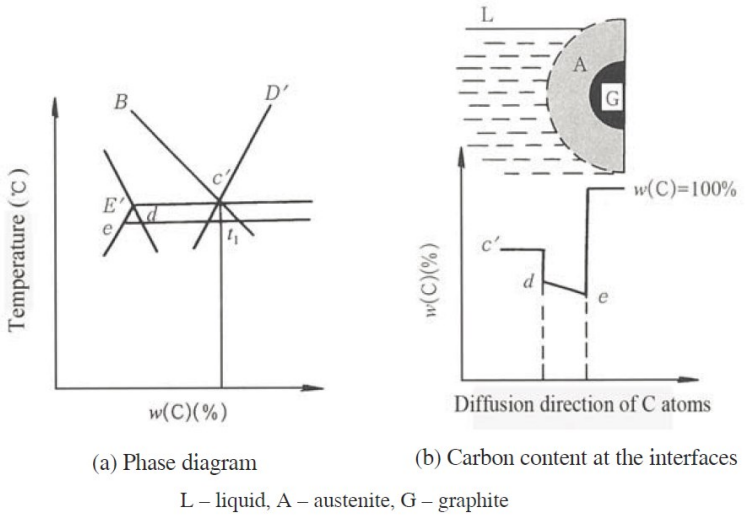

Figure 41 - Representation of the carbon content variation from the graphite particle, austenite shell and bulk liquid melt [39].

The concept that graphite nodules nucleate first in the melt and are later surrounded by austenite during the eutectic solidification was first described by Patterson and Scheil in 1949. It was later determined by Scheil and Hütter [52] that the ratio between the diameters of the austenite shell and the graphite particle tend to remain constant at 2,3. But through time other theories have been formulated in the attempt to better describe the phenomenon of eutectic solidification of nodular iron [45].

In 1972, Wetterfall et al, created a model to describe the eutectic solidification with the assumption that graphite particles nucleate between the dendrite arms and grow freely until they collide with the arm of a dendrite, due to flotation of the particle or convection currents. It is at that point, when there is a collision, that the dendrite arm is presumed to envelope the graphite particle in austenite [51]. Following this theory, Lesoult et.al [34] further developed an existing analytical model to describe the solidification of off-eutectic austenite by modification of the mass balance equation in the carbon diffusion model for nodular iron.

Based on these models, Stefanescu [32] created a more advanced one to describe the eutectic solidification of nodular iron, illustrated in **Figure 42**.

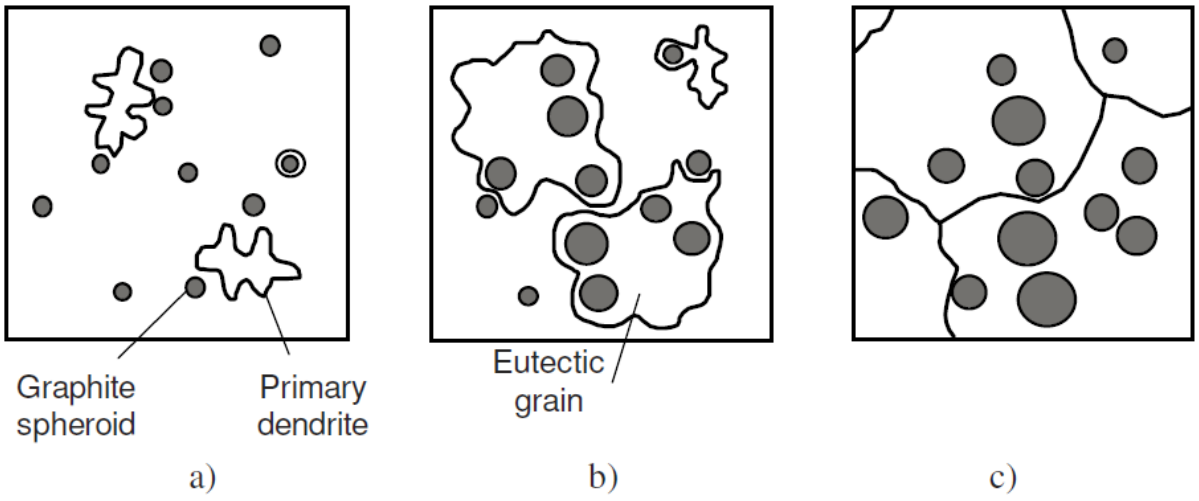

Figure 42 - Illustration, according to Stefanescu, of the sequence of formation of eutectic grains in Nodular iron in case of continuous cooling solidification [32].

According to Stefanescus's model, at the beginning of the eutectic transformation, both austenite dendrites and graphite particles nucleate independently in the melt (**Figure 42a**). As solidification proceeds, the dendrites continue to grow and the graphite particles may be enveloped by an austenite shell. At the dendritic coherency point, it is believed that the interaction between the graphite particles and the austenite dendrites take place. The interaction of the austenite dendrites and the graphite particles can result in the incorporation of more than one nodule in one austenite grain (**Figure 42b**). This incorporation is considered to take place by a mechanism denominated by particle engulfment and pushing (PEP).

A particle may be engulfed by the growing dendrite into the side of the dendrite arm, or through the splitting of the dendrite tip. The pushing occurs when the particle is pushed in the interdendritic region and entrapped in the LTF (last freezing zone). Also in this model, once a graphite particle is enveloped in austenite, further growth is only possible through solid-state diffusion of carbon from the liquid through the austenite shell to the graphite particle. The first particles to be incorporated are expected to be the ones that have the longest time to grow and will became the largest nodules. The smaller graphite particles are the ones that grow later and will be enveloped later, being found close to the austenite crystal's boarder. At the end of solidification (**Figure 42c**) the eutectic grains (austenite + graphite) will meet each other and the reaming liquid (LTF) will solidify completing the solidification process.

3.3.4.1. Envelopment of graphite particles by austenite shell

It seems consensual that, graphite nodules are always enveloped in an austenite shell during eutectic solidification. Nevertheless, the size or ratio between the austenite shell radius (rg) and the radius of the graphite particle enveloped (r_{Gr}) is not. Studies made by Scheil and Hütter [52] and used by Lesoult et al. consider this ratio to be 2,3 (rg/ r_{Gr}), and works performed by Nakae et. al. [40] indicate ratios of 1.4 (rg/ rGr). Once the graphite particle grows due to solid-state diffusion of carbon through the austenite shell, it is expected that the size of the austenite shell will influence the growth rate (also called graphitization) of the graphite particle. The bigger the austenite shell is, the lower will be the graphitization of the graphite particles [40].

Based on several microstructure observations, Zhou [39] has described in more detail the possible mechanism of austenite shell formation around a graphite particle, considering cases where the envelopment of the particle does not occur by engulfment, presented in **Figure 43**. This model describes that after the formation of the graphite nodule (**Figure 43a**), there is the formation of a carbon depletion zone around the nodule and subsequent enrichment in Si (**Figure 43b**). Afterwards there is the heterogeneous nucleation of austenite particles using available nucleus around the graphite particle or using the graphite particle surface itself (**Figure 43c**), and will grow in a dendritic form that, will rapidly merge forming individual austenite grains (**Figure 43d**). These grains will afterwards coarse and form a whole austenite grain (**Figure 43e**).

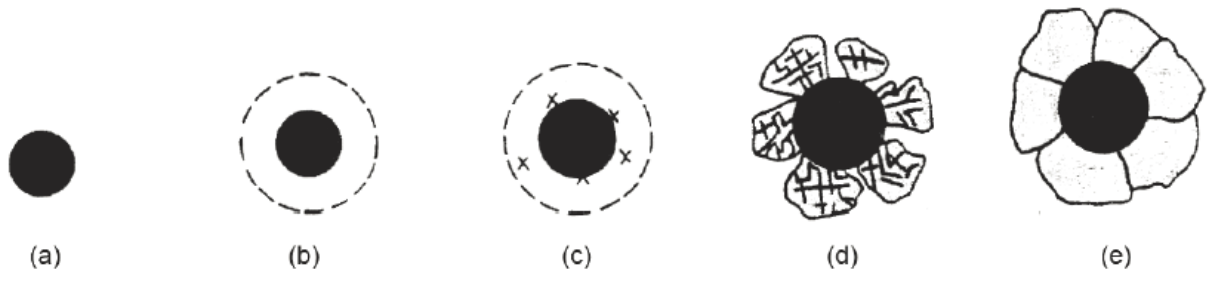

(a) Graphite forms a spheroid; (b) Carbon-depletion region forms; (c) Austenite nucleates; (d) Austenite grows in the form of dendrites, which join each other and broaden; (e) Close halo forms

Figure 43 - Illustration of the sequence of austenite shell formation around a graphite particle [39].

Once the nodules are reported to be readily surrounded by the austenite shell when they reach a diameter of 10 to 15μm, and at the end of the solidification (end of the eutectic reaction) and assuming that they will have a final diameter that can range from 50 to 100μm, most of the graphite particle growth occurs after envelopment by austenite. Carbon diffusion through the austenite is calculated to be 20 times slower than through the liquid, meaning that the growth rate of the graphite particle is very slow, especially when compared to lamellar graphite where the growth of the graphite particle is made in direct contact with the liquid.

Due to this growth rate difference of graphite when in contact or not with the liquid and based on the observation of several microstructures that resulted in the illustration from **Figure 43**, the shape of the graphite particle can be affected by the austenite shell. Once the shell is formed by grains (**Figure 43d**) before they form the compact shell (**Figure 43e**), during the time the individual grains exist, there will be liquid between the grains and local graphite/liquid interface will exist. This means that the growth rate of the graphite will be higher in those contact regions and the shape of the graphite will departure from the usual nodular shape. Therefore the time of enveloping of the graphite particle may influence also the shape of the graphite particle itself. Zhou et al. [53] proposed three methods of graphite envelopment by austenite based on the envelopment speed, presented in **Table 4**.

The first model, fast enveloping (1), is frequently observed in castings with rapid cooling rate or high particle density, where a austenite shell forms rapidly around the graphite particle. The growth rate of the graphite particle through diffusion of carbon in the austenite shell will be the same all around the shell and the particle grows as a sphere.

Slow enveloping (2) happens in castings with slow cooling rate and is characterized by a delay on the closure of the dendrite grains around the nodule that will form gaps and channels of liquid melt that will contact directly with the graphite. The resulting graphite particle will have an irregular shape, revealing protuberances on the sites where the gaps of the austenite shell existed.

The extreme case in the one of no complete envelopment (3) of the graphite particles, resulting in the directional growth of the graphite particles, made in constant contact with the liquid until the end of solidification. This case is the one that presents higher deformation of the graphite particles.

The speed of the austenite shell envelopment is considered to be influenced by the cooling speed, inoculation of the melt (number of nucleation sites for graphite particles), which when increased will promote fast envelopment of the graphite particles, and same critical chemical elements concentration such as Al, Sn, Sb, Pb and Bi that when increase will promote slow envelopment.

Table 4 - Relation between the graphite particle shape and the envelopment speed of those particles by a austenite shell [53].

Austenite shell	Graphite formation process	Graphite shape
(1) Fast enveloping		
(2) Slow enveloping		
(3) No enveloping		

The same authors also instigate about the fact that these fast or slow envelopment of the graphite particles will affect the overall expansion due to graphite growth speed during solidification.

3.3.4.2. Solidification of residual interdendritic melt (LTF)

The last freezing zones (LTF) correspond to the portion of liquid that is present at the intercellular regions when the eutectic solidification is coming to an end, and will therefore be the last liquid to solidify. These regions are the ones where all segregations (chemical elements with positive segregation factor or impurities contained in the melt) concentrate and also where more defects are found. Among the possible defects that can occur in these regions, we can find intercellular carbides, inclusions, distorted graphite and even small porosity cavities [53].

3.3.5. Basic consideration on macrostructure solidification of nodular cast iron

Due to its microstructure solidification characteristics, high undercooling and divorced eutectic morphology with the formation of dendritic structure in the bulk liquid, nodular iron is classified to undergo a mushy solidification type (**Figure 44b**), in opposition to lamellar graphite cast iron that has a skin or shell solidification type (**Figure 44a**) [45] [54].

This means that during solidification, in ductile iron, the formation of primary solidified particles will start randomly in the liquid, while in lamellar graphite cast iron the solidification will start in the periphery of the liquid volume forming a shell and will then proceed forward in the opposite direction to the heat flow [36].

Figure 44 - Illustration of the macrostructure of eutectic solidification morphology of lamellar (left) and nodular (right) graphite cast iron [45].

Nevertheless, also in nodular cast irons, the solidification of the liquid mass will start at places where the liquid cools faster, but unlike the lamellar graphite cast iron, no significant shell type solidification will occur. The absence of shell type solidification in nodular cast irons will, for example, lead to a loss of graphite expansion volume from early solidified nodules if the feeder necks are not frozen at that time, leading to additional shrinkage [32].

The S/L interface of the solidification front of nodular cast iron (SG in **Figure 45**) is also classified as being of irregular shape [45].

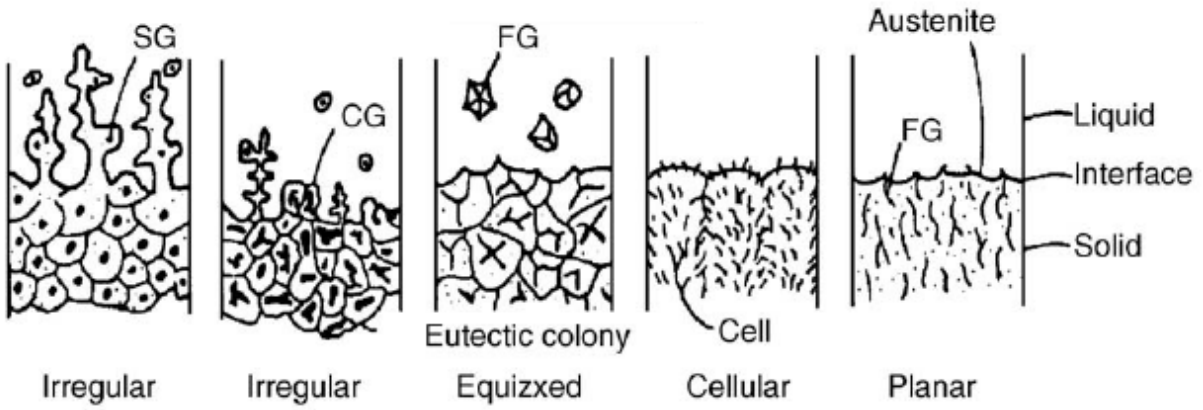

Figure 45 - Schematic representation of the S/L solidification front for different cast iron alloys [45].

This mushy type solidification and irregular S/L interface are associated to several difficulties in performing proper feeding of the castings during solidification, as well as the formation of shrinkage and porosity defects [45] [39] [54].

3.4. Classification of melt shrinkage defects in cast iron

3.4.1. Liquid contraction and feeding

Solidification is characterized by having three contraction stages, represented in **Figure 46**. Liquid contraction occurs before the beginning of solidification and is influenced by the pouring temperature, because the melt contracts as the temperature decreases. High pouring temperature for the same alloys, will results in higher liquid contraction volume. Solidification contraction occurs during the liquid/solid transformation and solid contraction that occurs during further cooling of the already solid material. From the three contractions stages, solidification contraction is the one with the highest volume variation, followed by liquid contraction and finally solid contraction [32].

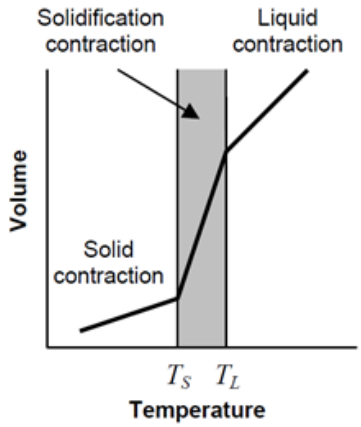

Figure 46 - Representation of the three volume contraction steps during solidification [32].

However, in the case of cast irons, this contraction concept is more complex due to the precipitation of graphite during solidification. **Table 5** shows the volume density of the different phases involved in the stable and metastable solidification of cast iron, where we can observe that the transformation of Liquid/Austenite will involve a contraction once the specific volume from austenite is smaller than the one from liquid. The same happens if iron carbides are the solidification product from liquid iron. However, the graphite has a specific volume that is 3,5 times higher than the specific volume of liquids iron. This means that during the solidification of graphite, there will be an expansion phenomenon related to the growth of graphite particles.

Table 5 - Density of the different phases involved in the solidification of cast iron [54] [55].

Phase	Specific volume [cm^3/g]
Liquid cast iron [3,9%C at 1450°C]	0,143
Austenite (g-Fe) [20°C]	0,136
Graphite (C) [20°C]	0,448
Iron carbides (Fe_3C) [20°C]	0,130

Depending on the amount of graphite that solidifies and the time of occurrence of this expansion, the overall solidification contraction can be positive (decrease of volume) or negative (increase of volume). According to **Table 6**, ductile iron can have a volumetric solidification contraction from -4,5% to 2,7%. In comparison to grey cast iron, nodular cast iron has a higher volumetric solidification contraction [32].

Table 6 - Solidification contraction of several metals and alloys [32].

Material	Volumetric solidification contraction, %	Material	Volumetric solidification contraction, %
carbon steel	2.5 to 3	Cu-30%Zn	4.5
1% carbon steel	4	Cu-10%Al	4
white iron	4 to5.5	aluminum	6.6
gray iron	-2.5 (expansion) to 1.6	Al-4.5%Cu	6.3
ductile iron	-4.5 (expansion) to 2.7	Al-12%Si	3.8
copper	4.9	magnesium	4.2
		zinc	6.5

In order to compensate liquid contraction and solidification contraction, castings need to have a feeding system which supplies additional melt volume than the one needed to fill the casting's mould cavity. **Figure 47** shows a model proposed by Campbell in 1969, for the feeding mechanisms considering the macro-solidification model of an alloy. The model considers 4 different feeding mechanisms. *Liquid feeding* occurs in before the solidification starts and the liquid melt has high fluidity through the casting cavity. *Mass feeding* occurs at the early stages of solidification and is characterized by a decrease of the melt fluidity due to the presence of small solid particles in the liquid, marking the appearance of the mushy zone. Once dendritic coherency occurs, the *interdendritic feeding* mechanism starts, where the flow of the melt is highly conditioned (feeding velocity will decrease) by the presence of a solidified "skeleton" structure and the flow of melt is only possible between the interdendritic spaces of that solid structure. Once the melt has solidified, no more feeding of liquid melt is possible and only limited *solid feeding* is likely through elastic and plastic deformation of the metal [32]. The point of dendritic coherency is often considered in literature as the most critical point in the feeding of a casting because it is the one where more constrains to the melt fluidity and feeding velocity are imposed.

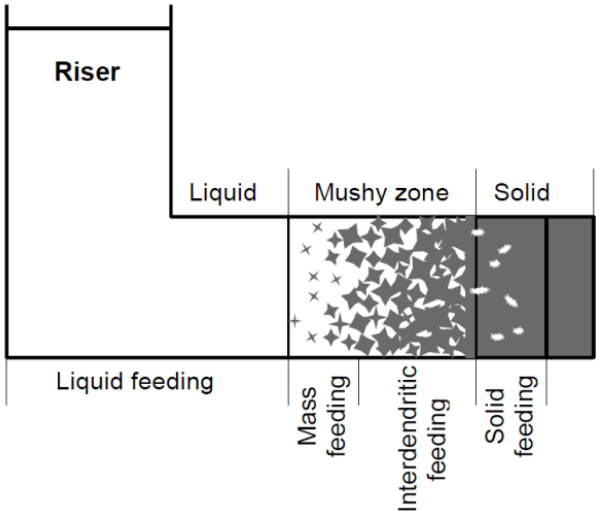

Figure 47 - Illustration of the macro-solidification and related mechanisms of feeding [32].

3.4.2. Terminology for classification of shrinkage defects

The classification of shrinkage defects in castings is not consensual, concerning the terminology used. Often, different researchers and foundries classify the same defects using different classification methods and terminology.

According to Stefanescu [32] shrinkage defects are classified in two distinct groups, presented in **Figure 48** : open shrinkage (macroshrinkage) and closed shrinkage defects (shrinkage porosity).

Open shrinkage defects are characterized by shrinkage cavities that are in contact with the surface of the casting and can have a pipe shape or simply a caved surface (on the side or top surface of the casting). These defects are a consequence of metal contraction during cooling in the liquid state (caved surfaces) and during solidification (pipe shape).

Closed shrinkage defects are characterized by not having contact with the casting surface and are formed due to metal contraction during the solidification, as a consequence of the mushy zone. According to the size of the shrinkage defect, it can be classified as macroporosity when the defect is a single big shrinkage volume (see **Figure 49**) or microporosity/microshrinkage when the cavities are small and interconnected (interdendritic cavities, see **Figure 50**).

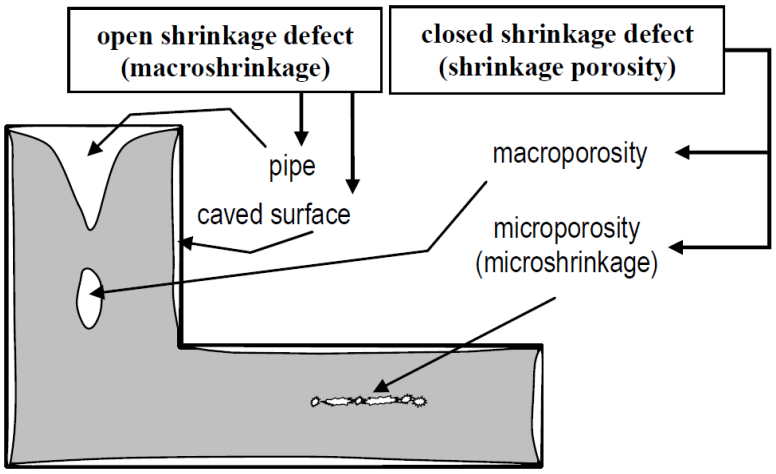

Figure 48 - Classification of shrinkage defects [32].

Hasse [54] presents in his book, a similar classification to the one made by Stefanescu, apart from the difference in the terminology from the bigger closed shrinkage volume, which Hasse classifies as "internal shrinkage", and he distinguishes microshrinkage from microporosity, considering that microporosity is a smaller scale of microshrinkage defects, but where the causes of these defects can be the same.

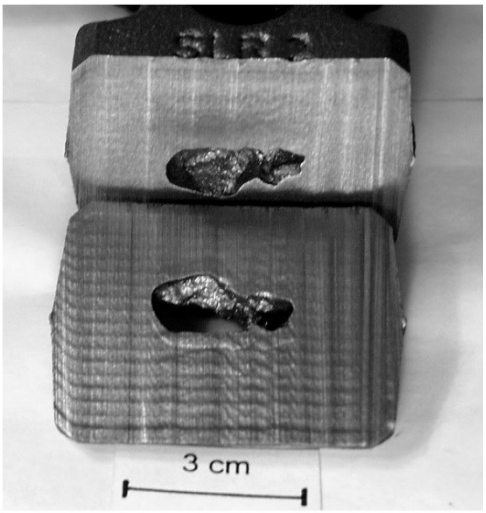

Figure 49 - Macroshrinkage in a nodular iron casting, in the in-gate area [54].

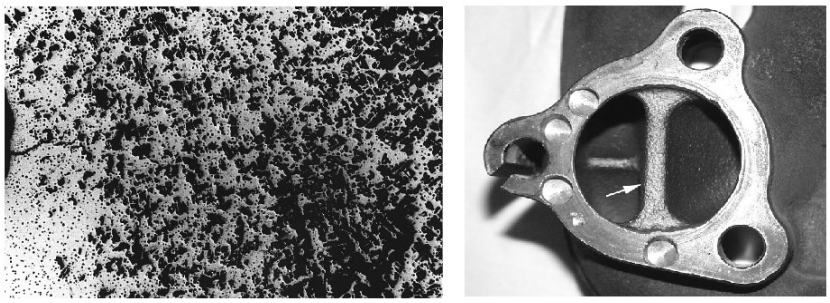

Figure 50 - On the left a micrograph of a nodular iron casting sample showing interdendritic microporosity (10x magnification without etching). On the right, the same casting, showing the local where the microporosity was found.

3.5. Application of thermal analysis techniques to nodular cast iron production

Thermal analysis can be defined as *"... the analysis of a change in a sample property*[10]*, which is related to an imposed temperature alteration.*" [56].

The thermal analysis is performed, in the field of foundry metallurgy, by acquisition of a cooling curve (temperature/time curve) from a sample of liquid melt that cools down until solidification is complete or until room temperature, depending on the sample's properties that are under investigation, through the use of a thermocouple immersed in the sample. This cooling curve expresses the balance between the evolution of heat in the sample and the heat transport away from the sample.

During cooling of a melt, without any melt property change, the heat transport must be equal to the evolution of heat in the sample (once the melt is cooling, the heat evolution will be negative). The cooling curve will be characterized by a temperature decrease over time, with a given slope (dT/dt). The heat transport (dQ/dt) in these conditions is calculated by **Equation 5**, where V is the sample's volume, ρ is the density of the melt and C_p is the heat capacity. The heat transport must be equal to the heat evolution in the sample. Before and after solidification process this is balanced by the loss of heat capacity.

$$\frac{dQ}{dt} = V \times \rho \times C_P \times \frac{dT}{dt} \quad \text{(Eq. 5)}$$

[10] "sample property" is considered to include thermodynamic properties, materials properties, chemical composition or structure, according to the bibliographic reference [56] .

During solidification, the transition from liquid to solid involves the release of latent heat of solidification (ΔH). Therefore, during solidification the previous equation has to consider the solidification phenomenon occurring in the melt and will be written as **Equation 6**, to include a term that reflects the solid phase forming in the liquid.

$$\frac{dQ}{dt} = \left(V \times \rho \times C_P + \rho \Delta H \frac{df}{dT}\right) \times \frac{dT}{dt} \quad \textbf{(Eq. 6)}$$

The volume fraction of solid formed at a changing temperature (df/dT) and the associated latent heat of solidification will now affect the cooling rate of the sample (dT/dt) for the same heat transport. This means that the higher the rate of increase of solid volume fraction (df/dT), the smaller will be the slope (dT/dt) of the cooling curve. Thus, in the cooling curve, a plateau will appear corresponding to the solidification process of a crystal from the melt. The identification of these plateaus for different melt compositions is in the base of the formation of the phase diagram, as illustrated in **Figure 51**, where the liquidus line for the phase diagram was obtained based on the evolution of the primary solidification plateaus from cooling curves with different composition of element A and B [3].

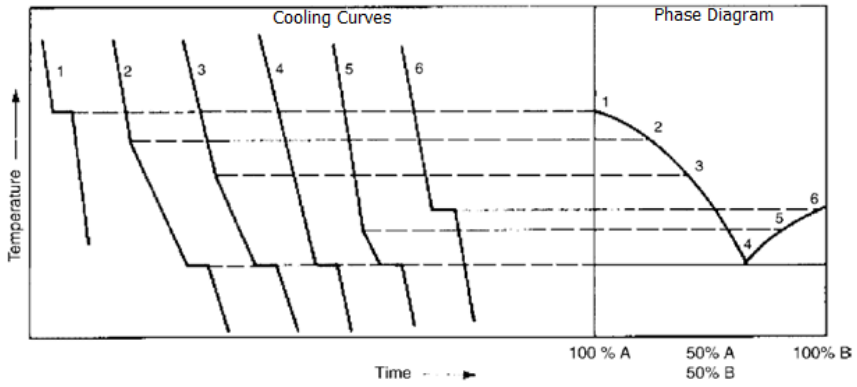

Figure 51 - Illustration of the relationship between the cooling curves and the phase diagrams (example for an alloys A-B) [3].

According to **Equation 6**, the reduction on the slope of the cooling curve, that forms the plateau, will depend on the nature of the crystal being solidified due to his specific latent heat of solidification (ΔH) and volume fraction of solid formed at changing temperature (df/dT). These characteristics are different between different crystals, and therefore, through the evaluation of

the cooling curve it is possible to establish a relationship between the points in the curve and the solidification sequence of the different phases.

3.5.1. Nomenclature of cooling curves for thermal analysis

Modern thermal analysis techniques, use not only the cooling curve (temperature/time) acquired from a sample in solidification, but also its 1st (dT/dt) and 2nd (d^2T/dt^2) derivative (see **Figure 52**) [57].

In **Figure 52**, the 1st derivative of the temperature/time curve is presented as the inverse (-dT/dt), following the curve analysis method of the company OCC GmbH, that was used for all thermal analysis tests performed in this work.

On the cooling curve and derivatives, all plateaus, maximum and minimum points and sometimes difference between points are identified by a name or abbreviation. The identification of main points and their meaning is presented in **Table 7**.

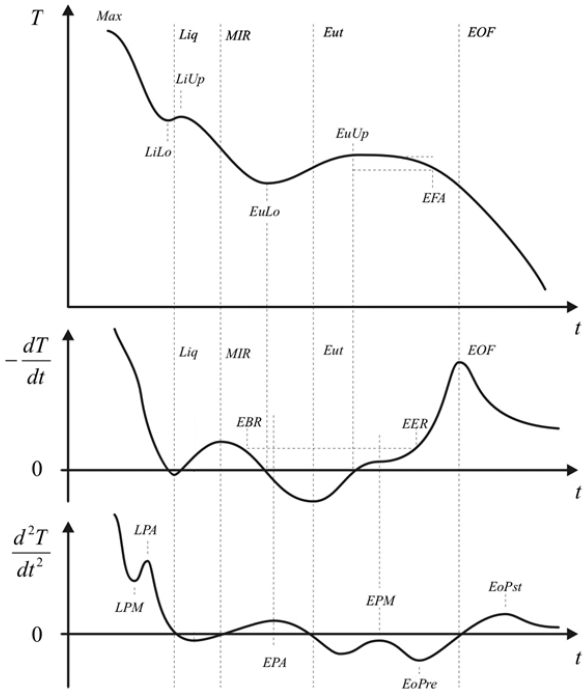

Figure 52 - Illustration of the temperature/time curve and main points, together with the 1st and 2nd derivative [57].

Table 7 - Nomenclature and definition of the points from a cooling curve and its 1st and 2nd derivative [57].

Name	Unit	Signification	Identification of the points according to the thermal analysis software PhaseLab (presented graphically in attachment ?)		
			Name/Abbrev.	Unit	Signification
Max (Maximum)	[°C]	Maximum temperature measured by the thermocouple.	MAX	[°C]	Temperature at MAX point
			MAX_Z	[s]	Time at MAX point
LPM	[°C/s^2]	Minimum at the 2nd derivative before the liquidus point.	PRE_LIQ_MIN_A	[°C]	Temperature at LPM point
			PRE_LIQ_MIN_A_Z	[s]	Time at LPM point
			PRE_LIQ_MIN_A_ROC	[°C/s]	Cooling rate at LPM point
			PRE_LIQ_MIN_A_T2	[°C/s^2]	LPM point on the 2nd derivative curve
LPA	[°C/s^2]	Highest temperature acceleration before the liquidus point.	PRE_LIQ_MAX_A	[°C]	Temperature at LPA point
			PRE_LIQ_MAX_A_Z	[s]	Time at LPM point
			PRE_LIQ_MAX_A_ROC	[°C/s]	Cooling rate at LPA point
			PRE_LIQ_MAX_A_T2	[°C/s^2]	LPA point on the 2nd derivative curve
LiLo (Low liquidus)	[°C]	Minimum temperature measured before the liquidus point.	LIQ_LO	[°C]	Temperature at LiLo point
			LIQ_LO_Z	[s]	Time at LiLo point
Liq (liquidus)	[°C]	Liquidus temperature corresponding to the local minimum at the 1st derivative.	LIQ	[°C]	Temperature at Liq point
			LIQ_Z	[s]	Time at Liq point
			LIQ_ROC	[°C/s]	Cooling rate at Liq point
LiUp (Upper liquidus)	[°C]	Maximum temperature measured before the liquidus point.	LIQ_UP	[°C]	Temperature at LiUp point
			LIQ_UP_Z	[s]	Time at LiUp point
MIR	[°C]	Temperature between the liquidus and eutectic point with the highest cooling rate (maximum in the 1st derivative)	MIR	[°C]	Temperature at MIR point
			MIR_Z	[s]	Time at MIR point
			MIR_ROC	[°C/s]	Cooling rate at the MIR point
EPA	[°C]	Highest temperature acceleration before the eutectic temperature (max. in the 2nd derivative curve)	EUT_PRE_MAX_A	[°C]	Temperature at EPA point
			EUT_PRE_MAX_A_Z	[s]	Time at EPA point
			EUT_PRE_MAX_A_T2	[°C/s^2]	Maximum temperature acceleration at point EPA
EuLo (Low eutectic temperature)	[°C]	Minimum temperature measured before the eutectic point	EUT_LO	[°C]	Temperature at EuLo point
			EUT_LO_Z	[s]	Time at EuLo point
			EUT_LO_T2	[°C/s^2]	Temperature acceleration at point Eu_Lo
Eut (eutectic temperature)	[°C]	Eutectic temperature, corresponding to the local minimum in the 1st derivative curve	EUT	[°C]	Temperature at EuLo point
			EUT _Z	[s]	Time at EuLo point
			EUT_ROC	[°C/s]	Cooling rate at the Eut, point
EuUp (Upper eutectic temperature)	[°C]	Maximum temperature measured after the eutectic point	EUT_UP	[°C]	Temperature at EuUp point
			EUT_UP_Z	[s]	Time at EuUp point
			EUT_UP_T2	[°C/s^2]	Temperature acceleration at point Eu_Up
EPM	[°C/s^2]	Smallest temperature acceleration after the eutectic temperature (Minimum in the 2nd derivative curve)	EUT_PST_MAX_A	[°C]	Temperature at EPM point
			EUT_PST_MAX_A_Z	[s]	Time at EPM point
			EUT_PST_MAX_A_T2	[°C/s^2]	Minimum temperature acceleration at point EPM
EBR	[°C]	Beginning of the eutectic transformation, considering a underrun of a given cooling rate (Standard:0,5°C/s) before the eutectic point	EUT_BEG_BY_ROC_	[°C]	Temperature at EBR point
			EUT_BEG_BY_ROC_Z	[s]	Time at EBR point

EER	[°C]	End of the eutectic transformation, considering a trespass of a given cooling rate (Standard:0,5°C/s) after the eutectic point	EUT_END_BY_ROC_	[°C]	Temperature at EER point
			EUT_END_BY_ROC_Z	[s]	Time at EER point
EFA	[°C]	Fade of the eutectic transformation, considering a given temperature decrease (Standard:5°C/s) after the EuUp point	EUT_FAD_BY_DT_	[°C]	Temperature at EFA point
			EUT_FAD_BY_DT_Z	[s]	Time at EFA point
EoPre	[°C/s^2]	Maximum temperature acceleration before the end of freezing (EoF) point.	EOF_PRE_MAX_A	[°C]	Temperature at EoPre point
			EOF_PRE_MAX_A_Z	[s]	Time at EoPre point
			EOF_PRE_MAX_A_ROC	[°C/s]	Cooling rate at EoPre point
			EOF_PRE_MAX_A_T2	[°C/s^2]	Temperature acceleration at EoPre point
EoF (End of freezing)	[°C]	Estimated point of end of solidification, characterized by a maximum in the inverted 1st derivative curve	EOF	[°C]	Temperature at EoF point
			EOF_Z	[s]	Time at EoF point
			EOF_ROC	[°C/s]	Cooling rate at EoF point
EoPos	[°C/s^2]	Minimum temperature acceleration before the end of freezing (EoF) point.	EOF_PST_MAX_A	[°C]	Temperature at EoPos point
			EOF_PST_MAX_A_Z	[s]	Time at EoPos point
			EOF_PST_MAX_A_ROC	[°C/s]	Cooling rate at EoPos point
			EOF_PST_MAX_A_T2	[°C/s^2]	Temperature acceleration at EoPos point

Based on the points readily identified from the cooling curve and its derivatives, additional thermal analysis variables can be calculated from them. The most common variables, and corresponding formulas, are presented in **Table 8**.

Table 8 - Additional thermal analysis variables calculated from the basic cooling curve points [57].

Name	Unit	Description	Formula
LIQ_RC	[°C]	Liquidus recalescence	$LIQ\_RC = LIQ\_UP - LIQ\_LO$
LIQ_RC_DUR	[s]	Duration of the liquidus temperature recalescence (LIQ_RC)	$LIQ\_RC\_DUR = LIQ\_UP\_Z - LIQ\_LO\_Z$
EUT_UK	[°C]	Eutectic undercooling, determined using the theoretical eutectic stable temperature from the equilibrium phase diagram (THEO_EUT_TEMP.)	$EUT\_UK = THEO\_EUT\_TEMP - EUT\_LO$
EUT_DEP	[°C]	Eutectic depression, determined using the theoretical eutectic stable temperature from the equilibrium phase diagram (THEO_EUT_TEMP.)	$EUT\_UK = THEO\_EUT\_TEMP - EUT\_UP$
EUT_RC	[°C]	Eutectic recalescence	$EUT\_RC = EUT\_UP - EUT\_LO$
EUT_RC_DUR	[s]	Eutectic recalescence duration	$EUT\_RC\_DUR = EUT\_UP\_Z - EUT\_LO\_Z$
EUT_FAD_DUR	[s]	Eutectic fading duration, between the EUT_UP and the EUT_FAD_BY_DT_Z	$EUT\_FAD\_DUR = EUT\_FAD\_BY\_DT\_Z - EUT\_UP\_Z$
DF	[°C]	Delta freezing or temperature interval for eutectic solidification, defined has the temperature difference between the low eutectic temperature and the estimated end of freezing temperature.	$DF = EUT\_LO - EOF$

3.5.2. Interpretation of cooling curves for thermal analysis

The interpretation of cooling curves is made upon a long learning process based on the manipulation of a melt, performance of the thermal analysis test and evaluation of the results. Based on a cause/effect evaluation, between the process data, laboratory results and cooling curve, the meaning of each one of the plateaus from the curves start to be identified.

3.5.2.1. Solidification morphology

In 1974, Loper et.al [58] described the changes caused in the solidification curves by the progressive increase of C.E value (through the simultaneous increase of C and Si content in the melt). The result of that experiment is presented in **Figure 53**, where it is visible that as the C.E. value increases, the first plateau in the cooling curve decreases, and starts to increase again for C.E values over the eutectic point. From these results it could then be defined that the first plateau in the curve corresponded to the liquid temperature and the second to the eutectic (although it most probably represents the metastable eutectic due to the strong presence of carbides reported in the article).

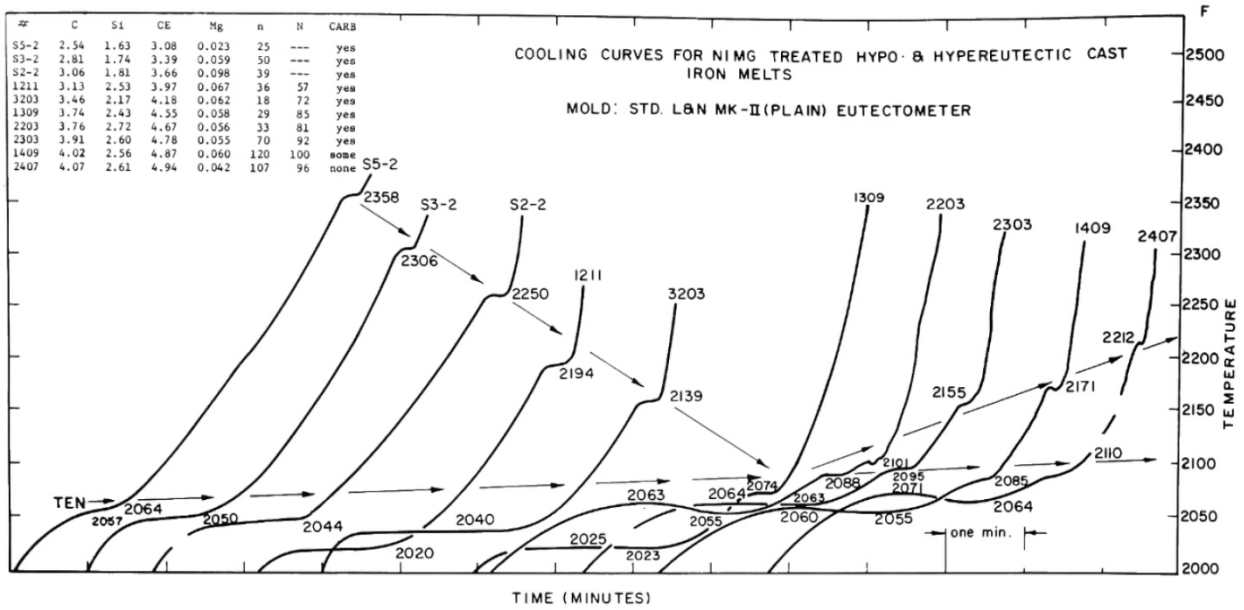

Figure 53 - Change in the morphology of the solidification curve, for CE values ranging from hypoeutectic to hypereutectic, according to experiments performed by Loper et.al [58].

Due to technological improvements over the year, both on the temperature measurement equipment and in computer systems, it is possible to have today a more precise and detailed acquisition of solidification curves.

The solidification morphology of nodular iron curves that, following the stable version of the solidification diagram, can be speculated through the sequence and magnitude of the different plateaus of a cooling curve according to the illustration from **Figure 54**, obtained from closed (constant sample volume) thermal analysis sample cups [59].

The solidification curves from hypoeutectic melts are characterized by two plateaus. The first one is recognizable by having only a slight inflection, that can have no recalescence or a small recalescence of maximum 2°C and that occur in a short period of time (up to 4 seconds). This first plateaus is identified as the liquidus temperature (Liq.). Afterwards the temperature decreases until a second plateau is reached, that is characterized to have a bigger recalescence both in temperature and time, being identified as the eutectic transformation. After this second plateau, the temperature decreases again and the end of freezing is reached [57].

In hypereutectic melts, also two main plateaus are identified, but with opposite characteristics than the ones for hypoeutectic melts. The first plateau has a higher recalescence and the second one is flat (no slope) or has a slight decrease, but never a recalescence and a longer duration than the first one. After the second plateau the end of freezing is reached. The first plateau is considered to be the primary solidification of graphite and the second plateau the eutectic transformation.

The melts with eutectic composition are easily recognizable because they exhibit only one big plateau, corresponding to the eutectic transformation.

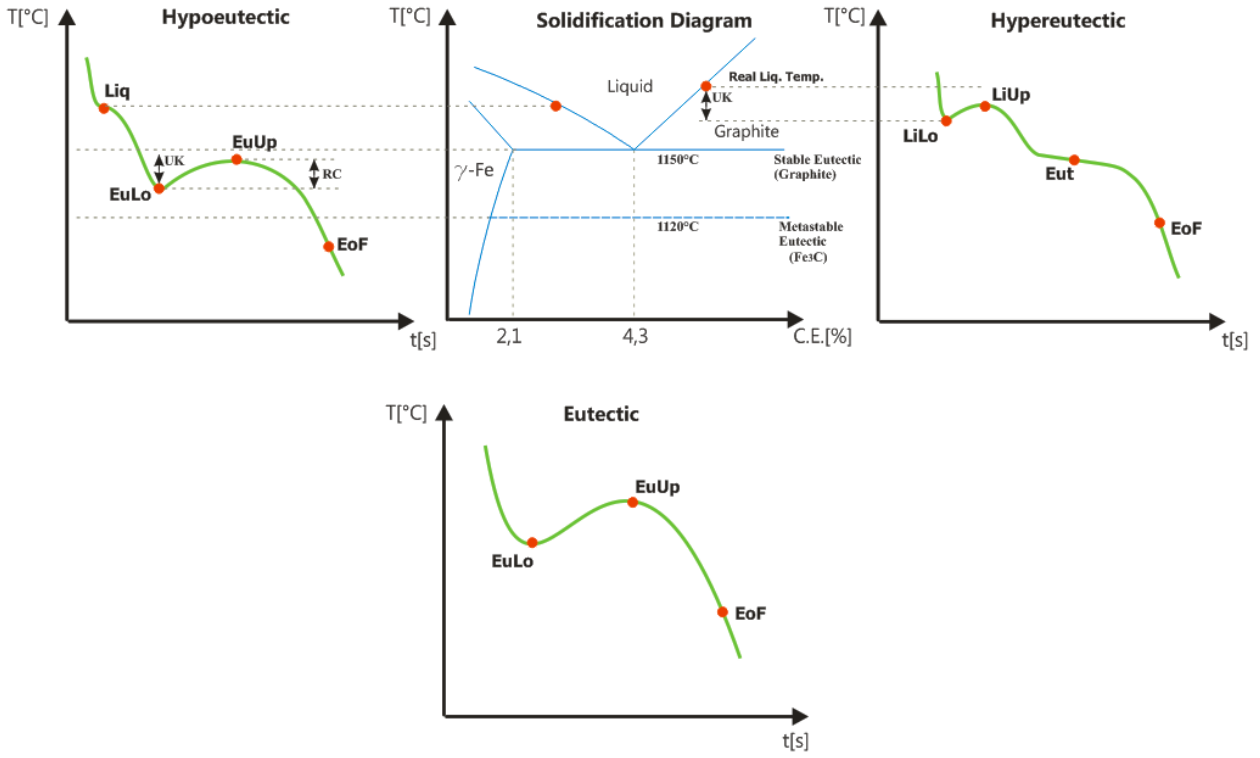

Figure 54 - Illustration of the representative shape of the solidification curves and suggested classification for hypoeutectic, eutectic and hypereutectic solidification morphologies according to OCC GmbH [59].

3.5.2.2. Evaluation of inoculation

Thermal analysis is often used in production of cast iron to perform the evaluation of the inoculation properties of the melt. Through the measurement of the undercooling of the cooling curve on the eutectic plateau, it is possible to estimate if a melt is properly inoculated for the production of a given casting. According to the principles of heterogeneous nucleation, the additions of nucleus to the melt (inoculation) will reduce the required amount of energy to start nucleation, which in the case of graphite precipitation of hypoeutectic and eutectic melts is evaluated by the magnitude of the undercooling [57] [22].

In a nodular iron melt, a non-inoculated curve is characterized by having the eutectic temperature matching the metastable eutectic temperature, as represented in **Figure 55a**, often without any recalescence. The addition of inoculant will make the curve gain same recalescence due to the latent heat of solidification of graphite nucleation and growth, and the eutectic reaction plateau

will raise in temperature, measured by the raise in the low eutectic temperature. **Figure 55b** shows the comparison between two real solidification curves from the same nodular iron melt, where the differences between the two curves result from the use of different inoculants (different inoculation states) that resulted in two different microstructures (microstructure from the thermal analysis sample). The curve with a higher inoculation state (green curve in **Figure 55b**) indicates a microstructure with higher particle density than the one with lower inoculation potential (red curve in **Figure 55b**).

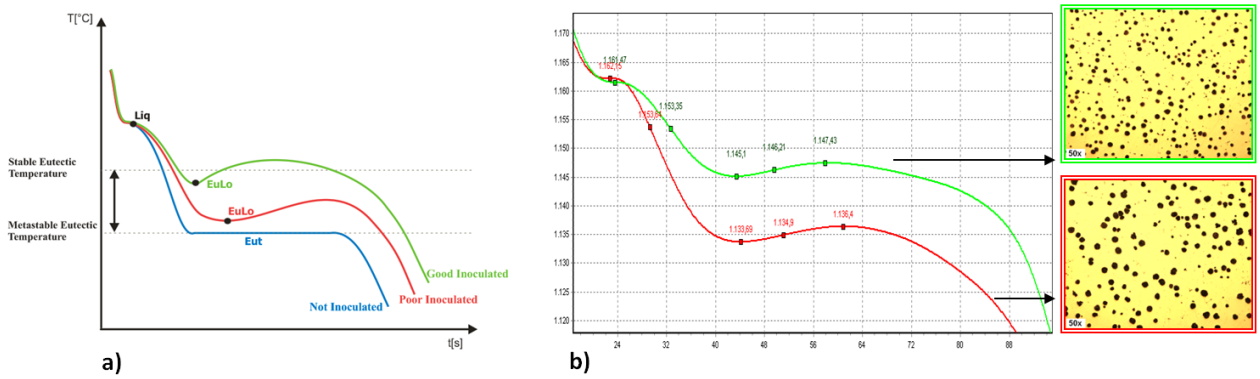

Figure 55 - a) Illustration of the melts inoculation influence in the cooling curves; b) real cooling curve display showing he difference between a cooling curve with low inoculation (red) and with high inoculation (green) state and respective micrographs [22].

3.5.2.3. Prediction of graphite shape

Once cooling curves are sensitive to the phenomenon of nucleation and growth of graphite, many researchers and companies that supply thermal analysis technology to foundries, developed mathematical models that correlate the thermal analysis data with graphite shape. Yearly works from Lopper et al [60] in 1967 showing the influence on the thermal analysis curves of the addition of Cerium to change the lamellar graphite into nodular graphite or in 1971 also by Loper et. al. [61] for the formulation of a mathematical model to predict the nodularity of heavy section ductile iron castings based on thermal analysis, showed the potential of this technique to help foundries in the active control of the final graphite structure during manufacturing. Bäckerud et. al. [62] and Stefanescu et. al. [63] used the same principal applied to the study of compacted graphite cast iron where they revealed that compacted graphite cast iron exhibits a high recalescence in comparison to ductile iron. Recently, Baumgart [57] presented also the

formulation of a mathematical model to estimate the graphite shape in nodular cast iron based on cooling curve analysis with an accuracy of 85% (using only 3 thermal analysis variables). The differences in the cooling curve between lamellar, compacted and nodular graphite cast iron are exemplified in **Figure 56**.

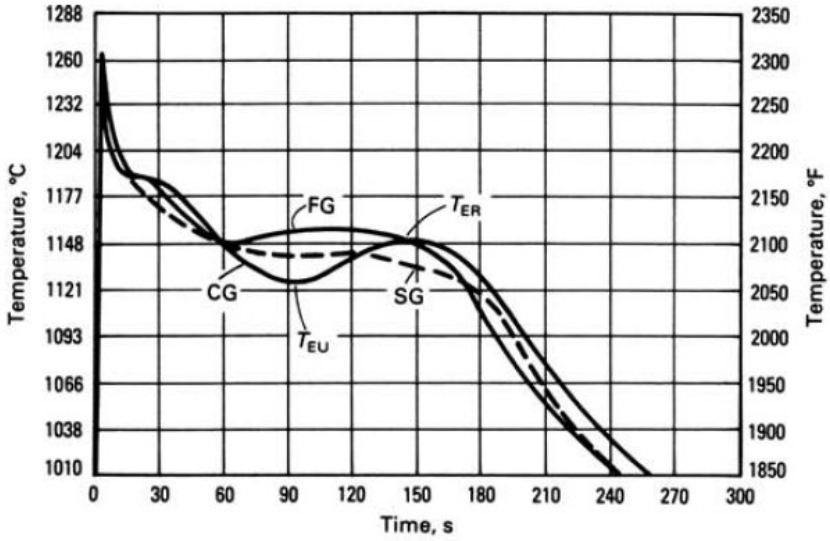

Figure 56 - Cooling curves for hypoeutectic cast iron, showing the differences in the curves for different graphite shapes (FG-lamellar graphite; CG-compacted graphite; SG-Nodular graphite). Teu and Ter represent the low and upper eutectic temperature respectively in the CG curve [3].

Nodular iron melts with good nodularity, are characterized by having small recalescence (from 1°C to 4 °C). As nodularity decreases, the eutectic recalescence tends to increase, as presented in **Figure 57** according to data from OCC GmbH [64].

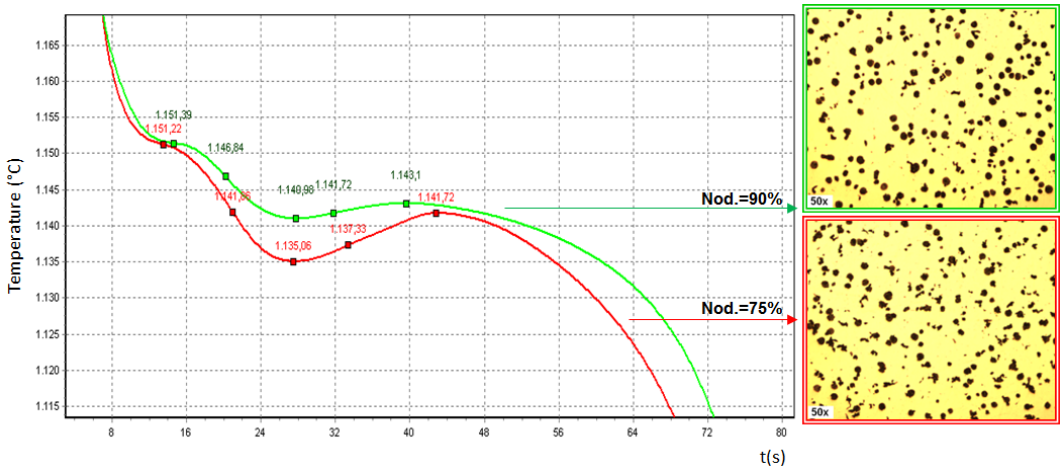

Figure 57 - Solidification curves for nodular cast iron with high and lower nodularity.

Nowadays, this principle is used in foundry practice to estimate accurately the graphite shape from a melt after solidification, during processing of that same melt. The implementation of such mathematical models is often used for the production of compacted and nodular cats iron melts [65] [66].

3.5.2.4. Prediction of shrinkage defects

Another aim for the use of thermal analysis techniques in cast iron production is the attempt to predict the occurrence of defects such as shrinkage and porosity. Based on the interpretation of the thermal analysis curve as well as the estimation of graphite shape and solidification morphology (hypoeutectic, eutectic or hypereutectic), some researches were done to study the relation between the graphite shape and the expansion during solidification [67].

Depending on the graphite shape and solidification morphology, the melt will have different sensibilities to form shrinkage, due to differences in the graphite expansion phenomenon during solidification. Studies performed by Hummer et. al. [68] using thermal analysis and displacement sensors, as well as works performed by Gedeonová et. al. [69] where also cooling curves and pressure curves from the melt in the mould wall were acquired, revealed that lamellar graphite cast iron has a higher expansion (higher displacement and pressure on the metal/mould interface) than nodular cast iron for the same eutectic saturation degree[11] (Sc). According to the study from Gedeonová, the pressure on the metal/mould interface for lamellar graphite cast iron with hypereutectic composition has a maximum of 243N (see **Figure 58c**) and for nodular graphite cast iron only 159N (see **Figure 58b**). The same study also indicate that hypoeutectic melt compositions of nodular graphite cast iron have higher pressure on the metal/mould interface and higher displacement than hypereutectic melt compositions (see **Figure 58a** and **b**). Schmidt et al. [70] have studied the influence of the eutectic saturation degree on the pressure over the mould wall, showing that for both lamellar graphite and nodular graphite cast iron the pressure increases

[11] Eutectic saturation degree (Sc) – Equivalent metallurgical meaning as the C.E. value. Calculated by the comparison of the actual melt's carbon content with the theoretical carbon content of a eutectic melt, accounting the influence of Si and P. Formula: $Sc = \%C_{total}/[4.30 - 0{,}3*(\%Si + \%P)]$ [68]. Sc=1, Eutectic; Sc<1, Hypoeutectic; Sc>1, Hypereutectic.

as the Sc increases from hypoeutectic (Sc<1) to eutectic (Sc=1) during the graphite growth in the eutectic transformation. The equivalent is to say that the pressure increases with the increase of the carbon content of the melt. In a cooling curve, the increase of the carbon content is represented by a decrease of the liquidus temperature, indicating therefore that as the liquidus temperature decreases, at least for hypoeutectic compositions, the expansion due to graphite growth in the eutectic transformation increases.

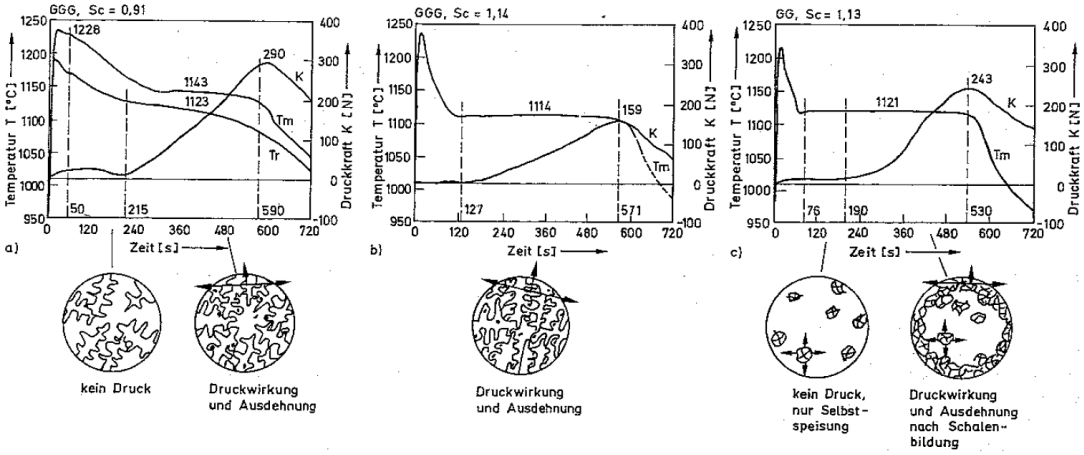

Figure 58 - Cooling curve and pressure curve as well as illustration of the solidification evolution of the microstructure for nodular graphite cast iron (a and b) and for lamellar graphite cast iron (c) [69].

The same work developed by Hummer, shows also that nodular cast iron solidification is characterized by an initial strong contraction and the expansion occurs later on, close to the end of solidification. The balance between the initial contraction and later expansion will influence the final shrinkage volume. For lamellar graphite cast irons, the expansion is constant throughout the eutectic transformation. Furthermore, Hummer also demonstrated that the increase of magnesium content increases the shrinkage in nodular graphite cast iron, once it increases the temperature difference between liquidus and low eutectic temperature from 0°K up to 17°K (the morphology of solidification changes from eutectic to hypoeutectic) on the thermal analysis curve and consequently the contraction at the beginning of solidification also increases from 0,185mm 0,309mm (see **Figure 59**).

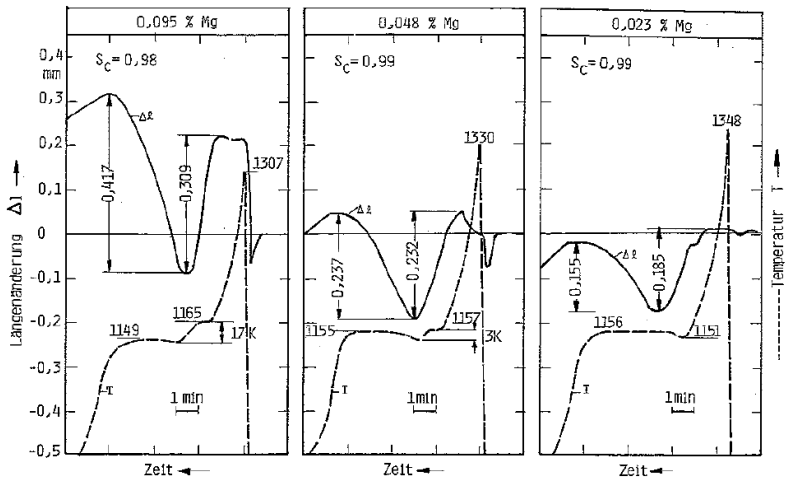

Figure 59 - Cooling curves and dilatation curves for nodular graphite cast iron, with increasing magnesium content [68].

Nevertheless, all this considerations on expansion due to graphite growth, is also dependent on the type of sand mould used in production of the casting. Schmitz et. al. [71] [72] showed in his studies on the behaviour of the sand form during pouring and solidification of a melt that the same iron poured in sand forms with different stability grades can result in the formation of massive shrinkage or no shrinkage at all, due to deformation of the mould walls [71].

Another method to acquire information on solidification characteristics of the melt that influence the shrinkage and porosity using thermal analysis is the determination of the dendritic coherency point. Such method is used often for aluminium alloys to predict the time of occurrence of the point when the feeding of the casting changes from mass feeding to interdendritic feeding [42].

No bibliography was found with the application of such techniques for cast iron alloys, and so no concrete evaluation of the transposition of this technics to cast iron alloys is possible at this moment.

There are three methods normally used to determine the dendritic coherency point. Bäckerud et. al. [73] proposed a thermal analysis method that uses two thermocouples, one positioned at the thermic centre and another close to the samples surface, where the dendritic coherency point corresponds to the first biggest minimum in the temperature difference curve (ΔT) between both cooling curves (see **Figure 60a**). The second method developed by Chai et. al. [74], is based on rheological technique, that uses a paddle stirrer to identify the dendritic coherency point due to

the changes in the mechanical strength (increase in torque) when the mushy zone is formed (see **Figure 60b**).

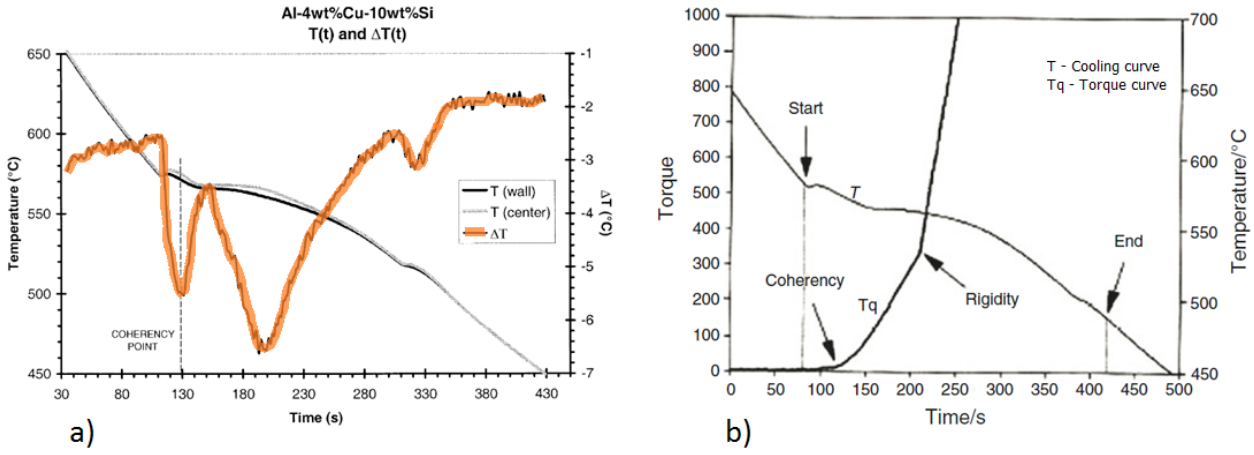

Figure 60 - Determination of the dendritic coherency point using thermal analysis following the models proposed by Bäckerud (a) and Chai (b).

Another method presented and tested by Djordjevic et.al. [43], uses the model proposed by Bäckerud, but a single thermal analysis curve acquired from the centre of the sample is required. Djordjevic indicated in his research that the one thermocouple technique can recognize the dendritic coherency point as good as the two thermocouple technic. He used the temperature difference curve from the two thermocouple method from Bäckerud to find a match in a single dT/dt versus temperature curve from a single thermocouple system, indicating that this curve reflects the thermal conductivity change during solidification and therefore can be used to determine the coherency point (see **Figure 61a**). The dendritic coherency point corresponds to a point in the dT/dt versus temperature curve "loop" before the curve enters in a quasi-constant cooling rate (see **Figure 61b**) [43]. Nevertheless, Djordjevic is not explicit in pointing out the exact criterion to locate the point, without the aid of Bäckerud's temperature difference curve for two thermocouples.

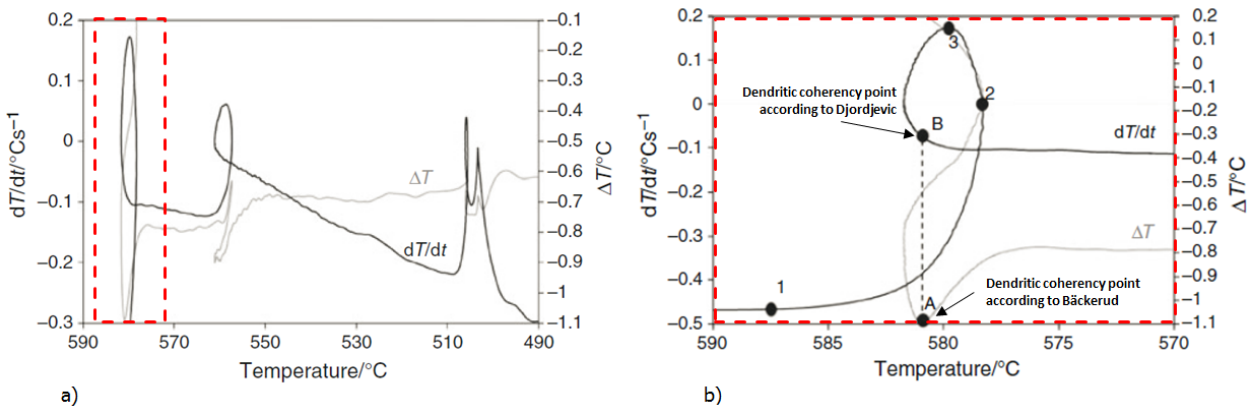

Figure 61 - Method of dendritic coherency point determination according to Djordjevic for Aluminium alloys. a) dT/dt curve versus temperature and ΔT versus temperature curve (following the method from Bäckerud); marked red is the region of primary dendritic nucleation and growth. b) Detail view of the region marked red in figure a, with indication of the dendritic coherency point.

The determination of the dendritic coherency point for cast iron, using thermal analysis would allow a better determination of the time available for liquid and mass feeding at a given region of the casting. This would therefore allow a more precise dimensioning of the feeding system and specially the feeder necks to freeze just before the occurrence of dendritic coherency.

4. Sample Materials and Methods of Analysis

For the execution of the present work, different sample types, sample preparation and measurement methods were used. They are hereby presented.

4.1. Thermal analysis equipment

In the execution of the work, thermal analysis evaluation of the melts was always performed in order to have a more complete assessment of the melts properties.

The equipment used was supplied by the company OCC GmbH and used the company's standard thermal analysis software PhaseLab. The software makes the acquisition and display of the cooling curve, 1st and 2nd derivative (the 1st derivative is presented as the inverse, therefore – dT/dt) and automatically performs the identification of the main plateaus and inflection points, as presented in **Figure 62**, according to the description and nomenclature given in **Table 7** and **Table 8**. The software saves all curves in a database, and allows the export of the saved data to Excel, for further data evaluation.

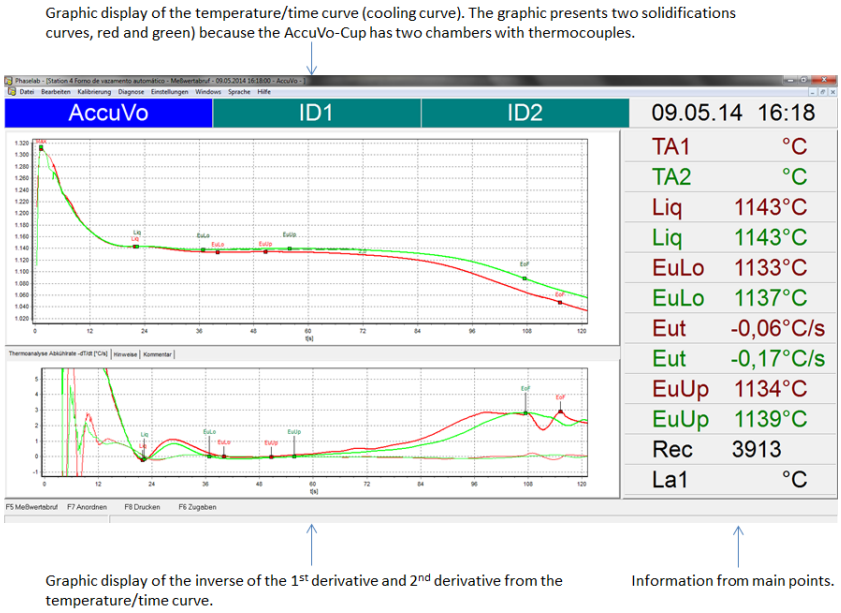

Figure 62 - Print-screen from the main window of the thermal analysis software PhaseLab.

The thermal analysis system uses 6B11 single-channel isolated signal-conditioning modules, from the company Analog Devices that can be configured for various thermocouple types, that allows a maximum sampling rate of 10Hz and a resolution of 16bits. Nevertheless, the company OCC uses in his system a measurement frequency rate of 3Hz, that is enough to obtain a temperature/time curve with sufficient resolution, that will afterwards be improved by a mathematical curve approximation function (smoothing), resulting in a final solidification curve accuracy that is above the accuracy of the thermocouple and his positioning. [57]

The thermal analysis system has a measurement accuracy of ±0,5°C. A scheme of the thermal analysis equipment is presented in **Figure 63**. Both measurement terminal, one for the base iron melt and another for the treated iron, where connected to the same electronic box and to the same computer.

The system was calibrated always before use. Type-K thermocouples (Chromel®[12]-Alumel®[13]) for the thermal analysis cups and contact cables were used.

For measurements made from the base iron melt, the thermal analysis cups QuiK-Cup QC4011 containing Tellurium from the company Heraeus Electro-Nite (see **Figure 63**) were used. The purpose of the use of Tellurium in the Quik-Cup is to promote the metastable solidification of the sample taken from the base iron melt, in order to allow the calculation of the C.E.[%], C[%] and Si[%] contents.

For measurements made from the melt after treatment, the thermal analysis cups AccuVo®-Cup from the company OCC GmbH were used (see **Figure 63**). The AccuVo® -Cup is a double-chamber closed cup, with a thermocouple at each chamber. This cup allows the addition of additives inside of the chambers, such as inoculant, for the evaluation of the melt's behaviour when mixed with that inoculant. The fact that the cup is closed ensures that the sample volume is always constant and this decreases eventual variations in the results due to variations of the mass of the sample solidifying and displacement of the thermocouple from the sample's thermal centre. A more detailed view of the interior design of the cup is given in **Figure 64**.

[12] Chromel® – Alloys made of approximately 90% Ni and 10% Cr.
[13] Alumel® - Alloys made of approximately 95% Ni, 2% Mn, 2%Si and 1%Al

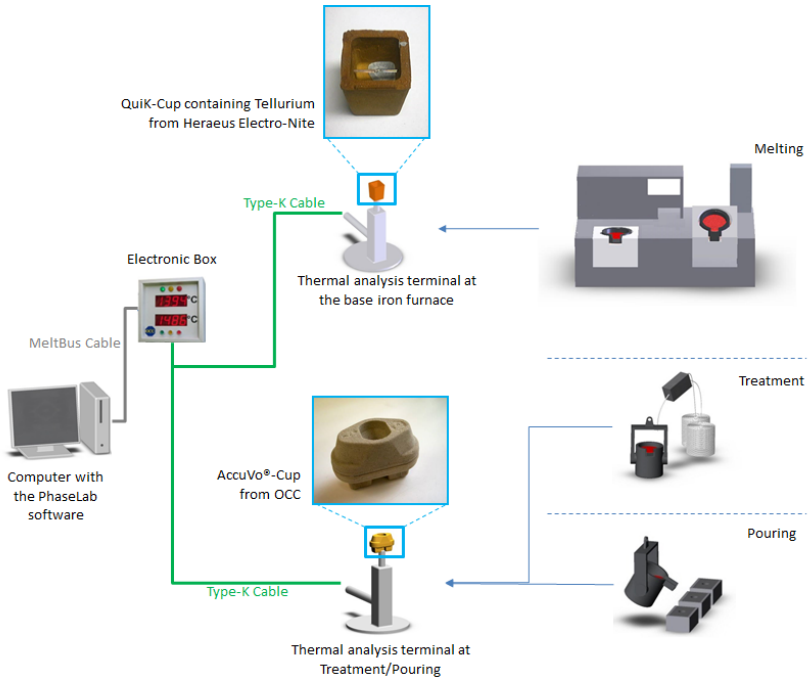

Figure 63 - Scheme of the layout and connection of the thermal analysis system used for the experiments.

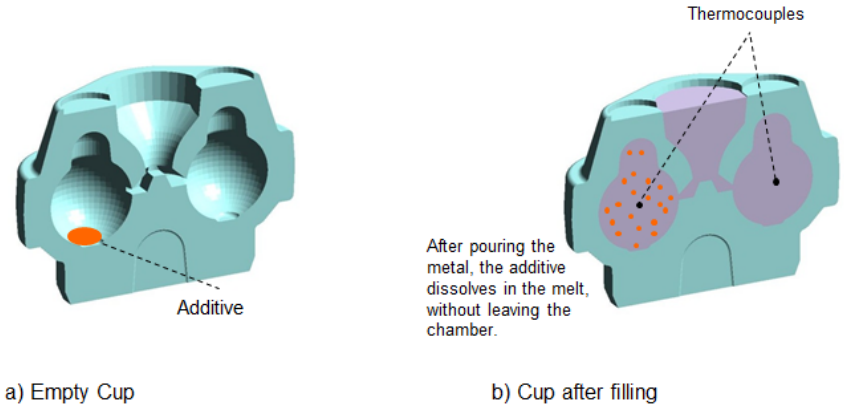

Figure 64 - Drawing of the AccuVo®-Cup, cut by the vertical middle plan, showing the two internal chambers. a) Empty cup with additive in one chamber; b) cup after pouring showing the positioning of the thermocouples in the sample.

4.2. Sample types

For the execution of the work, two types of samples where used for evaluation. The samples from the thermal analysis AccuVo®-Cup and a test casting developed for this work to study the occurrence of shrinkage and porosity defects in conditions similar to a real casting.

4.2.1. Shrinkage and porosity test casting

In order to study the occurrence of shrinkage and porosity defects, a versatile test casting was needed, that resembles also some of casting's characteristics such as connection between sections of difference thickness and strangulation points. Most of the test castings used in shrinkage and porosity studies are simply blocks, cylinders or crosses, and some of them do not allow the incorporation of a feeder (side or top) or the incorporation of small cores.

Therefore, for the present work, a test casting was developed that aims to be versatile and applicable to study shrinkage and porosity in different experimental conditions, also out of the scope of this work. The design of the developed test casting is presented in **Figure 65**. Additional information on the test casting is also presented in the **Table 9**.

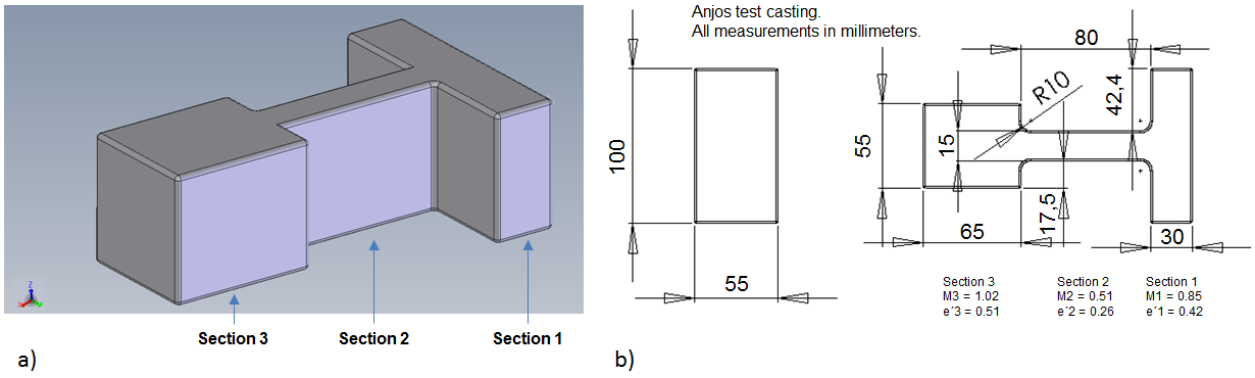

Figure 65 - Anjos test casting; a) 3D drawing showing the test casting design as identification of the different sections; b) technical drawing showing the measurements of the test casting part to create a model. Drawings made using SolidWorks software.

Table 9 - Main information on the test casting used to study the formation of shrinkage and porosity defects.

	Section 1	Section 2	Section3	Total
Volume [mm^3]	196.625	66.000	165.000	427.625
Weight [Kg]	1,44	0,48	1,20	3,12
Module	1,02	0,51	0,85	

The test casting is composed by a T-shape junction between section 1 and 2 that are usually a design that causes the formation of shrinkage or porosity. Section 2 is characterized by a long and narrow plate, with a smaller module than section 1 and 3 that will result in shorter solidification time, isolating section 1 from section 3 while they are still not completely solid. Section 3 is a versatile section in this test casting. Its big module and cubic shape are prone to the formation of shrinkage. Furthermore, section 3, allows the easy assembly of feeders (side or top), mounting of a expansion or linear movement sensor on one of the sides of the cube to study the expansion of graphite during solidification, the mounting of thermocouples and even the mounting of cores to study their impact on the formation of shrinkage and porosity defects. The fact that the all section have parallel walls, was made with the purpose to create two opposite solidification fronts, that will difficult the flow of liquid during solidification, especially along section 2.

The feeding of the test casting is possible to be made from section 1 (in-gate close to a T-junction) or section 3 (in-gate at a massive volume). The dimensioning of the different section was made with the purpose to create shrinkage and porosity defects. The result from the simulation of the model, done with the nodular graphite cast iron solidification model from the software Flow3D, is presented in **Figure 66**. The result from the simulation show the strong formation of shrinkage defects on the T-junction between section 1 and 2 and a massive shrinkage in section 3.

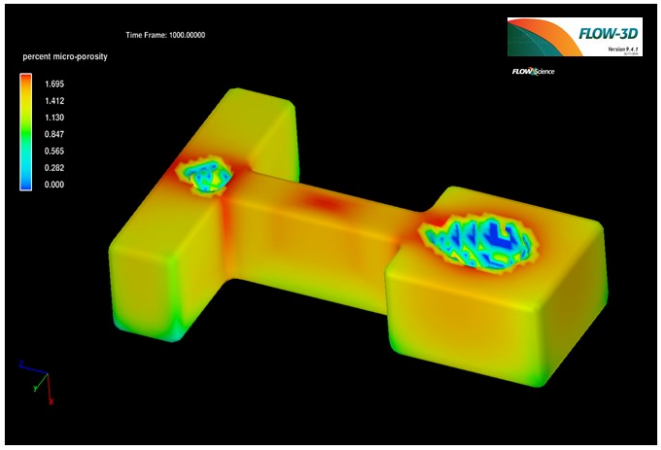

Figure 66 - Results from the simulation of the Anjos test casting using the software Flow3D. Image show a horizontal cut by the midline of the test casting revealing the shrinkage defects in section 1 and 3.

4.2.2. Microstructure sample

For the microstructure evaluation, both the test casting and the thermal analysis samples were used for microstructure evaluation (not necessarily simultaneously).

The samples from the thermal analysis cup were identified after sampling was made, by a reference number as well as the indication of the additive at each chamber. The observation of the microstructures from these samples allows a direct correlation between the microstructure characteristics or properties with the respective thermal analysis curve.

After pouring, the thermal analysis sample has the shape presented in **Figure 67a**. After cleaning the sand from the sample's surface, the two spheres of the same cup where separated from the in-gate system (cut 1) and cut by theirs horizontal midline across the thermic centre (cut 2), as presented in **Figure 67b**. The upper part of each sphere was used for the metallographic evaluation in the surface that resulted from the cut 2.

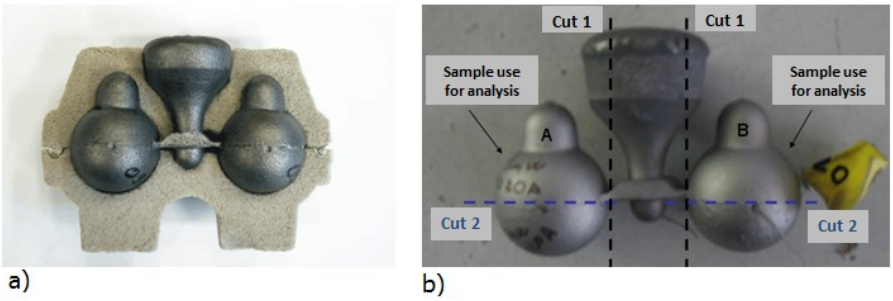

Figure 67 - Images from the AccuVo-Cup sample. a) image from the sample in the sand form; b) scheme showing how sample was cut for later metallographic evaluation.

The evaluation of the microstructure samples from the test casting allows a direct observation of the microstructure in areas close to the occurrence of the shrinkage and porosity defects, allowing a better understanding about the eventual relation between them. To obtain the metallographic samples from the test castings, they were cut across their vertical midline passing though the thermal centre of the casting, as illustrated in **Figure 68a**. From each test casting, three metallographic samples could be extracted from each of the main sections and identified as represented in **Figure 68b**.

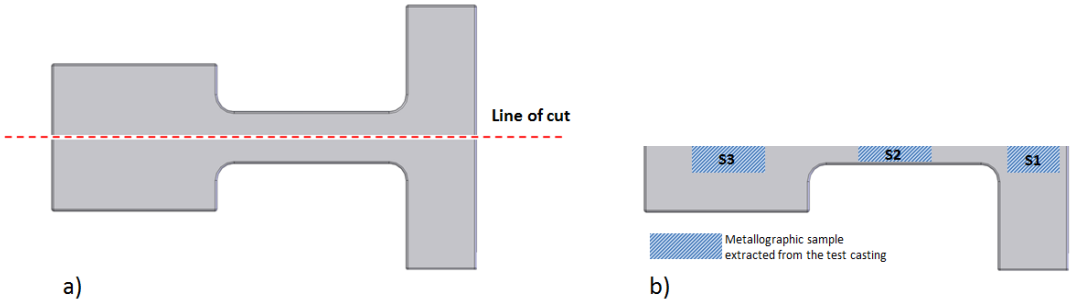

Figure 68 - Illustration of the test casting showing: a) top view of the test casting showing the cut line; b) the location of the metallographic samples extracted. The surface used for metallographic evaluation is the one that resulted from the cut line indicated in figure a.

4.3. Sample evaluation methods

4.3.1. Standard metallographic preparation

The samples subjected to metallographic evaluation, followed the preparation method presented in **Table 10**. The grinding and polishing operations were performed using a Abramin machine with a sample holder of 6 samples from the company Struers.

Table 10 - Procedure for metallographic preparation of samples.

Preparation step	Description	Preparation time (min.)
Grinding	120 mesh grinding diamante surface disc from Cloeren Technology GmbH	1
	200 mesh grinding diamante surface disc from Cloeren Technology GmbH	1
	600 mesh grinding diamante surface disc from Cloeren Technology GmbH	1
	800 mesh wet grinding paper from Struers	2
Cleaning between grinding	Washed water stream and dryed with soft paper	
Polishing	Fine polishing using DiaProPlus 3µm diamond suspension from Struers	9
Cleaning after polishing	Surface cleaned with Ethanol and dried with hot air.	

For observation of the graphite structure of the samples, the evaluation of the samples was done directly after polishing and cleaning.

For evaluation of the presence of iron carbides (Fe_3C), ferrite and pearlite content, the sample was etched using Nital 2% (98% Ethanol and 2% nitric acid) and the etching time varied between 3 and 5 seconds.

The microstructure observation of the samples was performed at a Nikon OptiPhot microscope, using 5x, 10x, 20x or 50x magnification. The micrographs presented and used in further analysis were obtained using a 3 megapixel digital camera UI1460SE from the company IDS GmbH, with connected to via USB 2.0 to a computer.

4.3.2. Metallographic evaluation of graphite particles by automatic image analysis system

The metallographic evaluation of the samples was performed using the image analysis software Micr-O-Phase from the company OCC GmbH. The software makes the acquisition of the images via a USB connection directly from the UI1460SE digital camera mounted in the microscope. Once the images are acquired by the software, the operator adjusts the threshold level for the image evaluation and the software analyses afterwards all metallographic parameters such as nodularity, particle density, phase area of graphite, graphite particle size class distribution, graphite shape classification, all according to the norm EN-ISO 945-1 2010.

The determination of the area of a graphite particle is made by the Micr-O-Phase software as the sum of all pixel areas that form a particle in the micrograph. The pixel size of the image is a function of the camera's pixel resolution and magnification used when the micrograph was taken. This information is added to the Micr-O-Phase, together with a micrograph of a millimetre scale with sub-division every 10µm. From this micrograph, the software counts the number of pixels that are along a 200µm linear distance across the scale. By dividing the number of counted pixels by the length of 200µm, the pixel size in the micrograph is known, and all measurement, linear or area, can be performed from micrographs taken with the same camera and same magnification.

The evaluation of the graphite particle shape is made by the Micr-O-Phase software, based on the evaluation of the roundness of each graphite particle according to the following **Equation 7**;

$$Roundnes = \frac{A_{Measured}}{A_{(\emptyset_{Ferret})}} = \frac{A_{Measured}}{\frac{\pi \emptyset_{Ferret}^2}{4}} = \frac{4 \times A_{Measured}}{\pi \emptyset_{Ferret}^2} \text{ (Eq. 7)}$$

where, $A_{Measured}$ is the area of the graphite particle, $A(\emptyset_{Ferret})$ is the area of a circle with a diameter equivalent to the graphite particle's Ferret diameter and $\emptyset_{Ferret}$ corresponds to the graphite particle's Ferret diameter. The roundness represents the comparison, or ratio between areas, of the real graphite particle area and the theoretic area of a circle with a diameter equal to the particle's ferret diameter. Roundness was proved to be a better variable to distinguish and classify the graphite shape, compared to other variables such as sphericity or aspect ratio [75].

The graphite shape classification, followed the evaluation of the roundness of each graphite particle to classify them according to the classification suggested by the norm EN-ISO 945-1 2010. The classification criterion used at the software Micr-O-Phase to classify the graphite particles according to their shape is presented in **Table 11**, used at micrographs taken with a 100x magnification.

Table 11 - Graphite shape classification based on roudness, used at the software Micr-O-Phase image analysis software, for micrographs taken with a 100x magnification.

Graphite form class	Roundness
Form I	<0,1
Form II	Not considered.
Form III	0,1 to <0,4
Form IV	Not considered
Form V	0,4 to <0,70
Form VI	≥0,70

The graphite shapes Form II and Form IV are not considered in the classification because Form II is a graphite shape that is observed only in hypereutectic lamellar graphite cast iron and Form IV only in malleable irons.

An important parameter used in the assessment of the graphite shape quality in nodular graphite cast iron is the determination of the microstructures nodularity.

The nodularity is determined based on the global evaluation of the graphite particles shape in the microstructure. Nodularity can range from 0%, indicating that the microstructure has no graphite

with round shape (typical of lamellar graphite cast iron), to 100% meaning that the microstructure has only perfectly round graphite particles. Following the norm DIN EN 1563:2012-03 for nodular graphite cast iron, nodularity should be 80% or above to ensure, with safety, that the required mechanical properties are reached, assuming that the matrix (percentage of ferrite and pearlite) is achieved and that no undesirable carbides and inclusions are also present. The calculation of the nodularity, used in the software Micr-O-Phase, is presented in the **Equation 8**.

$$\boldsymbol{Nodularity}[\%] = \mathbf{0,5} \times \boldsymbol{FormV}[\%] + \boldsymbol{FormVI}[\%] \quad \textbf{(Eq. 8)}$$

The *graphite size distribution* classification, used by the software Micr-O-Phase, followed also the classification proposed by the norm EN-ISO 945-1 2010, presented in **Table 12**.

Table 12 - Size class distribution for the graphite particles, used in the Micr-O-Phase image analysis software.

Size class	Size (in millimeters)
1	≥1
2	0,5 to <1
3	0,25 to <0,5
4	0,12 to <0,25
5	0,06 to <0,12
6	0,03 to <0,06
7	0,015 to <0,03
8	<0,015

The particle density is a variable from the micrographs analysis that expresses the number of graphite particles per square millimetre, as presented in the **Equation 9**.

$$\boldsymbol{Particle\ Density}[1/mm^2] = \frac{\boldsymbol{Total\ number\ of\ graphite\ particles}}{\boldsymbol{Area\ analised}} \quad \textbf{(Eq. 9)}$$

In a cast iron microstructure, often can be found the presence of small inclusions (smaller than the graphite nodules) that are not graphite particles and therefore should not be considered in the analysis of the graphite particle shape, size or density. The Micr-O-Phase allows a definition of a threshold level for particle area bellow which is considered to be an inclusion (called in the software as *"cut-off area"*) and is therefore excluded from the software's graphite evaluation. A standard cut-off area of 70mm^2 was defined, based on the observation of the microstructures prior to analysis.

4.3.3. Colour metallography technic for evaluation of austenitic structure

Colour metallography is an etching technic that allows a better distinction of different characteristics of the microstructure, when compared to traditional black/white technics such as the use of Nital, and is more sensitive to differences in.

With the aim of revealing the austenitic structure of solidification on nodular cast iron samples, a hot alkaline etching was used. This etching method produced a thin interference film on the surface of the alloy that will change in thickness or density in dependence to a given property of the sample's microstructure. The differences in the film thickness and density will originate a difference deflection of the microscope's light, resulting in an image with different colours.

In this case, the alkaline solution will react with the Si at the sample's surface forming a colloid that is absorbed and deposited onto the surface of the sample forming a thin film. For regions of the sample rich in Si, the film will form faster and will be thicker. On the other case, regions of the sample's surface poor in Si will have a thinner film that grows slower. Therefore, the resulting image will be composed by different colours that relate to the different Si content across the sample's surface. As indicated in the **Table 3**, Si is the element with the highest segregation coefficient in austenite during solidification, and therefore colour etching can show important information on the austenite structure.

Based on this assumption, Zhou [76] presented a colour scale based on the application of hot alkaline etching that reveals the silicon content, solidification sequence and effect of etching time, presented in **Table 13**.

Table 13 - Colour scale for colour etched samples with hot alkaline solution, as a function of Si content, solidification time and etching time [76].

Number	Colour	Silicon content	Time to solidify	Etching time
1	Yellow	high	early	long
2	Blue green	↑	↓	↑
3	Purple	↑	↓	↑
4	Orange red	↑	↓	↑
5	Pale yellow	↑	↓	↑
6	Pale blue	↑	↓	↑
7	Blue	↑	↓	↑
8	Brown	↑	↓	↑
9	Cream white or pale yellow	low	late	short

Once hot alkaline etching reacts with Si present in the sample's microstructure, the content of Si in the sample and its segregation levels will affect the etching conditions. Therefore, different compositions and etching procedures are available and should be selected according to the characteristics of the samples. These different etching compositions are presented in **Table 14**.

Table 14 - Formula of the different available hot alkaline etching reagents and etching procedure [76].

Etching reagent No.	Formula				Etching process		Literature
	NaOH (g)	KOH (g)	Picronitric acid (g)	Distilled water (mL)	Temperature (°C)	Time (min)	
1	28	1	4	200	95–100	10 –30	[28, 29]
2	100		8	200	95 –100	1.5 –4	[31, 32]
3	20	3	4	200	65	10– 65	[28]
4	40	160	40	200	120	1–1.5	[37]
5	28	56	28	200	95– 100	1.5–3	[38]

The etching reagent no.1 was, in this work, always the standard reagent to be used first at any new sample from a new melt. Only in cases where the reagent did not give the optimal results, other reagent was experimented until one of them provides the desirable results. The etching number used for a given sample, as well as the etching temperature and time, will be indicated always when a sample's microstructure that was colour etched is presented.

The experimental apparatus for the performance of the colour etching is presented in **Figure 69**. The etching preparation procedure was made firstly by pouring distilled water into a 400ml glass beaker. The beaker was then placed on a magnetic stirrer (B in **Figure 69**) and a stir bar was immersed in the distilled water. In an electronic weighing scale (A in **Figure 69**), the needed amount of NaOH was weights, added to the distilled water and the stirrer was started. Afterwards, the KOH was also weighted and added into the beaker, followed by the Picronitric acid. After one minute of stirring of all the added elements, the stirrer was stopped, the stir bar removed and the beaker transferred to an electrical hot plate (C in **Figure 69**). A thermometer was inserted in the solution to measure the temperature (D in **Figure 69**). Once the solution reached the desired temperature, the sample was immersed in the solution with the polished surface facing up, to avoid scratching. The temperature was carefully controlled during the etching time to be kept in a range of ±5°C from the target temperature. Once the etching time was reached, the sample was extracted, washed initially with distilled water and afterwards with ethanol. At last, the sample was dried with hot air and taken to the microscope for observation. If the sample was considered

to be well etched, the sample evaluation was done. If the sample was under-etched, the etching procedure was repeated, for shorter time periods until the structure was considered to be properly etched. If the sample was over-etched, it was taken again to the final polishing step to remove the etched layers and the etching procedure repeated.

The etching solution, when kept at high temperature during long periods of time, started to lose water, which caused its chemical concentration to change. Therefore the usage time of one solution was limited to approximately 90 minutes (for a holding temperature of 100°C). After that time a new solution had to be prepared.

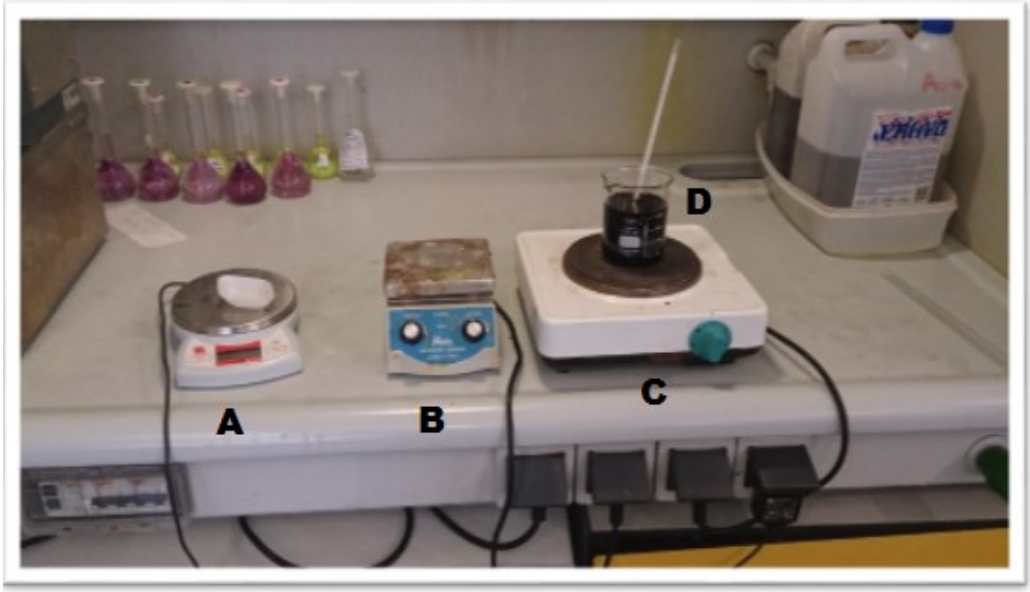

Figure 69 - Laboratory apparatus for the performance of the colour etching technic. A) Electronic weighting scale; B) Magnetic Stirrer plate; C) Electrical hot plate and beaker containing the hot alkaline solution and thermometer.

4.3.4. Shrinkage and porosity evaluation

4.3.4.1. Shrinkage and porosity defect nomenclature

In the present work, the nomenclature to be used in the classification of the shrinkage and porosity defects will be based on the proposal from Stefanescu presented previously in **Figure 48**. Nevertheless, some changes in nomenclature where made, in order to consider defects that are not properly defined, such as small intercellular pores (as big or slightly bigger than a graphite

nodule and only observed under the microscope) that appear in the LTF zones, or the incorrect use of the prefix "micro" in classification of defects that are readily observed without the aid of a microscope.

The prefix "micro" will be used in the classification of defects that can only be observed with the aid of a microscope.

The nomenclature used in the defect classification in the present work is presented in **Table 15**.

Table 15 - Nomenclature, used in the present work, to classify shrinkage porosity defects.

Nomenclature	Description	Example
Open Shrinkage	Shrinkage cavity with contact to the casting's surface, either on the top surface or the side surface	
Shrinkage	Single or multiple individual closed shrinkage volume defect with diameter (of Ferret diameter) ≥3 mm	
Porosity	Defect region characterized by dispersion of several small volume voids interconnected between each other or not, along an area with diameter (of Ferret diameter) < 3mm and visible without aid of a microscope. No contact with the casting's surface.	
Microporosity	Small individual closed volume void, with diameter (of Ferret diameter) < 1mm, better observed under a microscope, including volume voids in the intercellular/interdendritic zones.	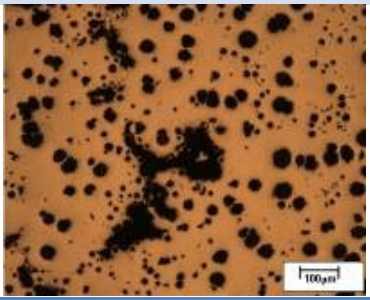

4.3.4.2. Sample preparation

For evaluation of the shrinkage and porosity defects in the test casting, the castings were cut across the vertical mid-plane, through the thermic centre of all sections (see **Figure 70b**). To do so, a horizontal semi-automatic band saw (see **Figure 70a**) was used to cut the castings.

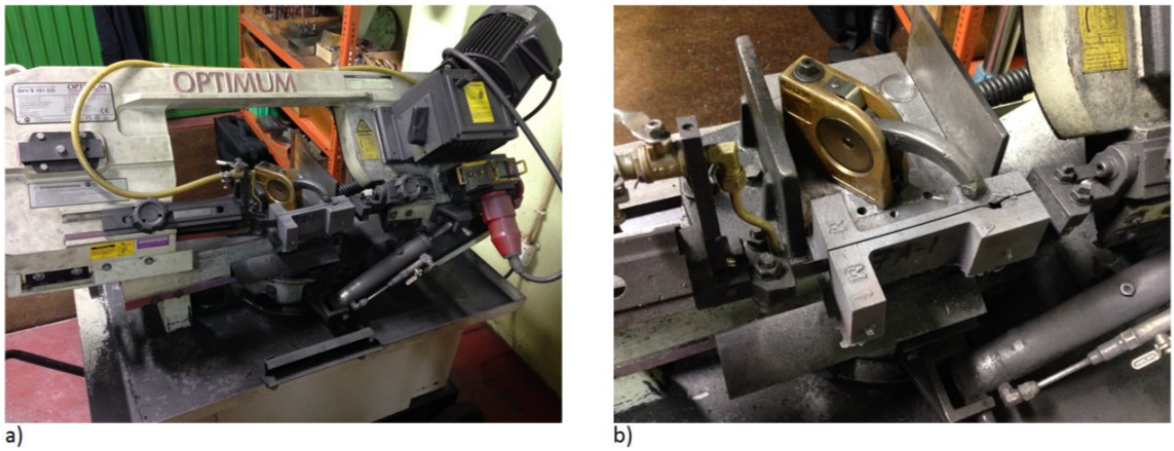

Figure 70 - Apparatus for the cut of the test casting. a) Test casting being cut in the horizontal semi-automatic band saw; b) Details showing the casting cut position.

For the evaluation of the test casting's volume defects, the surface that resulted from the cut revealing the thermic centre of the sample was evaluated in the search of any defect related to melt shrinkage or porosity. The occurrence of the defects was always allocated to the section in the test casting where it occurred.

4.3.4.3. Shrinkage area and shrinkage volume

For the evaluation of the shrinkage defects, the defect volume and the approximated area at the surface that resulted from the cut was evaluated. The *Shrinkage Volume* was measured using a low viscosity and low surface tension liquid, in this case ethanol, that was injected in the shrinkage cavity using a syringe (with a millilitre scale) until the shrinkage cavity was full with liquid, as presented in **Figure 71**. The volume of ethanol injected was measured at the syringe scale to determine to the volume of shrinkage on that half of the test casting. This was performed

to both half of the same sample and at the end the volumes were added to obtain the total *Shrinkage Volume* defect by section of the test casting.

In cases where the same section exhibits more than one shrinkage defect, the number of occurrences and the volume of each individual shrinkage defect were registered, as well as the sum of all shrinkage volumes by section. In cases of occurrence of open shrinkage, in order to allow the measurement of the cavity volume, the shrinkage was closed using modelling clay at the external surface of the casting.

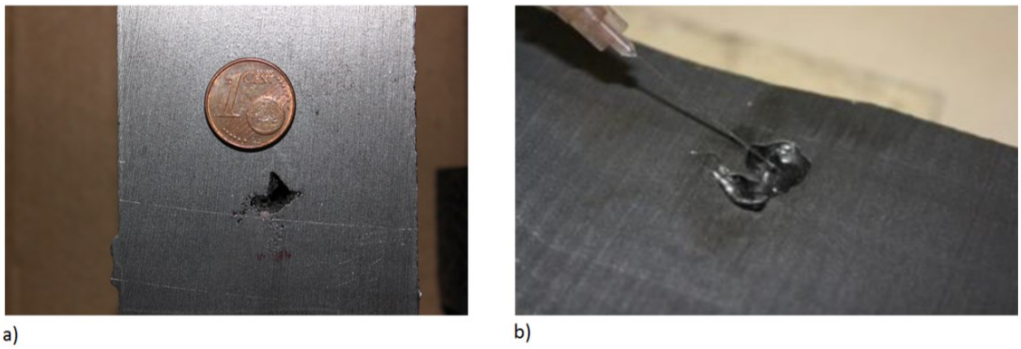

Figure 71 - Example of a shrinkage defect in the test casting. a) Detail of the shrinkage volume after cut of the casting; b) Filling of the shrinkage volume defect with ethanol using a syringe.

The measurement of the *Shrinkage Area* defect was also made by approximation through the fitting of a regular geometric rectangle shape to the defect. Afterwards, the sides of the rectangle were measured and the area of that rectangle calculated to obtain the approximate *Shrinkage Area* of that defect (see **Figure 72**). This *Shrinkage Area* defect was measured in both half of the test casting and the average value was calculated.

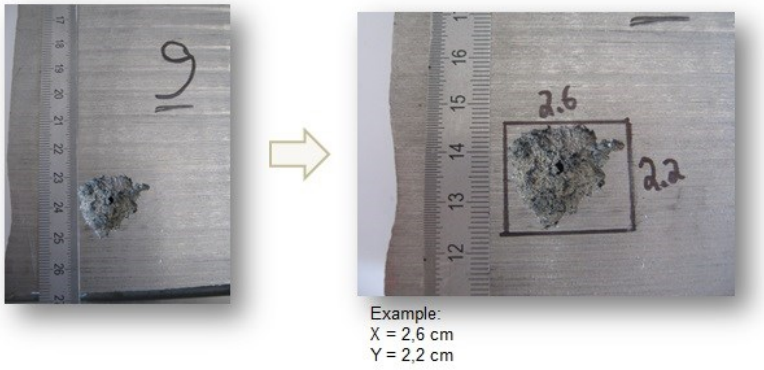

Figure 72 - Example of the method to measure the shrinkage area.

4.3.4.4. Porosity area and porosity index

For the evaluation of the porosity defects, due to their characteristics and the fact that they are often composed by a dispersion of small volume defects, as presented before in the **Table 15**, no volume was measured due to technical difficulties in filling accurately all small volume voids. Therefore, only the area of porosity dispersion (*Porosity Area*) and a *Porosity Index* were measured. The measurement of the *Porosity Area* was performed in an identical way to the *Shrinkage Area* as presented in **Figure 72**, but now applied to the region containing porosity. However, in the occurrence of porosity defects, the small volume voids can have sometimes a slightly bigger or smaller size for the same area of porosity dispersion. Therefore, an intensity index scale was used resulting from a visual qualitative evaluation of the individual void size, to use it together with the area of porosity evaluation. The porosity intensity scale is presented in **Figure 73**. To calculate the *Porosity Index*, and express both the porosity dispersion and the small individual void size, the **Equation 10** was used.

Figure 73 - Porosity's intensity scale used for the calculation of the Porosity Index.

$$Porosity\ Index = Porosity\ Area(mm^2) \times Porosity\ Intensity\ Index \quad \text{(Eq. 10)}$$

4.3.4.5. Contraction defect index

In addition to all shrinkage and porosity evaluation methods and variables, another variable was defined named "*Contraction Defect Index"* that represents the general melt contraction defects magnitude, regardless of the defect type and classification, as long as it resulted from melt contraction. This allows a global evaluation of the results and correlation to the process parameters including shrinkage and porosity defects together. This *Contraction Defect Index* is calculated using the same method described for the *Porosity Index*, but including also the open shrinkage and shrinkage defects. The intensity scale from **Figure 73** is used, but includes now two additional intensity levels for shrinkage and open shrinkage, as presented in **Figure 74**.

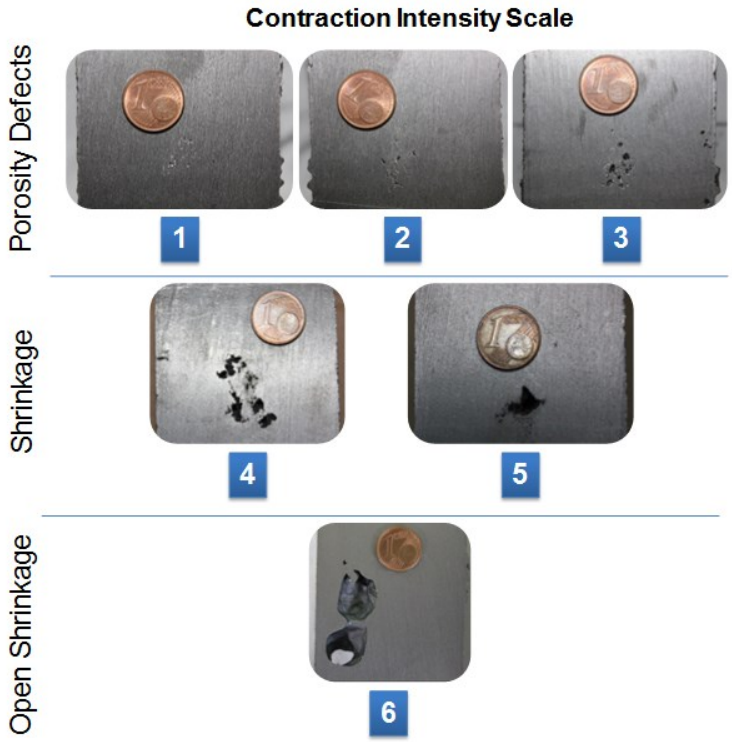

Figure 74 - Contraction intensity scale for shrinkage and porosity defects.

The formula for the calculation of the *Contraction Defect Index* is presented in **Equation 11**.

$$\boldsymbol{Contraction\ Defect\ Index = Defect\ Area(mm^2) \times Defect\ Intensity\ Index} \quad \textbf{(Eq. 11)}$$

5. Experimental Procedure and Results

5.1. Study of the microstructure evolution during solidification using thermal analysis

One of the main purposes on the application of thermal analysis techniques is to get information of the solidification sequence and characteristics of the microstructure during solidification. Information such as which phase is solidifying first, when does the graphite nodules start to grow, the melt solidification morphology (hypoeutectic or eutectic or hypereutectic), is important during the production process in order to evaluate if the melt is complying with the requirements, before it is taken for pouring. Therefore, it is important to effectively know in details the solidification curve and associate the shape, the plateaus and inflections to the metallographic phenomenon occurring.

To perform that study, it is necessary to observe the microstructure from a thermal analysis sample before, after or while a given transformation is occurring. In the present work, it was intended to observe what phases are present immediately after the liquidus temperature, before the eutectic low temperature and during the eutectic.

For this observation, it was necessary to interrupt the solidification of the sample in the thermal analysis cup once a plateaus or inflection on the solidification curve was reached. The interruption of the solidification was done by immersion of the sample in solution of brine (water with sodium chloride) and ice. This rapid solidification of the sample will cause the following transformation of the different phase constituents in the sample:

- Liquid metal -> Cementite (Fe_3C)
- Austenite -> Martensite or Pearlite
- Graphite -> Graphite

Therefore, through the observation of the constituents of the sample after rapid cooling it is possible to see what phases have already precipitated (austenite and graphite) at that stage of solidification and what was still liquid.

For the execution of this experiment, a thermal analysis system was used with two stations for sampling after treatment of the melt, using the thermal analysis AccuVo® cup. From the same sampling spoon a sample was taken from the melt after treatment and the two AccuVo® cups were filled.

In one cup the thermal analysis preceded normally until the end of solidification and the other was used to be immersed in the brine water with ice for interruption of the solidification, as demonstrated in **Figure 75**. In order to accelerate the cooling of the sample inside the cup, a few seconds after pouring the sample, one side of the cup was cracked and removed using a plier to expose the sample's surface (see **Figure 75a**). The acquisition of the cooling curve of the sample quenched continued after the sample was immersed until the end of solidification, once the thermal analysis cup was still connected to the measurement terminal. Both cups were then taken to the laboratory for metallographic evaluation.

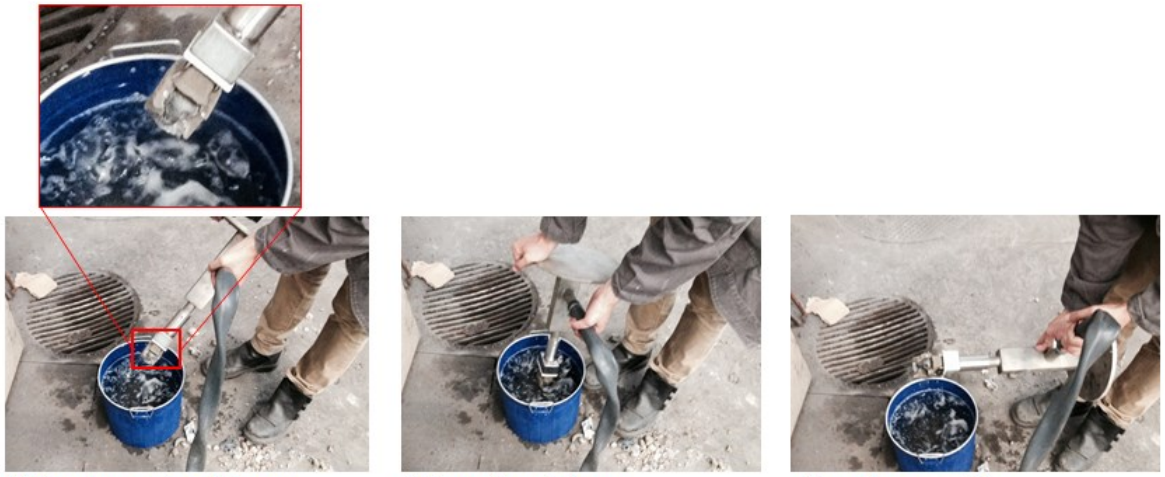

Figure 75 - Steps performed for the quenching of the thermal analysis sample AccuVo®-cup.

A total of 3 different base iron charges for the grade GJS400 were used for these trials, performed in a foundry under real production conditions, following the trials procedure illustrated in **Figure 76**. From the base melt with hypoeutectic solidification morphology, two treated ladles were used, from a base melt with eutectic solidification morphology only one treated ladle was tested and from a hypereutectic solidification morphology base melt two treated ladles were used.

The treatment was performed using the Sandwich method and the alloys used are presented in the **Table 16**.

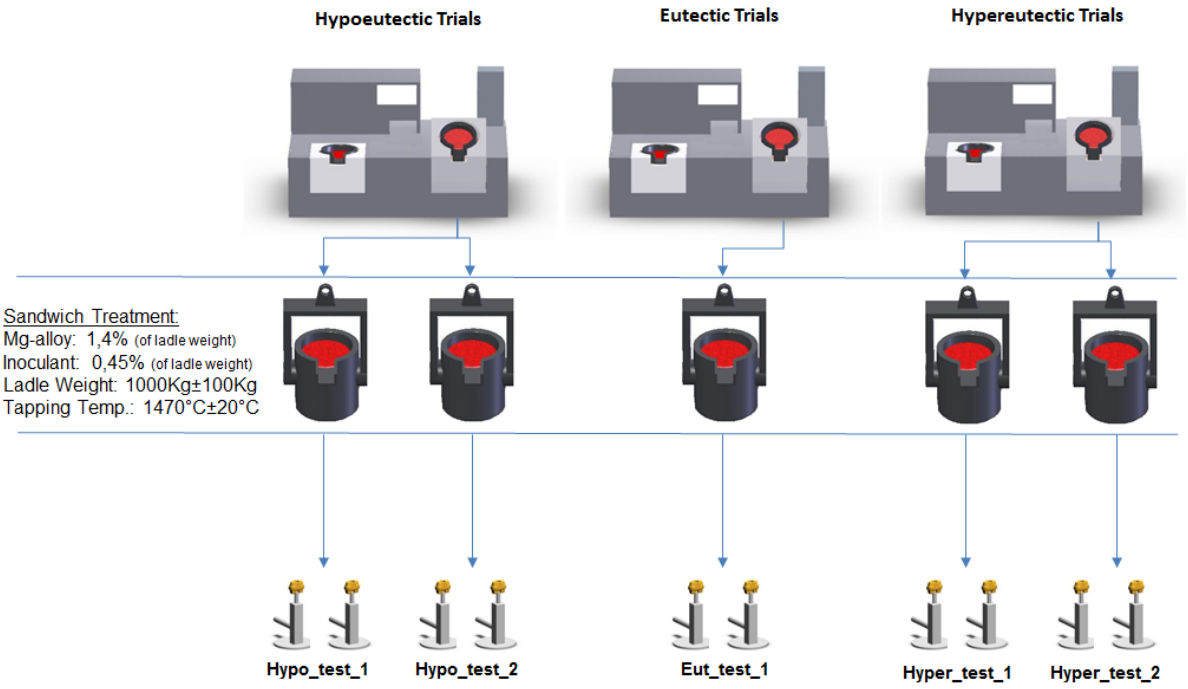

Figure 76 - Illustration of the trials procedure for the quenching of the thermal analysis sample.

Table 16 - Treatment wires composition used in the thermal analysis quenching trials.

	Si (wt%)	Ca (wt%)	Mg (wt%)	Ba (wt%)	Al (wt%)	RE (wt%)	Zr (wt%)	Mn (wt%)	Fe (wt%)
Nodularizer	44,6	1,19	6,2	-	0,64	0,64	-	-	balance
Inoculant	66,9	1,81	-	1,69	1,06	-	2,45	2,74	balance

From each treated ladle, a sample for chemical analysis was taken, and the results are presented in **Table 17**.

Table 17 - Chemical analysis from the melt after treatment, used in the quenching test.

Melt type	Test	C.E.[%]	C[%] (LECO)	Si[%]	Mn[%]	P[%]	S [%]	Cu[%]	Sn[%]	Mg[%]
Hypoeutectic	Test_1	4,38	3,51	2,62	0,43	0,009	0,004	0,031	0,012	0,046
	Test_2	4,35	3,48	2,60	0,42	0,009	0,004	0,033	0,014	0,049
Eutectic	Test_1	4,47	3,57	2,70	0,44	0,011	0,003	0,024	0,012	0,050
Hypereutectic	Test_1	4,59	3,64	2,85	0,45	0,01	0,004	0,025	0,011	0,044
	Test_2	4,57	3,61	2,89	0,45	0,01	0,005	0,026	0,015	0,042

The representative curves, for the normal solidification, of the melts tested are presented in **Figure 77**. The red curve is from the hypoeutectic melt, the blue one from the eutectic melt and the green from the hypereutectic melt.

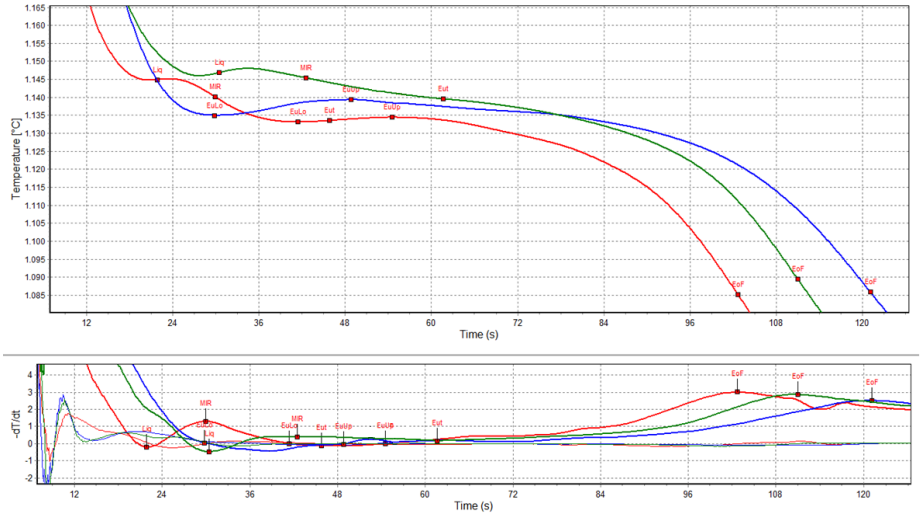

Figure 77 - Solidification curves from the 3 melt types used for the quenching test. red: hypoeutectic; blue: eutectic; green: hypereutectic.

The hypoeutectic curve, obtained for the ladle melts Hypo_Test_1 and Hypo_Test_2 show two main plateaus in the curve. A primary one, without any recalescence, considered to be the liquidus temperature and a second one, bigger than the first, with 2°C of recalescence, considered to be the eutectic transformation, as indicated in **Figure 78**.

The eutectic curve is characterized by only one plateau of big dimension, with a recalescence of 5°C a long duration, considered to the eutectic transformation, also presented in **Figure 78**.

The hypereutectic curve is characterized again by two plateaus, like in the case of the hypoeutectic, but with the particularity of the recalescence being inverted. This means that the first plateaus has now a recalescence of 3°C, estimated to be the liquidus temperature related to the solidification of primary graphite and a slight second plateaus considered to be associated to the eutectic transformation.

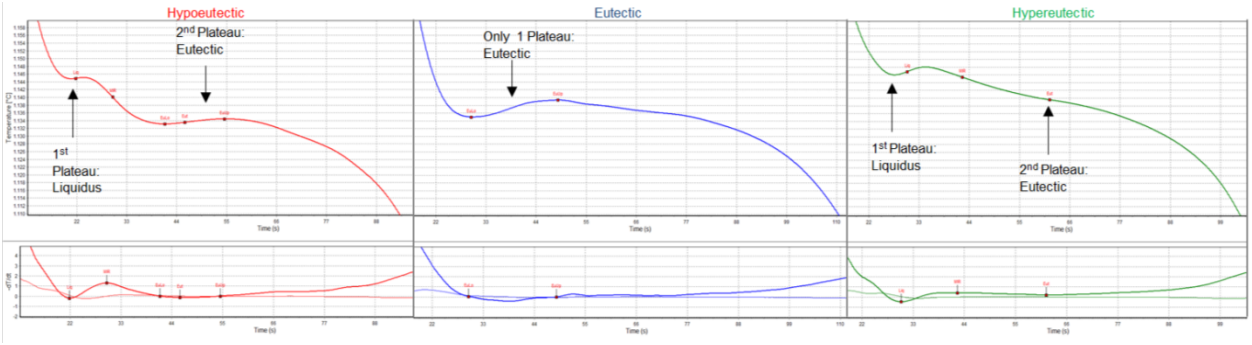

Figure 78 – Same curves as in Figure 77, showing the comparison of the plateaus between the solidification curves obtained on the trails.

5.1.1. Microstructure evolution of hypoeutectic melts during solidification using thermal analysis

The solidification curves from the two quenching tests of the melt with hypoeutectic solidification morphology, according to thermal analysis, are presented in **Figure 79**. In the first test (Hypo_Test_1) presented in **Figure 79a**, the quenching was done after the plateau corresponding to the liquidus temperature, before the MIR point. On the second test (Hypo_Test_2) the quenching was performed immediately before the low eutectic point, presented in **Figure 79b**.

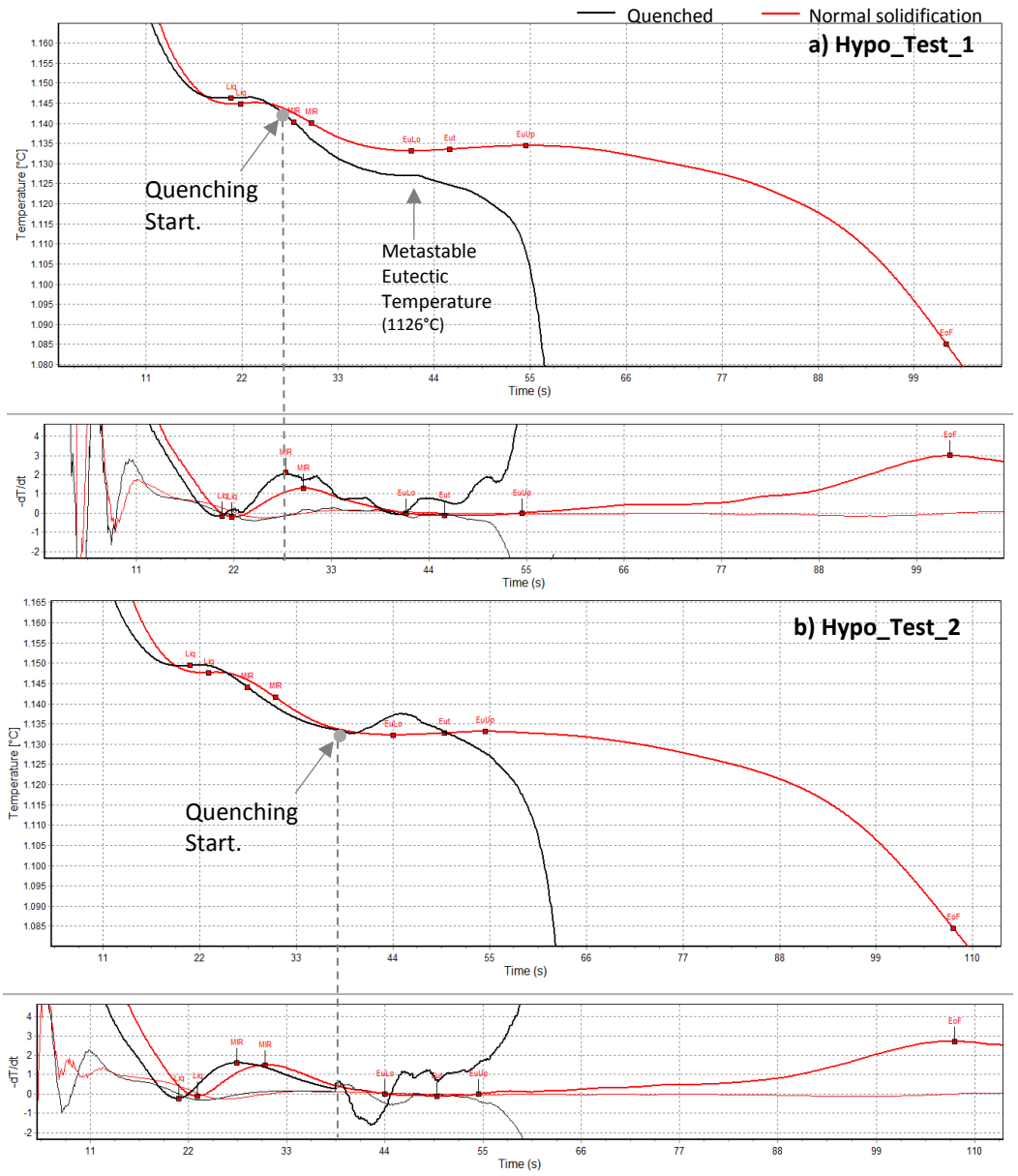

Figure 79 - Solidification curves for the quenching testes on hypoeutectic melts with quenching after the liquidus temperature (a) and before the eutectic low temperature (b).

The characteristic microstructure obtained after the quench test, using Nital etching, is presented in micrograph from a hypoeutectic sample in **Figure 80**, showing the evolution of the solidification front. A detail of the metallographic constituents is presented **Figure 81**, where graphite, pearlite and iron carbides are present. The **Figure 80** refers to a periphery region of the sample and shows the main metallographic constituents that result from tests of this nature, as well as the evolution of the solidification microstructure. It is observed that there are less iron carbides (liquid before quenching) close to the boarder of the sample, compared to the region

close to the centre. It is also visible that there is a bigger density of nodules close to the boarder. As we approximate to the centre of the sample the number of nodules decreases and the amount of carbides increases, indicating that the solidification was there still at an earlier stage. The dendritic structure is clearly observed close to the centre of the sample, showing also wide arm spacing. Close to the boarder, the dendritic structure is not so clearly visible due to the solidification of the austenite shells around the nodules and the complete solidified structure is evener, indicating that at that point the dendritic coherency point has already occurred.

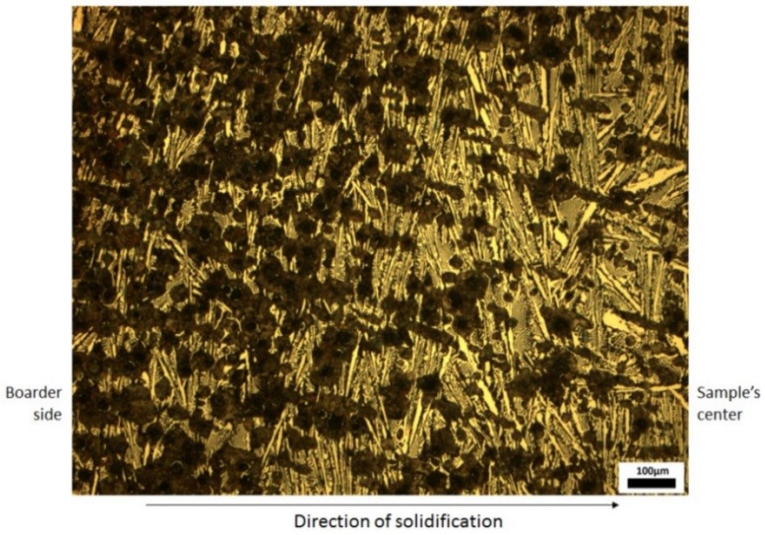

Figure 80 - Microstructures of the quenched sample Hypo_test_1, showing the evolution of the solidification microstructure. Micrograph obtained after etching with Nital 4%.

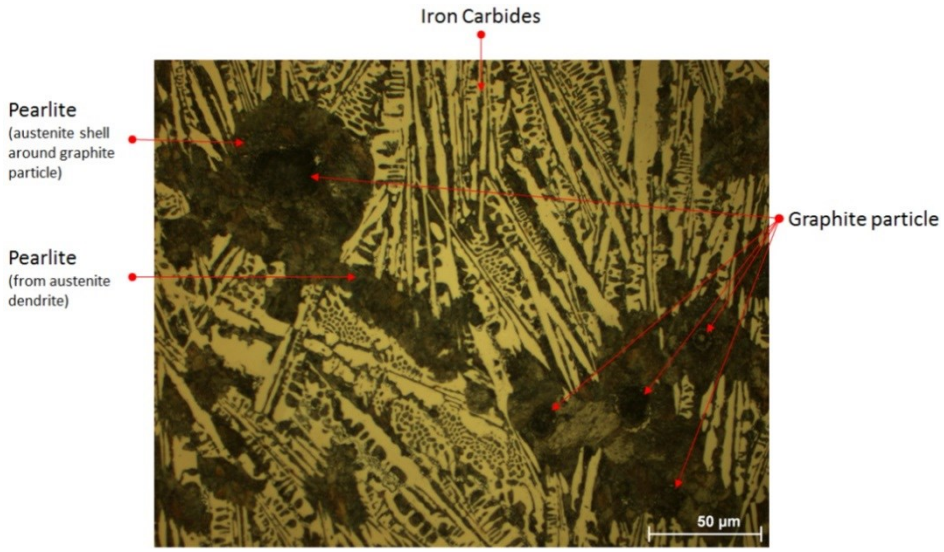

Figure 81 - Micrograph from sample Hypo_Test_1, showing the detail of the metallographic constituents. Micrograph obtained after etching with Nital 4%.

The microstructure obtained from the quenching of samples Hypo_Test_1 and Hypo_Test_2 are presented in **Figure 82** respectively. From the figure, it is observed that the dendritic structure is more developed (higher amount and higher density) in the Hypo_Test_2 sample, compared to Hypo_Test_1, as a result from the interruption of the solidification at a later stage.

From the Hypo_Test_1 sample (**Figure 82a**) the following qualitative observations are made, that correspond to the evolution of the solidification structure after the liquidus temperature and before the MIR point of the solidification curve:

- There is a much lower amount of solid phase;
- The main dendrite arms are long and spaced between each other;
- The secondary arm branching in almost non-existing;
- There are were still wide areas of liquid in the microstructure (now represented by carbides);
- There is a presence of small graphite nodules along the primary arms of the dendrites, with a diameters up 24μm enveloped in a thick austenite hallo;

From the Hypo_Test_2 sample (**Figure 82b**) the following qualitative observations are also made, that correspond this time to the evolution of the solidification structure close to the eutectic low temperature:

- There is a much higher amount of solid phase, when compared to the Hipo_Temp_1;
- The main dendrite arms are long and spaced between each other, as in the sample Hipo_Temp_1;
- The secondary arm branching is much more significant, giving a much more dense dendritic structure;
- There are less areas of liquid in the microstructure (represented in the micrograph by carbides);
- There is higher amount of graphite particles than in the sample Hipo_Test_1, with a diameter up 36μm, with the characteristic that they are not growing only along the dendrite arms, but also in the middle of the liquid area (there is no contact between the austenite halo around the graphite nodule and the dendrite arms) as highlighted in **Figure 83**.

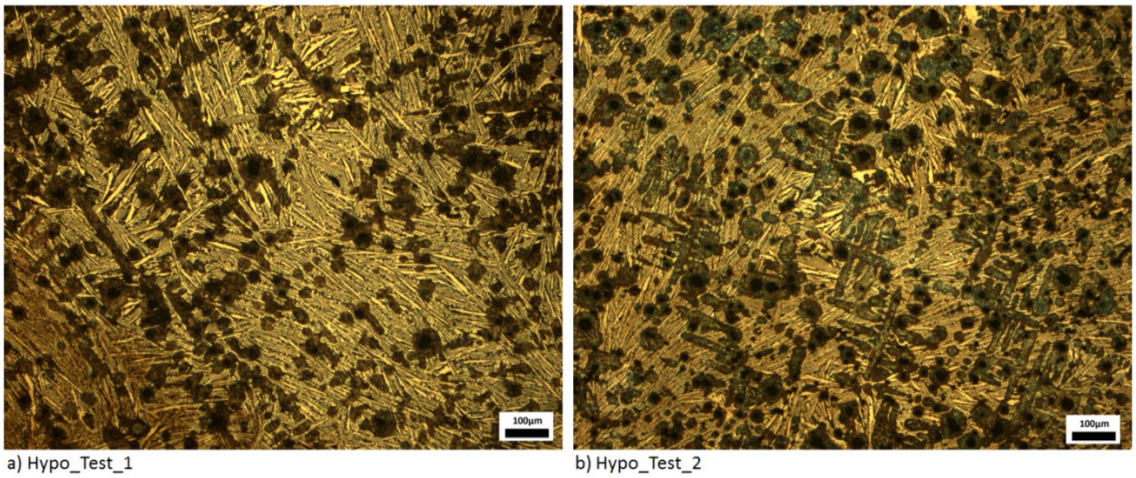

Figure 82 - Micrographs from the samples Hypo_Test_1 (a) Hypo_Test_2 (b) at the center of the samples. Micrographs obtained after etching with Nital 4%.

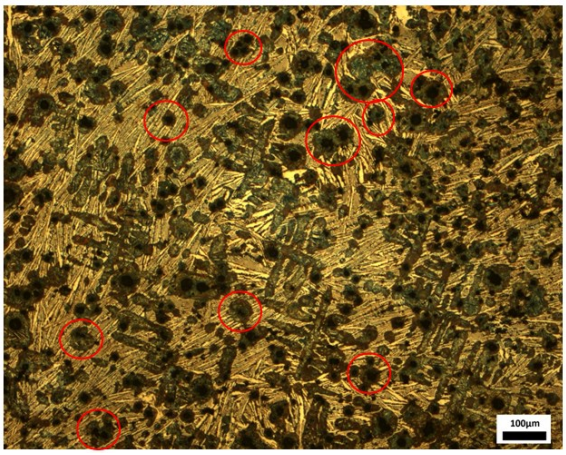

Figure 83 - Same micrograph as Figure 82b with a highlight on the nodules that seem to nucleate and grow from the bulk liquid.

In terms of development of the graphite structure, the micrographs without etching for the two tempered sample and the normal solidification sample, are presented in **Figure 84**. From the micrographs it is visible that for the sample quenched after the liquidus temperature (**Figure 84b**), there are already some graphite particles solidified. When the sample is etched (like in the micrograph from **Figure 82a**) this particles appear along the main dendrite arms. When the interruption of the solidification is made before the eutectic low, the micrograph presented in **Figure 84b** indicates a higher amount of graphite particles that appear more randomly in the

sample's area. The main characteristics of the microstructures presented from samples Hipo_Test_1, Hipo_Test_2 and normal solidification sample are presented in the **Table 18**.

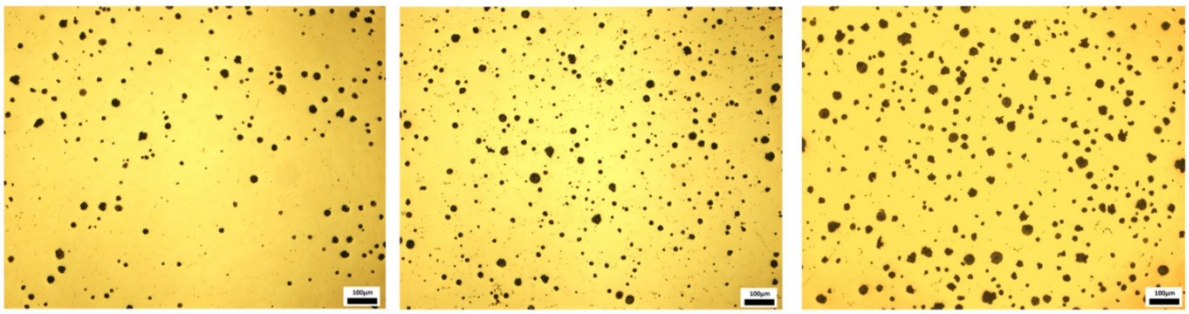

Figure 84 - Micrographs without etching from the quenched samples Hipo_Test_1 and HIpoTest_2 and normal solidification AccuVo-Cup sample.

Table 18 - Comparison of the main microstructure characteristics of the hypoeutectic quenched samples.

	Hypo_Test_1	Hypo_Test_2	Normal
Solid Phase [%]	21	45	100
Graphite Phase [%]	1,8	3,9	7,1
Graphite particle density [1/mm^2] (Ø>20µm)	14	43	112
Max. graphite particle diameter [µm]	24	36	47
Average dendrite's main arm length [µm]	502	512	-
Average primary dendrite arm spacing [µm]	271	211	-
Average secondary dendrite arm length[µm]	Almost Inexistent	116	-
Average secondary dendrite arm spacing [µm]	Almost Inexistent	32	-

5.1.2. Microstructure evolution of eutectic melts during solidification using thermal analysis

The solidification curve from the quenching test applied to eutectic solidification morphology is presented in **Figure 85**. From the curve it is visible that, although the quenching started at the middle point between the EuLo and EuUp, the temperature drop in the sample started only close to the EuUp point.

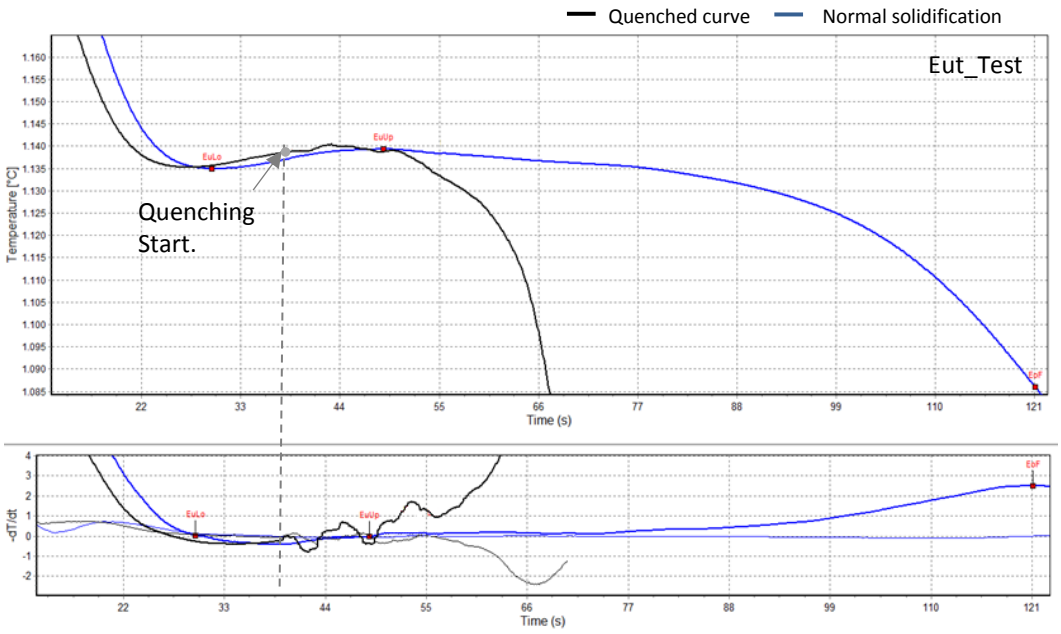

Figure 85 - Solidification curves for the quenching testes on a eutectic melt (according to curve morphology) with quenching between the EuLo and EuUp.

From the microstructure presented in **Figure 86** it is visible that the sample is almost solidified completely. Only at intercellular regions there is still remaining liquid, indicating that after these EuUp point, only the intercellular regions will solidify, and total percentage of solidified phase is 78%.

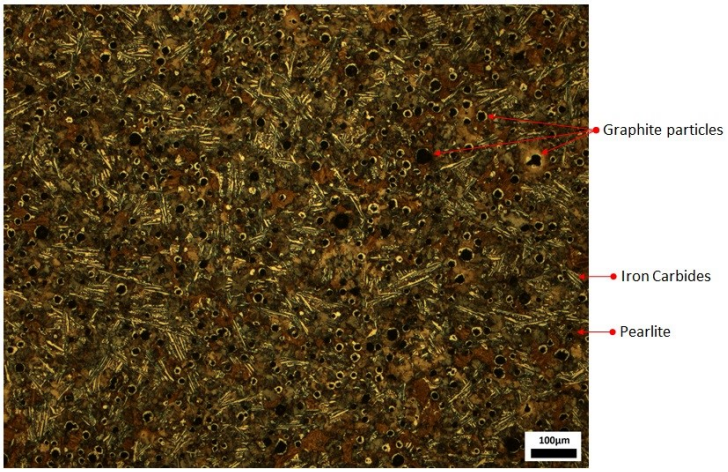

Figure 86 - Micrograph from the eutectic samples after quenching, at the thermic center, obtained after etching with Nital 4%.

The micrographs for the evaluation of the graphite structure for the eutectic samples, after quenching and normal solidification, are presented in **Figure 87**, showing that there is no significant change between the graphite structures of both samples. This means that at the point the quenching was done, the solidification structure of the graphite was almost complete developed. The microstructure characteristics presented in **Table 19** indicate also that the graphite particle microstructure from the quenched sample is also close to the results obtained for the normal solidification sample.

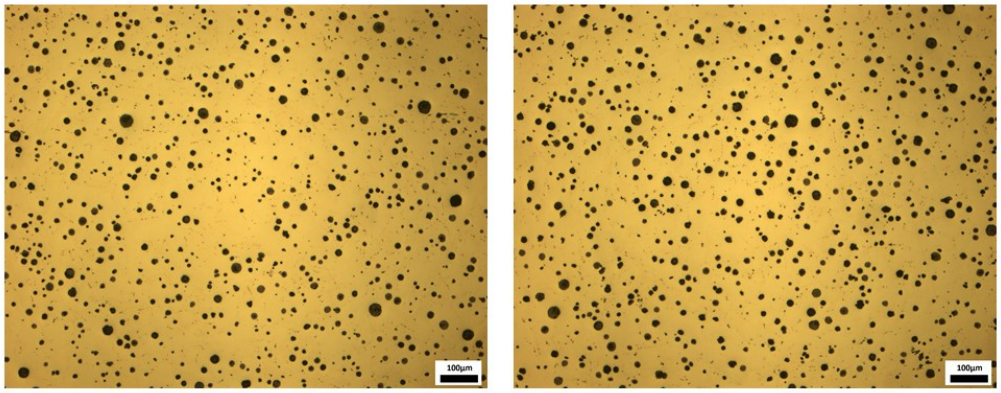

Figure 87 - Micrographs without etching from the quenched sample and normal solidification AccuVo-Cup sample.

Table 19 – Main microstructure characteristics from the quenched and not quenched eutectic sample.

	Eut_Test	Normal
Solid Phase [%]	78	-
Phase Area of Graphite [%]	6,9	7,3
Graphite particle density [1/mm^2] (Ø>20µm)	150	175
Max. graphite particle diameter [µm]	34	36

5.1.3. Microstructure evolution of hypereutectic melts during solidification using thermal analysis

For the quenching test performed to the melt with hypereutectic solidification morphology, the solidification curves are presented in **Figure 88**. The solidification curve for the test with the quenching of the thermal analysis cup after the occurrence of the liquidus temperature (Hyper_Test_1) is presented in **Figure 88a**, and in **Figure 88b** the solidification curve with

quenching before the eutectic (Hyper_Test_2). The resulting microstructures from the quenched samples, at the thermic centre, are presented in **Figure 89a** for the Hyper_Test_1 sample and **Figure 89b** for the Hyper_Test_2.

The main observation made to the microstructure from sample Hyper_Test_1 (**Figure 89a**) are the following:

- There is a considerable presence of graphite particles with big diameters (up to 38μm) that form right after the liquidus temperature, indicating that they are primary graphite particles. These particles are bigger than any of the particles found for the hypoeutectic and eutectic test;
- This primary graphite particles seam to nucleate directly from the liquid, once some of this particle seem to have floated at collide with each other, causing they agglomeration;
- The microstructure reveals also the presence of short but ramified dendrites (possible equiaxed dendrites), smaller than the ones from the hypoeutectic test.

For the microstructure from sample Hyper_Test_2 (**Figure 89b**) the following observations are made:

- The nodular graphite particle size increased even further, to a maximum diameter of up to 55μm;
- There is a higher density of big sized graphite particles;
- The amount of solid phase increased;
- The amount of dendrites present are equivalent to the Hyper_Test_1, although their visualization is more difficult due to the coarsening of the solidification structure;
- The austenite shell surrounding the nodular graphite particles is thicker than for the sample Hyper_Test_1.

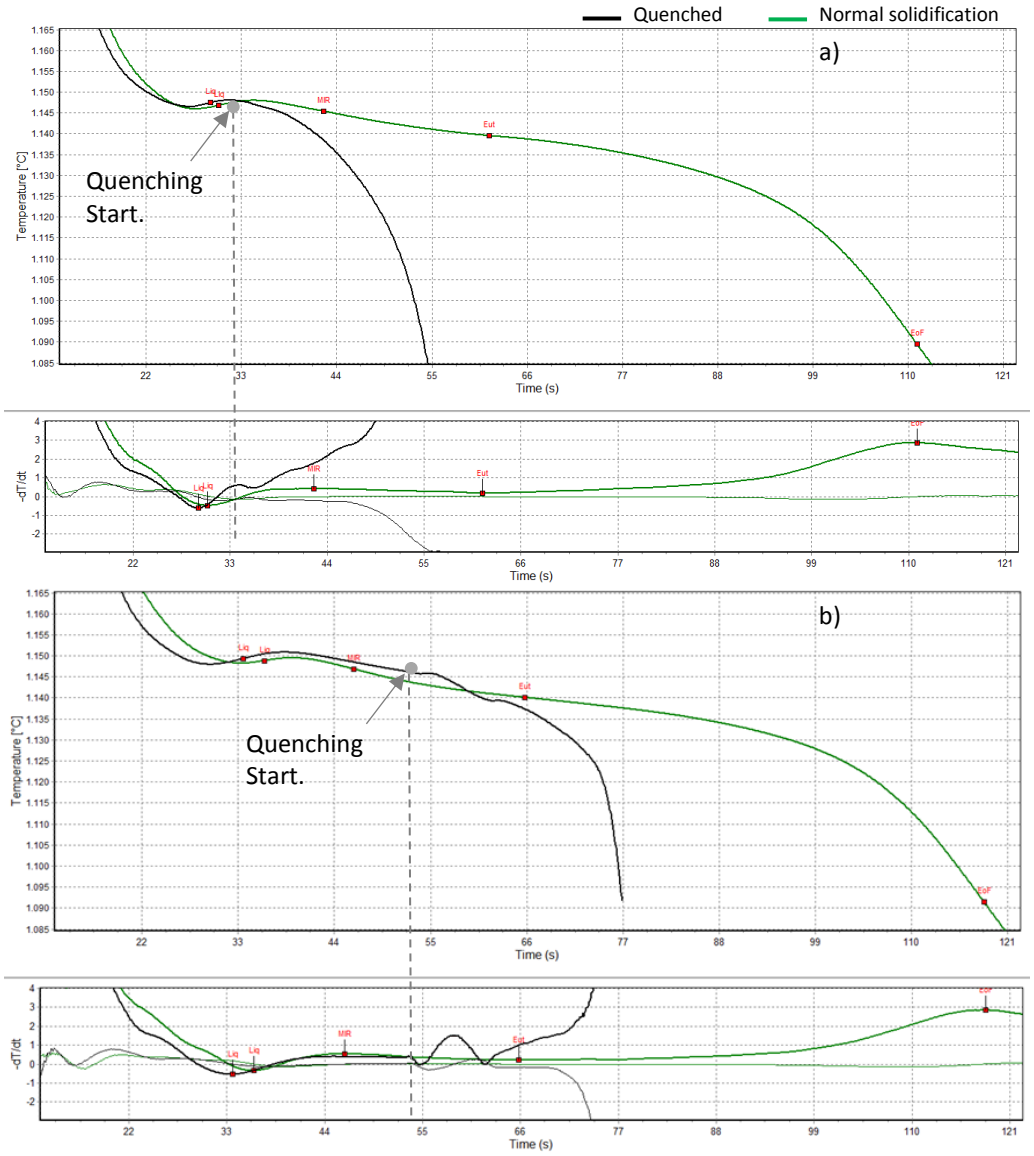

Figure 88 - Solidification curves for the quenching testes on hypereutectic melts with quenching after the liquidus temperature (a) and before the eutectic temperature (b).

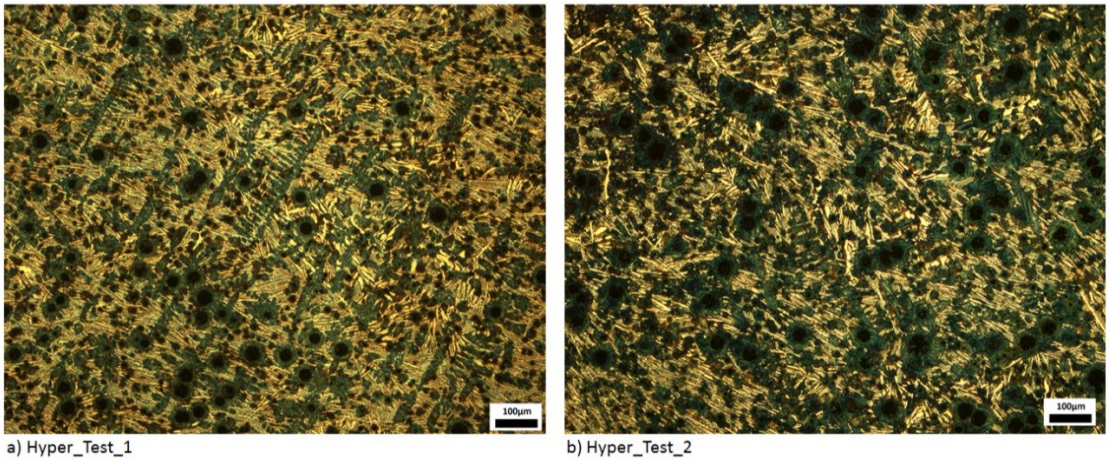

Figure 89 - Micrographs from the samples Hyper_Test_1 (a) Hyper_Test_2 (b) at the center of the samples. Micrographs obtained after etching with Nital 4%.

A more detailed observation of the sample Hyper_Test_1, presented in the micrograph from **Figure 90**, shows the presence of small graphite particle nodules that have nucleated on the bulk liquid melt. These particles have a diameter smaller than 15µm, and are already being enveloped by a shell of austenite (in **Figure 90** appearing as martensite). No graphite particle, with diameter of 15µm or higher was found without an austenite envelope, partial or total.

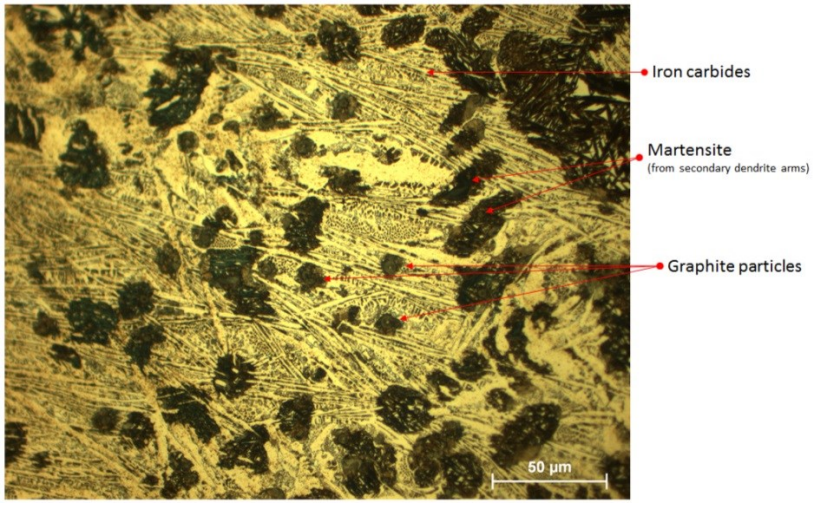

Figure 90 - Detailed observation of the graphite particles early growth stage, showing the envelopment of the graphite by a austenite shell. . Micrographs obtained after etching with Nital 4%.

The observation of the samples micrographs without etching in the micrographs from **Figure 91**, show how the graphite particle structure changes during the different solidification moments.

After the liquidus temperature, for the sample Hyper_test_1 presented in **Figure 91a**, there is already 3,8% of graphite in the structure and the nodule size reaches a diameter up to 44µm. As the solidification precedes the graphite particle size continues to grow and at the eutectic point (see **Figure 91b**) it reaches up to 56 µm and an amount of graphite of 5,1%. The final microstructure has a graphite nodule size of up to 67µm and it is characterized by big primary graphite nodules and smaller nodules that nucleated and growth during the eutectic (see **Figure 91c**).

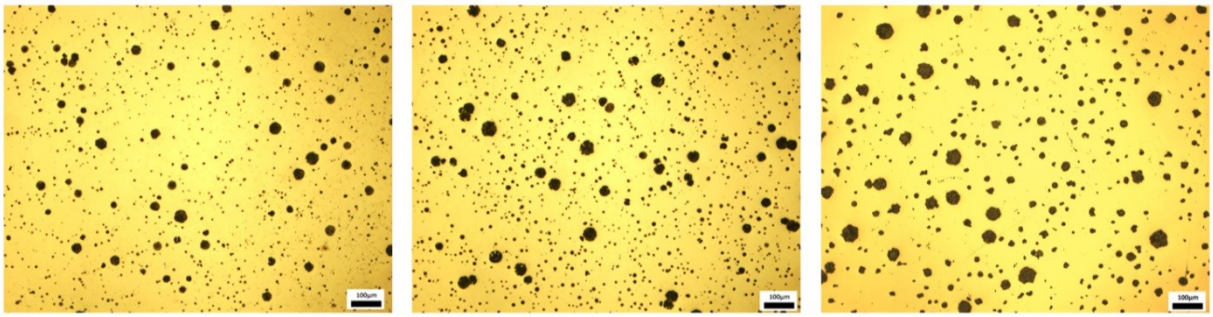

Figure 91 - Micrographs without etching from the quenched samples Hyper_Test_1 and HypeTest_2 and normal solidification AccuVo-Cup sample.

Table 20 summarized the main microstructure characteristics for the samples resulting from the quenching test of the hypereutectic melt.

Table 20 - Comparison of the main microstructure characteristics of the quenched and not quenched hypereutectic samples.

	Hyper_Test_1	Hyper_Test_2	Hyper_Normal
Solid Phase [%]	34	53	-
Phase Area of Graphite [%]	3,8	5,1	8,1
Graphite particle density [1/mm^2] (Ø>20µm)	38	55	96
Max. graphite particle diameter [µm]	44	56	67
Average dendrite's main arm length [µm]	245	259	-
Average primary dendrite arm spacing [µm]	230	262	-
Average secondary dendrite arm length[µm]	53	69	-
Average secondary dendrite arm spacing [µm]	27	25	-

5.2. Forecast of dendritic coherency point in nodular cast iron solidification curves

In this following test, the application of the methods for determination of the dendritic coherency point, usually applied to Aluminium alloys, were tested for cast iron melts.

For the experiments, a thermal analysis cup AccuVo was used, where in one chamber the hot junction of the thermocouple was placed at the centre of the chamber and in the second chamber the hot junction is close to the wall of the cup. This way it is achieved the same two thermocouple experimental principal used by Bäckerud, presented in chapter 3.5.2.4.

The first experiments were made using a nodular cast iron melt, at a foundry that used a pouring furnace process and have always hypoeutectic melt compositions. The thermal analysis samples were taken from inside the pouring furnace. One sample was made at the filling steps of the furnace to obtain a sample with a high liquidus temperature (DCP_Hypo_1). The second sample was obtained from the normal running production and the last one with an increased addition of carbon to have a eutectic solidification morphology. The treatments were performed using FeSiBa inoculant (SB5) and FeSiMg alloy added to the transport ladle using a wire treatment machine. The chemical compositions of the main elements from the three melts are presented in **Table 21**. No trials with a hypereutectic melt were possible to be performed at that time.

Table 21 - Main spectrometer data and liquidus temperature from the samples used on the dendritic coherency point trials.

Melt type	Solidification morphology	Liq. temp. [°C]	Si [%]	Mn [%]	P [%]	S [%]	Cu [%]	Sn [%]	Mg [%]
DCP_Hypo_1	Hypoeutectic	1190	2,31	0,34	0,012	0,006	0,031	0,010	0,032
DCP_Hypo_2	Hypoeutectic	1152	2,43	0,30	0,012	0,005	0,022	0,010	0,043
DCP_Eut	Eutectic	-	2,48	0,32	0,013	0,005	0,026	0,010	0,047

The trials for the coherency point in hypereutectic melts were performed in foundry conditions, simultaneously with the trials from chapter 5.1 for the study of the microstructure evolution during solidification. The melts used are the Hyper_Test_1 and Hyper_Test_2 from **Table 17**.

The result obtained for the two samples are identical, and hereby the results from sample Hyper_Test_2 are presented and renamed has DCP_Hyper.

The microstructures obtained from the thermal analysis samples of the tested melts, are presented in **Figure 92**, showing that all samples had nodular graphite shape.

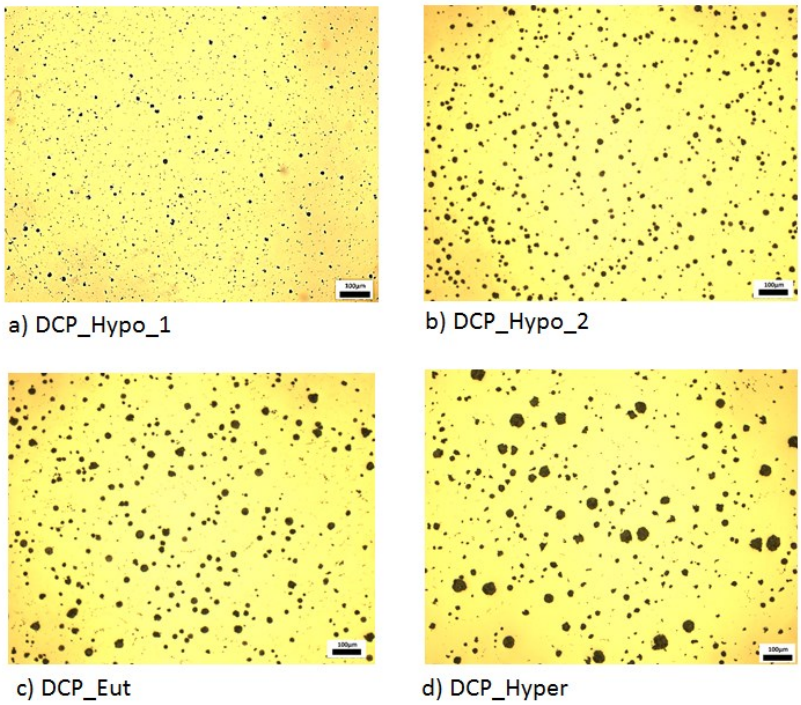

Figure 92 - Micrographs from the thermal analysis samples obtained at the DCP trials. Micrographs obtained after polishing.

The solidification curves obtained from the tests are presented in **Figure 93**. At the figure, for each test, the solidification curve and the derivatives are presented, where the red curve represents the thermocouple at the centre of the sample and the green curve the thermocouple close to the interior wall of the cup.

From **Figure 93a**, from sample DCP_Test_1, it is possible to observe a small difference on the cooling stage between the liquidus temperature and the eutectic plateau, and later on after the eutectic plateau until the EoF point. Following Bäckerud's model, a curve representing the temperature difference between the solidification curve in the centre and in the wall, is also plotted together with the two solidification curves. According to Bäckerud's model the dendritic

coherency point will correspond to the first minimum in this temperature difference curve occurring after the beginning of solidification (liquidus temperature). The dendritic coherency point, resulting from this method, is indicated also in the same figure. A projection of this point in the 1st and 2nd derivative curves (bottom graphic from **Figure 93a**) show that it approximately matches the first maximum in the 1st derivative curve and the zero of the 2nd derivative, that correspond to the MIR point in the red solidification curve. More exactly, and after a detailed observation of the 1st derivative curve, the dendritic coherency point matches the point where the cooling rate of the red curve turns higher than the one from the green curve (the 1st derivative lines cross each other), which happens just less than a second after from the maximum point.

In the **Figure 93b**, for a sample DCP_Test_2 with a lower liquidus temperature than DCP_Test_1, the same observation made for the **Figure 93a** are valid. Also here an exact match exists between the coherency point and the moment when the cooling rate of the red curve turns higher than the cooling rate of the green curve. In this specific case it happens shortly before the maximum cooling rate is achieved.

In the case of the eutectic solidification curve, presented in **Figure 93c** the coherency point occur short after the eutectic low point, more exactly when the 2nd derivative reaches zero, after the beginning of solidification, corresponding also to the 1st minimum of the 1st derivative curve. It is a similar situation as for the hypoeutectic curves, but this time the coherency point occurs during the recalescence period of the eutectic transformation.

For the test in a hypereutectic solidification curve, the coherency point occurs at the time of the liquidus upper temperature, corresponding to the 1st maximum of the 2nd derivative curve after the liquidus low temperature.

By observation of the time of occurrence of the coherency point for the 4 melts tested, is can be found that as the melt goes from hypoeutectic to hypereutectic, and knowing that the maximum temperature registered by the thermal analysis system changed only between 1298°C to 1310°C, the coherency point occurs slightly later (approximately 6 seconds between a DCP_Test_2 and DCP_Test_4).

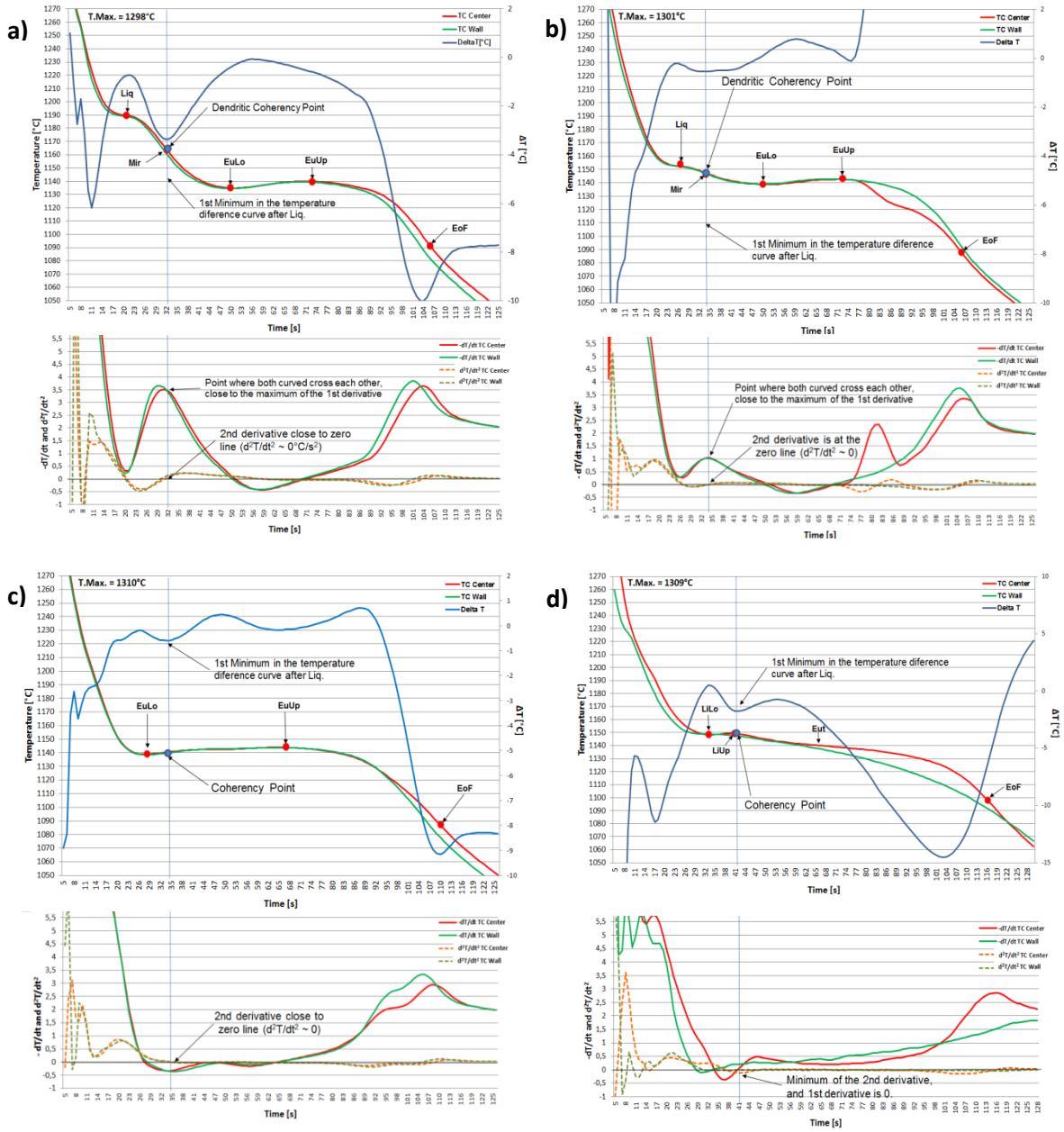

Figure 93 - Determination of the dendritic coherency point using Bäckerud's model, for the samples: a) DCP_Test_1; b) DCP_Test_2 and c) DCP_Test_3

The analysis of the derivative curves displayed versus the temperature (used by Djordjevic), from all 4 samples, is presented in **Figure 94**, considering only the derivatives from the thermocouple positioned at the centre of the sample. In the case of hypoeutectic curves, the observation of **Figure 94a** and **b**, shows that the dendritic coherency point matches exactly the point where the 2nd and 3rd derivative cross (have the same value) after the liquidus temperature (see **Figure 94a**

and **b**). The use of this point is more accurate to match with the minimum on the ΔT curve than the maximum of the first derivative.

For the eutectic and hypereutectic curves, it confirms the observations made directly at the 1st and 2nd derivative curve, and do not give additional and a more accurate determination of the coherency point. For a eutectic composition the minimum of the ΔT curve matches the minimum of the 1st derivative and for the hypereutectic the minimum of the 2nd derivative. A detail view of the **Figure 94d** is presented in **Figure 95**.

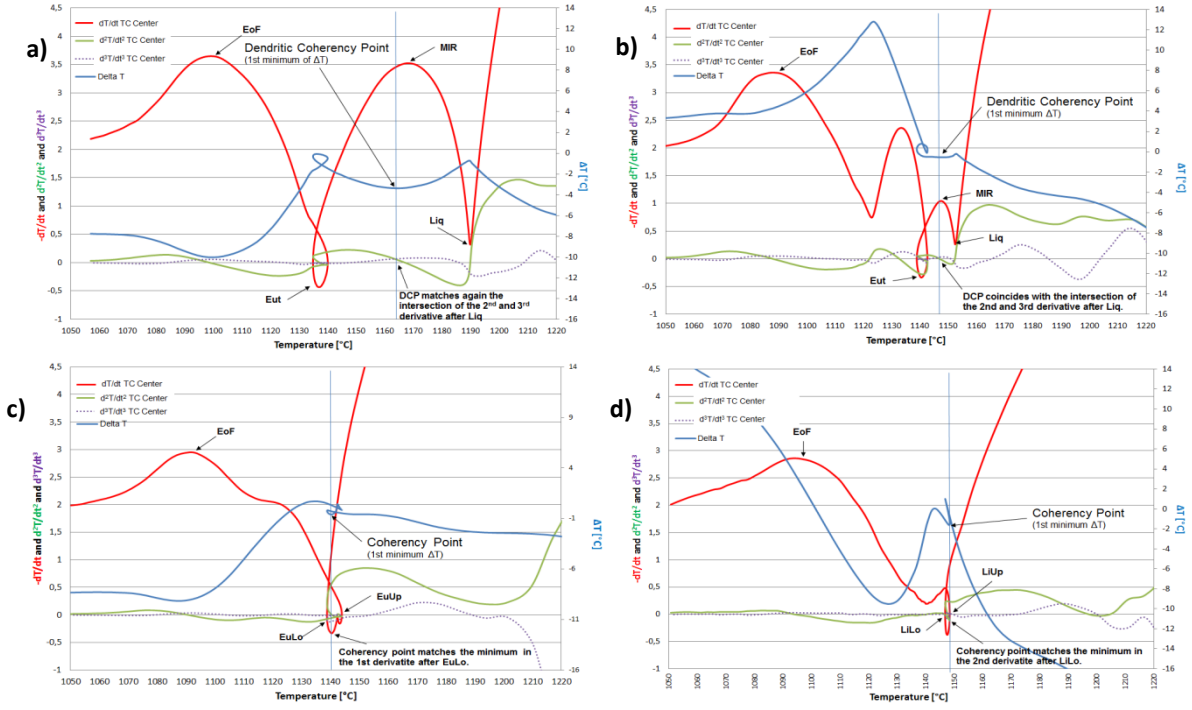

Figure 94 - Display of the solidification curve's derivatives and temperature difference curve as a function of temperature, for the samples used in the dendritic coherency test.

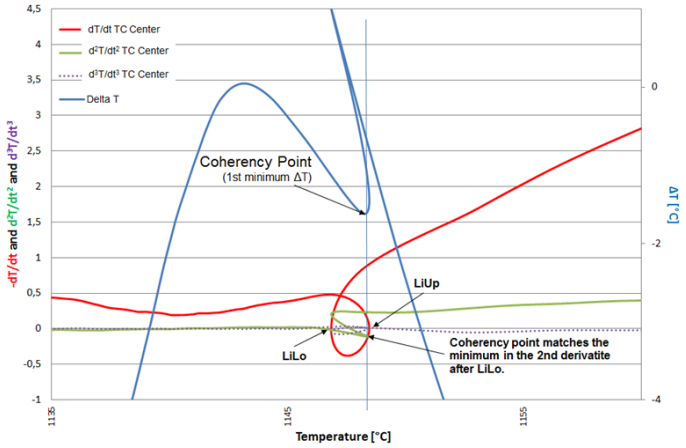

Figure 95 - Detailed view of Figure 94d at the point of coherency.

After this analyses, a resume of the main points that allows the estimation of the dendritic coherency point are presented in **Table 22**.

Table 22 - Points from thermal analysis that better match coherency point for different solidification morphologies of cast iron.

Curve morphology	Point that matches the time of coherency	Graphic type
Hypoeutectic	Moment where 2nd and 3rd derivative curves cross after liquidus temperature	Derivative Vs. Temperature
Eutectic	1st minimum of the 1st derivative after eutectic low temperature	Derivative Vs. Time
Hypereutectic	1st minimum of the 2nd derivative after liquidus low temperature	Derivative Vs. Time

5.3. Relation between C.E. value and thermal analysis solidification morphology

As mentioned before in this thesis introduction, the equilibrium diagram does not represent the real solidification conditions in the foundry. Nevertheless, the equilibrium diagram is still often used in the foundry practice as a reference, specially the C.E. value, to evaluate the melt's solidification morphology. In order to evaluate the discrepancy between the equilibrium solidification morphology and the real solidification morphology, an experiment was conducted, in foundry conditions, described below. The main purpose of this test was to obtain a melt with

different C.E. values, by increasing the carbon content, to evaluate how the solidification morphology of the melt really changed by measuring it using thermal analysis.

A standard base iron melt for production of GJS400 grade was prepared, using pig iron, GJS 400 returns, steel scrap and alloying elements in an induction furnace, to obtain the base chemical composition from **Table 23**.

Table 23 - Base Iron chemical composition from the melt used in the C.E. and solidification morphology trials.

$C_{(Leco)}$ [%]	Si [%]	Mn [%]	P [%]	S [%]	Cu [%]	Sn [%]	Ni [%]	Cr [%]	Pb [%]
3,45	1,45	0,25	0,026	0,013	0,025	0,003	0,023	0,023	0,001

From the same base iron melt, five treated melts were used in this trial, with approximately the same treatment additions and with increasing carbon content. The carbon additions to increase the C.E. value were either given to the base iron melt furnace between tapings (if the requires increase of carbon was big) or directly to the ladle when tapping (if the carbon addition was small, up to 2 Kg/ton), as illustrated in **Figure 96**. The ladle treatment was performed by a cored-wire treatment method using the treatment wires composition presented in **Table 24**. After each treatment a sample of the melt in the ladle was taken into one thermal analysis samples and a spectrometer sample. The thermal analysis AccuVo®-cup, was empty in one chamber, while the other contained 0,04% FeSiCaAl inoculant alloy with approximately 1% of Bi and 1% RE[14] (hereby named Inoc.-Bi; complete specification given in **Table 29**), considered to be a powerful inoculant for nodular graphite cast iron, originating a high nodular graphite particle count [77]. The purpose of testing the melts reaction to the inoculant present in the thermal analysis cup is to evaluate the effect that the inoculation potential has in the solidification morphology of the melt.

[14] RE – Rare Earth (also denominated as Mischmetal (CerMM)): Alloy containing a mixture of rare earth elements, with an approximate composition of 45-52% Ce, 20-27% La, 15-18% Nd, 3-5% Pr and 1-3% combination of Sm, Tb and Y.

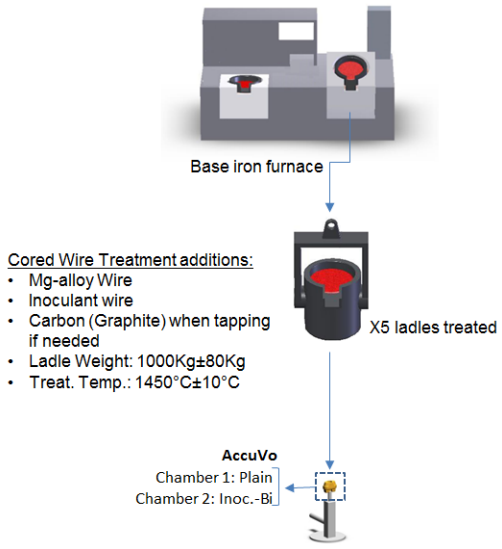

Figure 96 - Illustration of the trials procedures for evaluation of the relationship between C.E. and real solidification morphology.

Table 24 - Treatment wires composition used in the trials for relation between C.E. and solidification morphology determined by thermal analysis.

	Si (g/m)	Ca (g/m)	Mg (g/m)	Ba (g/m)	Al (g/m)	RE (g/m)	C (g/m)
Nodularizer	106	5	43	-	-	1,3	24
Inoculant	103	4,4	-	31	4,3	-	-

The addition given to the melt in the base iron and at the ladle for each treatment, are presented in **Table 25**. The sample name (Ladle ref.) has altered after the trials to match the liquidus temperature obtained from each ladle to allow a better recognition of the sample.

Table 25 - Additions made to the melt, in the furnace and ladle, during the performance of the trials for evaluation of the relation between C.E. and the real melt's solidification morphology.

Ladle ref.	C add in furnace [Kg]	Ladle's melt weight [Kg]	C add in ladle [Kg]	Treat. temp. [°C]	Nodulizer [m]	Inoculant [m]
SM_1181	11	1030	0	1438	31,0	15
SM_1173	9	1070	0	1445	33,2	18,2
SM_1150	18	1010	0	1462	33,9	17,8
SM_1148	0	1030	0,3	1446	33,5	17,6
SM_1145	0	1000	0,2	1436	33,1	17,9

The chemical composition results obtained for the melts after treatment are presented in **Table 26** , where also the C.E. value is calculated using the formula from **Equation 3.**

Table 26 - Main spectrometer results from the ladle's melt after treatment used in the trials for evaluation of the relation between C.E. and the real melt's solidification morphology.

Ladle ref.	C.E. [%]	C (Leco) [%]	Si [%]	Mn [%]	P [%]	Mg [%]	S [%]	Cu [%]
SM_1181	4,11	3,40	2,11	0,241	0,026	0,041	0,007	0,026
SM_1173	4,16	3,44	2,15	0,234	0,025	0,035	0,007	0,025
SM_1150	4,36	3,63	2,20	0,271	0,028	0,039	0,006	0,025
SM_1148	4,42	3,73	2,08	0,280	0,028	0,037	0,007	0,029
SM_1145	4,45	3,74	2,12	0,268	0,026	0,038	0,007	0,024

The solidification curves obtained from each of the ladle melts treated, from the thermal analysis cup chamber that was empty, represents the actual melt quality after treatment. The main thermal analysis information is presented in **Table 27** and are presented graphically in **Figure 97a**, together with the projection of their liquidus temperature to correlate it with the C.E. value obtained, presented in **Figure 97b**.

Table 27 - Main thermal analysis results from the ladle's melt after treatment used in the trials for evaluation of the relation between C.E. and the real melt's solidification morphology.

Ladle ref.	T.Liq. [°C]	EuLo [°C]	EuUp [°C]	TA curve solidification morphology
SM_1181	1181	1132	1140	Hypoeutectic
SM_1173	1173	1136	1137	Hypoeutectic
SM_1150	1150	1137	1138	Hypoeutectic
SM_1148	1148	1138	1139	Hypoeutectic
SM_1145	1145	1136	1139	Hypoeutectic

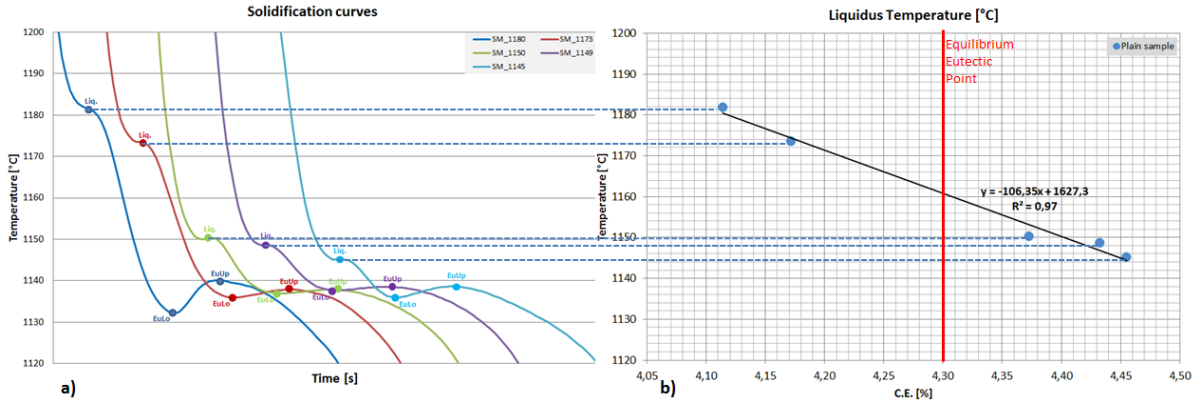

Figure 97 - a) Solidification curves obtained during trials; b) correlation between the liquidus temperature from the solidification curve and the C.E. value.

The observation of the **Figure 97b**, confirms the good correlation between the liquidus temperature of the solidification curve, with a correlation coefficient of 0,97. The results reveal also, that although we have reached during trials a C.E. that is eutectic and even hypereutectic following the Fe-C equilibrium diagram, the thermal analysis results show that all curves solidified with a hypoeutectic morphology. This is observed even for the sample SM_1145, that has a C.E. value of 4,45% and still solidifies hypoeutectic.

The comparison between the curve from the thermal analysis cups without additional inoculant (plain) and the curve with additional Inoc.-Bi inoculant, presented in **Figure 98**, show that the solidification morphology of the melt can change from hypoeutectic to eutectic as a consequence of inoculation, when the liquidus temperature is below 1150°C, that correspond also to melt composition that have a C.E. equal or higher than the equilibrium eutectic point (see **Figure 98d** and **e**). For curves with lower C.E. value, and consequently higher liquidus temperature, case of the curves **Figure 98a**, **b** and **c**, this influence of the inoculant of the solidification morphology variation is not seen.

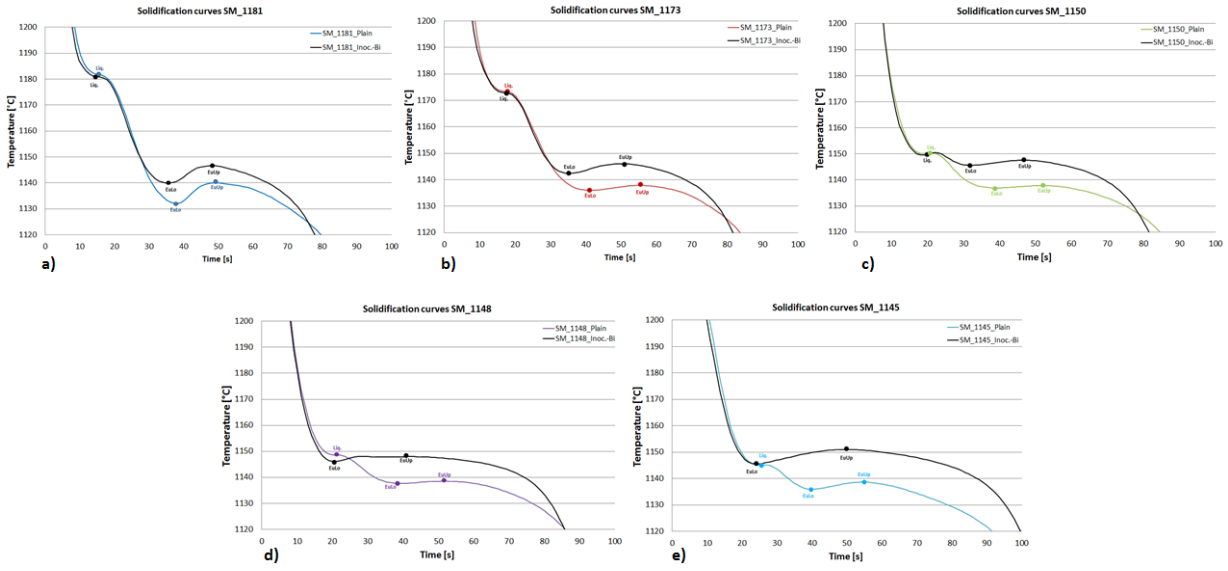

Figure 98 - Comparison between the solidification curves from the different chambers of the AccuVo®-cup, without and with additional Inoc.-Bi inoculant (present at the 2nd chamber).

The results from these trials suggest therefore, that the solidification morphology of the melt for composition above the eutectic point is highly dependent on the inoculation potential of the melt. If the melt has a low inoculation potential, it will still have hypoeutectic solidification morphology, although the C.E. is characteristic of eutectic and even hypereutectic composition. This demonstrates that, the use of the C.E. as a control parameter of the solidification morphology of the melt is not accurate.

5.4. Evaluation of the melt's inoculation efficiency for different inoculant types using thermal analysis

Following the results that show how important the inoculation state is on the solidification morphology of the melt, and following the importance that has for foundries the correct evaluation of the inoculation potential of the melt during processing for the active correction and adjustment of that same inoculation, a trial was conducted to study the influence of different inoculants in the melt. The purpose of the trial is to evaluate the inoculation potential of the different commercially available inoculants and their influence in the microstructure, but also evaluate the impact that they have on the solidification morphology of the melt when that same melt is above the C.E. value range where its solidification morphology will depend greatly in the inoculation potential.

This trial was once again conducted under industrials conditions, in a real foundry, where one base iron melt was used for this study. A base iron melt for production of GJS500 grade was prepared, using pig iron, returns, steel scrap and alloying elements in an middle frequency induction furnace, to obtain the base chemical composition presented in **Table 28**.

Table 28 - Base iron chemical composition from the trials to study the inoculation potential of different inoculants.

$C_{(Leco)}$ [%]	Si [%]	Mn [%]	P [%]	S [%]	Cr [%]	Ni [%]	Mo [%]	Cu [%]	Ti [%]	Al [%]
3,69	1,5	0,28	0,02	0,015	0,026	0,017	0,004	0,54	0,006	0,001

From the same base iron melt a total of 10 ladles where treated, using the nodulizer and inoculant wires from **Table 24** and from each melt treated 6 thermal analysis cups AccuVo® were poured containing different types of inoculants in their chambers. The illustration of the trials procedure is presented in **Figure 99**, with indication of the inoculants present in each thermal analysis cup. Each cup contained two different types of inoculant (one at each chamber of the cup) in the amount of 0,04%.

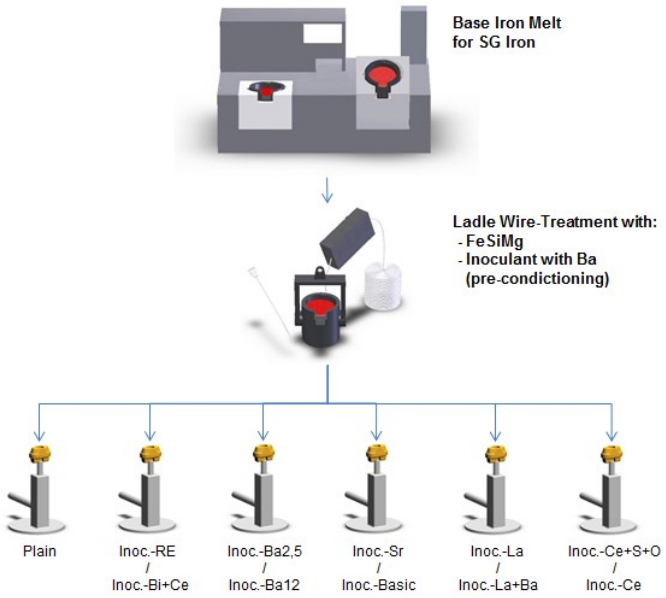

Figure 99 - Illustration of the procedure for evaluation of the inoculation potential of different inoculants using thermal analysis.

The composition of each one of the inoculants used is presented in **Table 29** and follows the specification given by the inoculant suppliers. Once the intention here is to test the inoculation effect of each inoculant in the melt based on their active elements and in order to avoid any beneficial or negative impact on the inoculant brands, the commercial name of the inoculants was hereby replaced by another name that has associate the main active elements present at that same inoculant.

Table 29 - Composition of the inoculants used inside the thermal analysis cups, for the trials on the evaluation of the inoculant effect on the melt.

Non-commercial inoculant name	Si (wt.%)	Ca (wt.%)	Al (wt.%)	Ba (wt.%)	Sr (wt.%)	Bi (wt.%)	R.E. (wt.%)	La (wt.%)	Ce (wt.%)	S+O (wt.%)
Inoc.-Re	40-42	0,56	0,6				9,6			
Inoc.-Bi+Ce	62-66	1,8–1,4	0,8			0,8 – 1,2			0,8 – 1,2	
Inoc.-Ba2,5	63-65	1,26	1,43	2,5						
Inoc.-Ba12	60-70	0,5–1,5	1–1,8	11,5–12,5						
Inoc.-Sr	74-79	0,1	0,5		0,8–1,2					
Inoc.-Basic	68-73	0,3–1,5	3,2-4,5							
Inoc.-La	45–50	2,5	1,5					1,8 – 2,2		
Inoc.-LaBa	73	1,3	1	0,9				1		
Inoc.-Ce+S+O	70 - 76	0,8 – 1,2	0,8 – 1,2						1,5 – 2	1
Inoc.-Ce	70 - 76	0,8 – 1,2	0,8 – 1,2						1,5 - 2	

The treatment addition to each ladle as well as the treatment temperature, are presented in **Table 30**. The calculation for the treatment alloys addition was made by the process control software Navigator from OCC, in order to keep the melt quality after treatment constant. The system has a process control model that takes in account the last treatment results and the actual targets, to calculate the optimized alloys additions.

Table 30 - Ladle treatment temperature and treatment addition for the trials for inoculant evaluation.

Ladle number	Treatment temperature (^{o}C)	Nodularizer added (m)	Inoculant added (m)
1	1447	36,5	16,7
2	1445	35	17,7
3	1451	36,5	17,6
4	1445	37	18,2
5	1438	38,5	19
6	1443	40	19,1
7	1447	41,9	17,8
8	1457	43,5	21
9	1416	36	15,8
10	1442	34	18,1

The chemical composition of each ladle after treatment, at the time the samples for the thermal analysis system were made is presented in **Table 31**.

Table 31 - Chemical composition from the melt after each treatment, from the inoculation trials.

Ladle number	C* [%]	Si [%]	Mn [%]	P [%]	S [%]	Cr [%]	Al [%]	Cu [%]	Mg [%]
1	3,66	1,96	0,31	0,009	0,012	0,03	0,007	0,50	0,049
2	3,66	1,98	0,31	0,010	0,014	0,03	0,006	0,50	0,039
3	3,65	2,03	0,31	0,009	0,013	0,03	0,007	0,50	0,045
4	3,64	2,05	0,31	0,009	0,013	0,03	0,007	0,50	0,043
5	3,61	2,04	0,31	0,011	0,013	0,03	0,007	0,51	0,043
6	3,62	2,03	0,30	0,013	0,012	0,03	0,007	0,51	0,039
7	3,56	2,04	0,30	0,013	0,013	0,03	0,008	0,50	0,048
8	3,58	2,06	0,30	0,014	0,012	0,03	0,008	0,50	0,045
9	3,61	1,97	0,29	0,016	0,012	0,02	0,007	0,51	0,045
10	3,59	1,99	0,28	0,019	0,013	0,02	0,007	0,51	0,041

* - The Carbon content presented in the table above is not prevenient from the LECO analyzer, and so a higher uncertainty can be associated to that measurement values.

The **Figure 100** shows the variation of the undercooling for all 10 ladles after treatment, measured by the thermal analysis cup without any inoculant inside, representing therefore the ground melt inoculation state after treatment. The undercooling changed between 11 and 14°C.

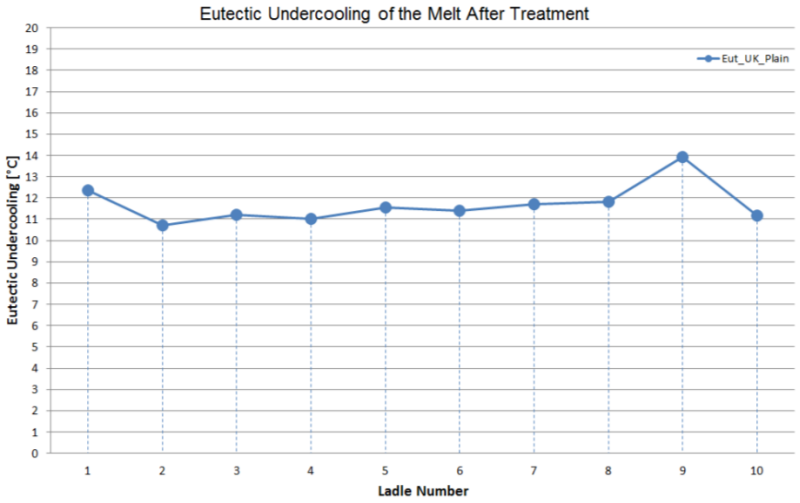

Figure 100 - Variation of the eutectic undercooling measured by the thermal analysis cup AccuVo plain, after each treatment, for the inoculation trials.

From all thermal analysis samples for the different treated melts, a metallographic evaluation of the graphite particle shape, size and distribution was made, through the acquisition of 25 micrographs per sample that were evaluated by the image analysis software Micr-O-Phase.

The average values for the main graphite particle parameters for the 10 melts tested for each type of inoculant are presented below. **Figure 101** shows the average nodularity value revealing that the addition of inoculant after the ladle treatment (that included already a pre-conditioning step of inoculation) improved slightly the nodularity.

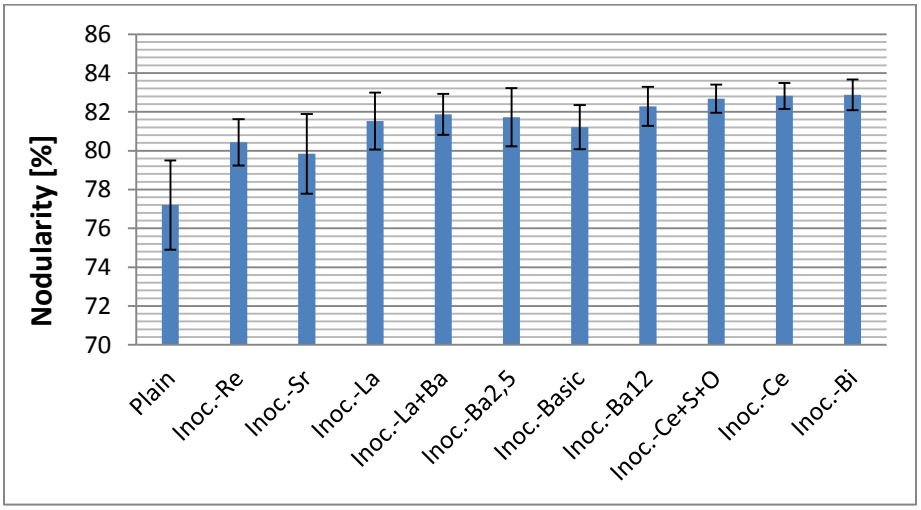

Figure 101 – Average nodularity value per inoculant, from the samples used in the inoculation test.

The influence, of each of the inoculant types used, on the graphite particle density and graphite particle size is presented in **Figure 102**. From the figures it is visible that as the particle density increases the size of the graphite particles decrease as expected. The melt state after treatment, only with the pre-conditioning from the inoculant wire, (identified as plain in the graphic from **Figure 102**, with no addition of inoculant in the AccuVo®-cup chamber 1) shows the lowest particle density from all samples analysed.

On the opposite, the addition of inoculants containing Bismuth gave the highest particle density (58% more particles than the plain sample) and highest amount of small graphite particles by increasing the size 8 particles from 4,6% to 10,4% and the size 7 particles from 40% to 73%. Very similar results were also obtained for inoculants containing Cerium (Inoc.-Ce) and Cerium+Sulfur+Oxygen (Inoc.-Ce+S+O), having also a strong influence in increasing the inoculation potential. Curiously, the use of the inoculant containing Rare-Earth (Inoc.-RE) has a very low influence on the inoculation compared to the sample only with pre-conditioning (3% increase in particle density and 3% less size 8 particles).

Inoculants bearing Barium showed a moderate influence on the inoculation. Nevertheless the increase on the Barium content in the inoculant, improves the final inoculation potential. The inoculant with 12% of Barium (Inoc.-Ba12) gave higher particle density and higher amount of smaller particles when compared with inoculants with less Barium (Inoc.-Ba2,5). All other inoculants used resulted in an intermediate effect.

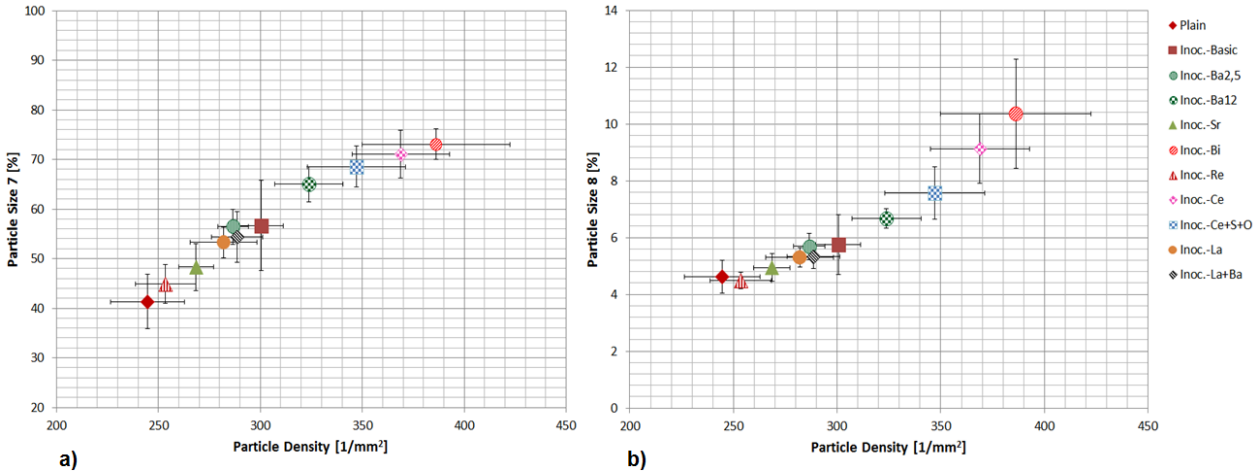

Figure 102 - Evaluation of the effect of different inoculants on the graphite particle density and percentage of smaller particle size. a) Particle size 7; b) Particle size 8.

Once the quality of the inoculation of a nodular graphite cast iron melt is substantially measured by the number of graphite particles and the size of those particles, it is necessary to express this using a single value or variable. Therefore an "*Inoculant Index*" was created to allow an easy evaluation of the melt's inoculation state. This *Inoculant Index* was calculated based on the microstructure evaluation of the samples considering the following parameters:

- Graphite Particle Density [1/mm2]
- Graphite Particle Size Distribution [%]

To achieve an index, that represents the inoculation potential of the melt, the **Equation 12** was developed.

$$Inoculant\_Index = \frac{ParticleDensity}{100} + 0.51 \times Size\_Distribution\_Factor \quad \textbf{(Eq. 12)}$$

were "Particle_Density" is the measured graphite particle density per square millimetres and "Size_Distribution_Factor" is a parameter that ranges from 0 to 10 and is determined based on the graphite particle size distributions in percentage and a qualitative constant defined by an metallographic technician.

This "Size_Distribution_Factor" is higher (closer to 10) when the microstructure represents a good inoculated microstructure and gets smaller (closer to 0) when the microstructure shows evidences of poor inoculation.

The new classification of the melt inoculation quality, according to the new *Inoculant Index*, for the addition of the different inoculants, is presented in **Figure 103**.

The highest *Inoculant Index* was obtained for the Inoc.-Bi inoculant, trailed by the Inoc.-Ce and Inoc.-Ce+S+O, in accordance to the results provided before in the **Figure 102**. The lowest *Inoculant Index* (lowest inoculation state) was obtained for the plain sample (without late inoculation additions) and the Inoc.-Re.

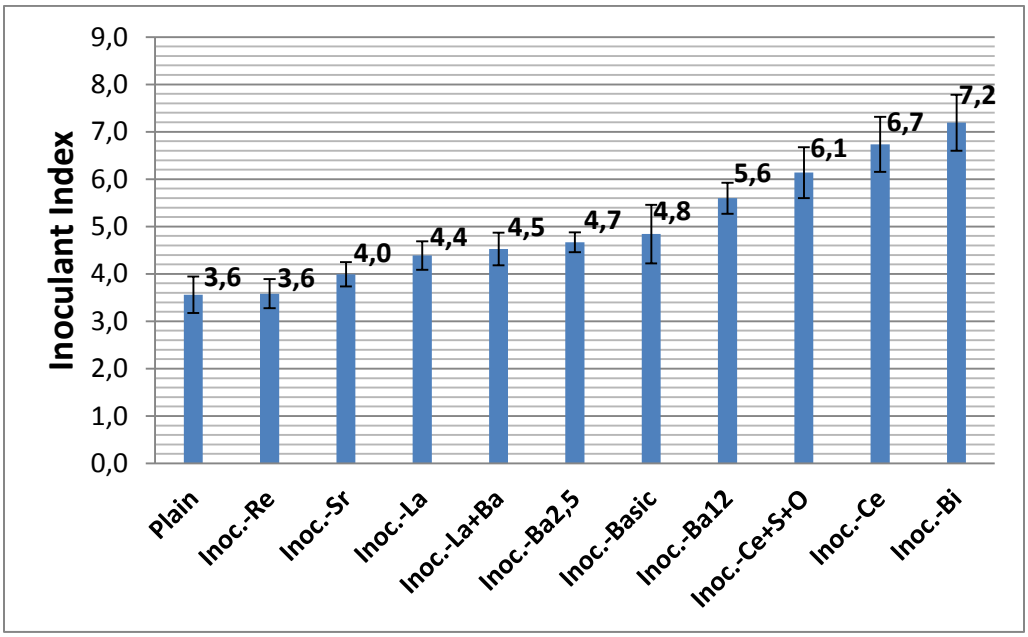

Figure 103 - Classification of the melt's inoculation quality according to the Inoculant Index for the different inoculants tested.

Once the use of different inoculants results in different inoculation states of the melt, it is expected that changes in the solidification's kinetic and consequently in the solidification morphology are visible in the solidification curve. Such effect is visible on the **Figure 104**, where, as the *Inoculant Index* on the melt increases due to the use of more powerful inoculants, the solidification morphology changes progressively from hypoeutectic with high undercooling (Eut_UK = 12°C) to eutectic. The same figure also shows that, as the inoculation potential in the melt increases, for the different inoculant additions, the undercooling is progressively reduced and therefore the temperature difference between the liquidus and the eutectic low temperature is also reduced. Once the eutectic low temperature equals the liquidus temperature, the solidification morphology of the curve changes and goes from hypoeutectic to eutectic.

The correlation between all samples evaluated in this trials and the solidification curves shows that the inoculation potential of the melt has a correlation coefficient (R^2) of 0,86 with the eutectic low temperature and it is therefore the point that better represents that quality state of the melt (see **Figure 105**).

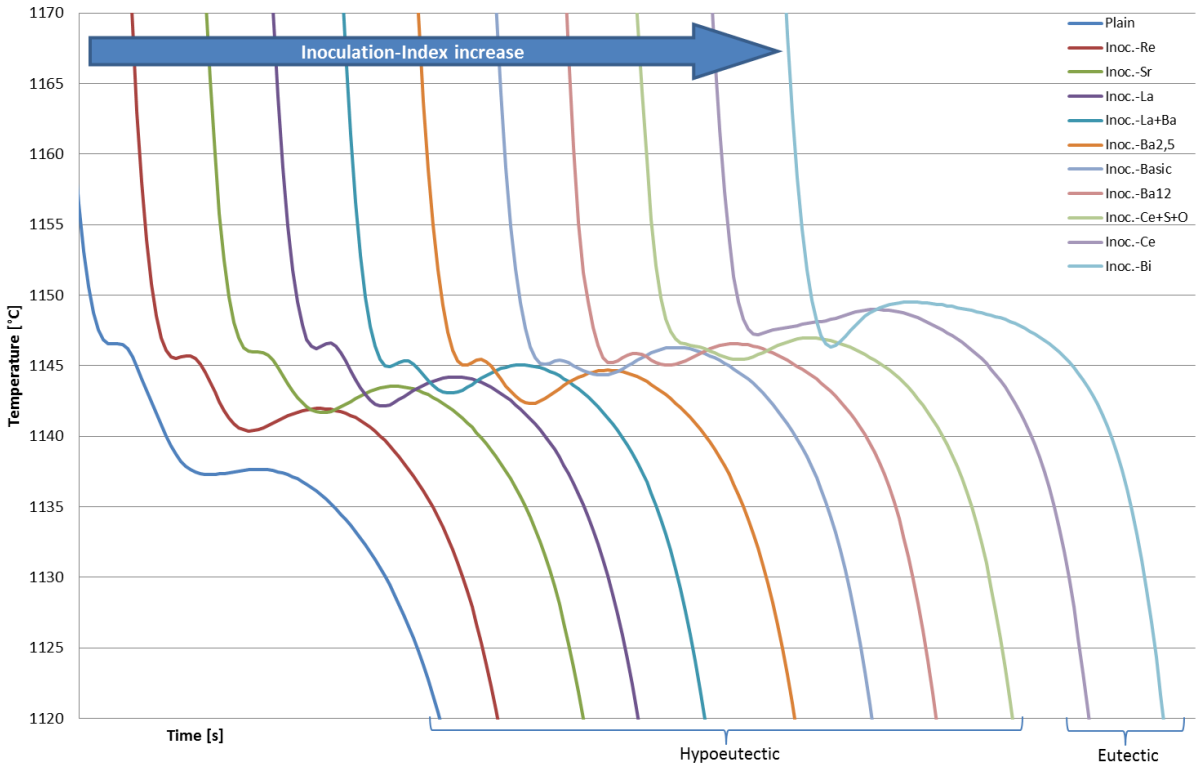

Figure 104 - Representative curves (all from ladle number 3) showing the influence of the different inoculants on the solidification morphology.

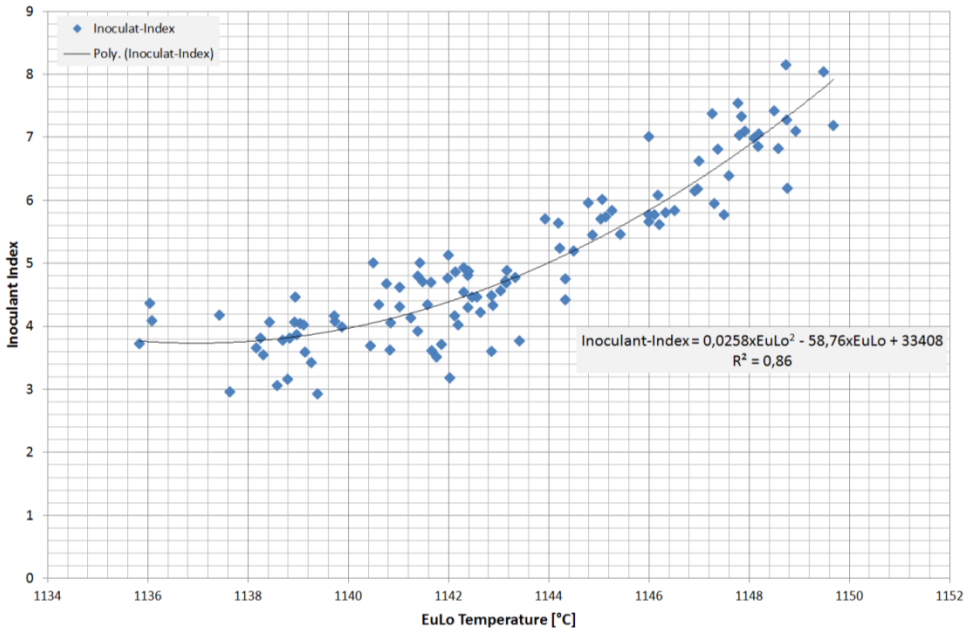

Figure 105 - Correlation between the Inoculant Index and the eutectic low temperature.

5.5. Influence of liquidus temperature on shrinkage and porosity defects in hypoeutectic solidification morphologies

In order to study the influence of liquidus temperature in the formation of shrinkage and porosity defects on a test casting for hypoeutectic solidification morphology melts, the following trial was performed.

The trials were executed in industrial conditions at a foundry, using a test model plate from that same foundry, were the test part from **Figure 65** was incorporated. No additional feeder was used in the model. The drawing of the model tree used in the trials is presented in **Figure 106** and although other models were in the same tree, in these trials only the test casting developed in this work (presented in chapter 4.2.1) was used. The melt feeding to the casting was made through the section 1. The model was then used on a horizontal moulding line to create the moulds poured during the trial. The moulds were made of green sand.

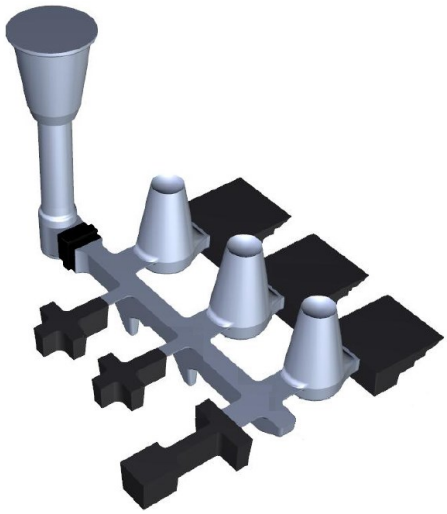

Figure 106 - Drawing of the tree model used in the liquidus temperature trials.

The trials matrix, presented in **Table 32**, considers variations on the liquidus temperature of the melt, keeping the solidification morphology of the melt hypoeutectic. The variation of the liquidus temperature was a result of the use of two different base iron melts with different carbon contents. The trials considered also a variation on the levels of pre-inoculation in order to evaluate the sensibility of the melt's *Inoculant Index*, on the curve morphology and final defects in the casting.

Table 32 - Trials matrix for the evaluation of shrinkage and porosity defects in hypoeutectic solidification morphology melts.

Ladle number	Target liquidus temperature (°C)	Pre-conditioning inoculant (m)	Stream inoculant (addition amount 0,05%)
LT_1	1170	Low	Inoc.-Basic
LT_2	1170	Normal	Inoc.-Basic
LT_9	1145	Normal	Inoc.-Basic
LT_12	1145	Low	Inoc.-Basic

The composition of the "Inoc.-Basic" is given in the **Table 29**.

The trials procedure is illustrated in **Figure 107**. The thermal analysis samples were taken at the beginning of pouring from each test casting. Only one type of thermal analysis AccuVo-cup was used, where the first chamber was empty and the second had the Inoc.-Basic. Together with the thermal analysis sample also a spectrometer sample was taken, for later evaluation of the chemical composition. The moulds poured were numbered with the same number as the ladle.

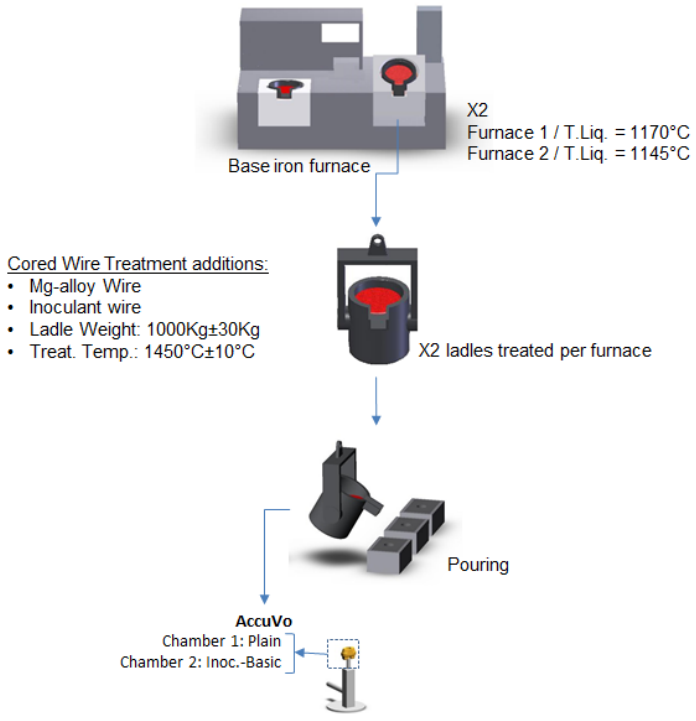

Figure 107 - Illustration of the trials procedure for evaluation of shrinkage and porosity in hypoeutectic morphology melts.

For the trials, two different base iron melts were used, with different carbon contents, and therefore different liquidus temperatures. The melt was prepared using middle-frequency electrical furnaces. The material grade was GJS 400.

The chemical composition of the base iron melt used is presented in the **Table 33**.

Table 33 - Base iron chemical composition for the shrinkage/porosity trials for different Liquid temperatures.

$C_{(Leco)}$ [%]	Si [%]	Mn [%]	P [%]	S [%]	Cu [%]	Sn [%]	Ni [%]	Cr [%]	Pb [%]
3,41	1,51	0,23	0,031	0,014	0,024	0,004	0,019	0,021	0,001
3,72	1,47	0,25	0,027	0,014	0,17	0,003	0,016	0,020	0,001

The treatment alloys used in this trial are presented in **Table 34**.

Table 34 - Treatment wires composition used in the shrinkage/porosity trials for different Liquid temperatures.

	Si (g/m)	Ca (g/m)	Mg (g/m)	Ba (g/m)	Al (g/m)	RE (g/m)	C (g/m)
Nodularizer	100	5	55	-	-	1,5	24
Pre-Conditioning inoculant	110	4,0	-	20	4,0	-	-

The process data referring to the treatment and pouring steps are summarized in **Table 35**.

Table 35 - Main process data from the treatment and pouring steps in the shrinkage/porosity trials for different Liquid temperatures..

Ladle number	Treated melt weight [Kg]	Treatment temperature (°C)	Nodularizer added (m)	Pre-conditioning inoculant (m)	Pouring temperature [°C]
LT_1	1000	1445	20	6	1352
LT_2	1000	1453	21	3	1373
LT_9	1000	1450	21	8	1368
LT_12	1005	1453	21	2	1371

The chemical compositions from the melt after treatment are presented in **Table 36**.

Table 36 - Chemical analysis results from the melt after treatment, from the shrinkage/porosity trials for different Liquid temperatures.

Ladle number	C* [%]	Si [%]	Mn [%]	P [%]	S [%]	Cr [%]	Al [%]	Cu [%]	Mg [%]
LT_1	3,49	2,33	0,23	0,031	0,010	0,022	0,003	0,024	0,031
LT_2	3,52	2,15	0,23	0,031	0,010	0,022	0,005	0,024	0,037
LT_9	3,71	2,20	0,27	0,032	0,011	0,021	0,004	0,016	0,040
LT_12	3,71	2,10	0,26	0,032	0,009	0,020	0,003	0,014	0,041

* - The Carbon content presented in the table above is not prevenient from the LECO analyzer, and so a higher uncertainty can be associated to that measurement values.

The variation of the liquidus temperature and the *Inoculant Index* during the trials is presented in **Figure 108**, showing that the liquidus temperature measured by thermal analysis from the treated melt decreased from the first to the second furnace. The dispersion of the *Inoculant Index* obtained during trials was approximately the same in the ladles treated from the first and second furnace and varied from 3 up to 7. The thermal analysis curve considered for the results displayed in the **Figure 108** are the one from the AccuVo-cup chamber that had the same inoculant as the inoculant used in the stream when pouring the casting. This way the thermal analysis curve considered is close to the real melt condition of the castings poured.

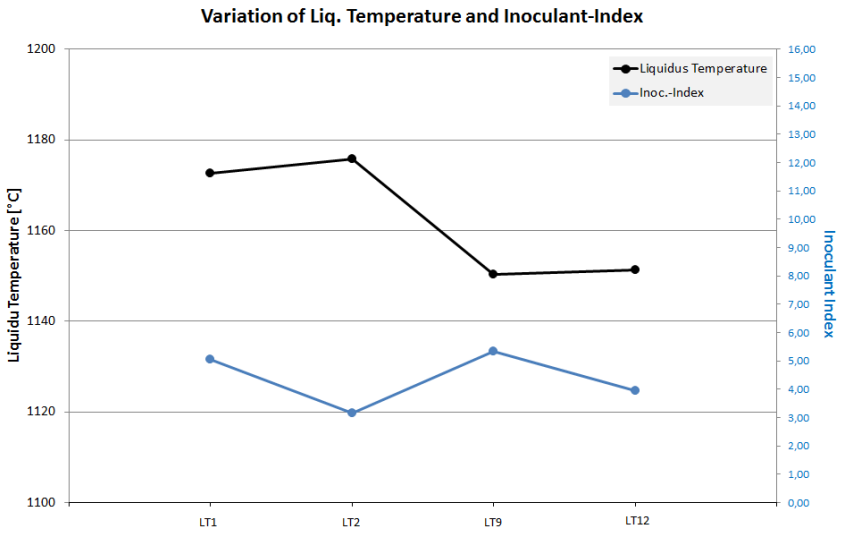

Figure 108 - Variation of the liquidus temperature and Inoculant Index during the execution of the shrinkage/porosity trials for different Liquid temperatures..

After the trials, the castings were recovered and taken to the laboratory for analysis. The evaluation of the shrinkage and porosity defects followed the evaluation mentioned in chapter 4.3.4. The results obtained are presented in **Table 37**. The table shows that open shrinkage was only seen once in test casting section 1 for a poured melt with highest liquidus temperature. For low liquidus temperature no open shrinkage defect was found in any of the castings sections. Also, no test casting section for any of the melts revealed porosity defects. Section 2 of the casting revealed no defects of any nature.

Table 37 - Shrinkage and porosity evaluation results for the shrinkage/porosity trials for different Liquid temperatures.

	Open shrinkage Vol.			Shrinkage vol.			Porosity Index		
Ladle number	**S1 (mm^3)**	**S2 (mm^3)**	**S3 (mm^3)**	**S1 (mm^3)**	**S2 (mm^3)**	**S3 (mm^3)**	**S1**	**S2**	**S3**
LT_1	0	0	0	0	0	3600	0	0	0
LT_2	2000	0	0	0	0	2350	0	0	0
LT_9	0	0	0	500	0	0	0	0	0
LT_12	0	0	0	250	0	0	0	0	0

The evaluation of the results obtained for section 1, also presented in **Figure 109**, shows that for high liquidus temperatures, bigger shrinkage is present in the casting. The exception was the casting LT_1 that had a lower pouring temperature compared to the other castings might have

helped to avoid the shrinkage in section 1. For results from section 1 with low liquidus temperature, shrinkage is always present and it seems even to increase if the *Inoculant Index* increases (case of LT_12). This indicates that the higher potential for precipitation of graphite causes an increase of the shrinkage cavity, possibly due to excess pressure on the mould walls causing its deformation and therefore the increase in shrinkage volume. Nevertheless no prove of this possible mould deformation is here given, and this fact is purely conjectural.

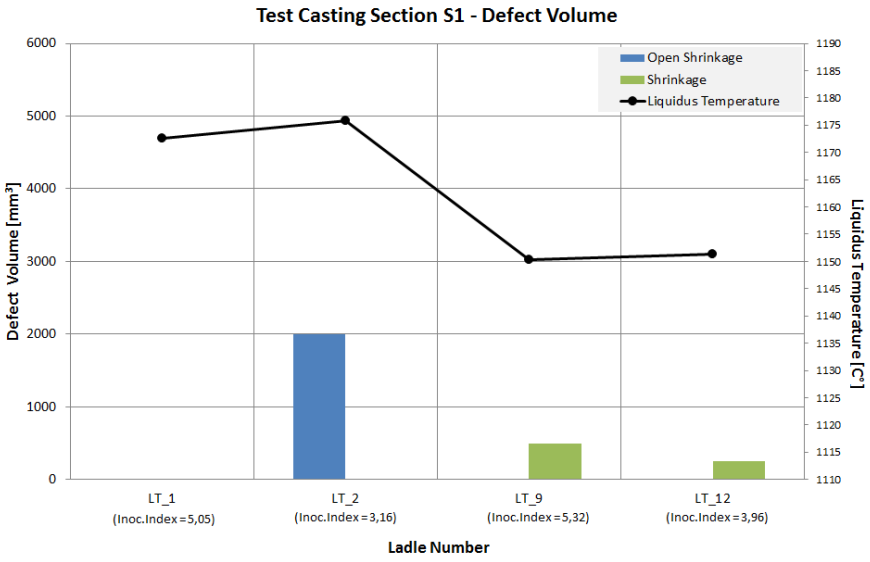

Figure 109 - Volume defect from test casting section 1, for the shrinkage/porosity trials for different Liquid temperatures.

For the results obtained in section 3, only shrinkage defects were found in the castings poured with high liquidus temperature. For lower liquidus temperatures no open shrinkage or shrinkage was found in these castings section (see **Figure 110**). The observation of the influence of the *Inoculant Index* reveals here also that the casting poured from the melt with the higher *Inoculant Index* had the higher shrinkage volume. The same hypotheses as formulated for the casting's section 1, regarding the possible mould wall movement for high *Inoculant Index*, might be applicable here to explain with the shrinkage is bigger for better inoculated melts.

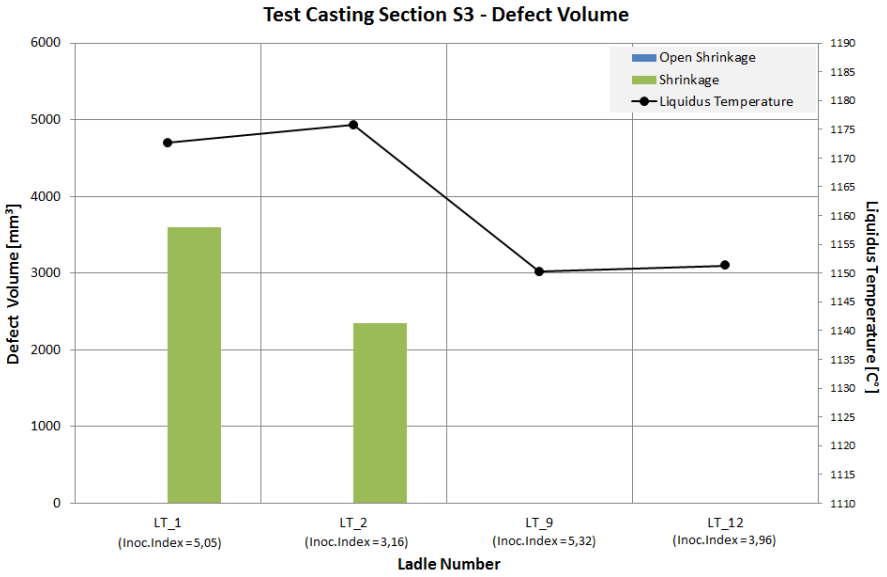

Figure 110 - Volume defect from test casting section 3, from the feeding needs trials for different Liquid temperatures.

In order to have a better understanding on the effect of the liquidus temperature on the microstructure of the casting, especially in the solidification structure of austenite, two samples, one from high liquidus temperature and another from low liquidus temperature, were evaluated in the laboratory with application of colour etching. The samples from section 3 from castings LT_1 and LT_9 were submitted to the analysis.

The graphite structure of the two casting's samples analysed is presented in the micrographs from **Figure 111**. The samples appear to have a similar structure, but due to the difference in the liquidus temperature, the LT_9 sample presents a slightly higher amount of graphite phase than the LT_1 sample, as presented in **Table 38**.

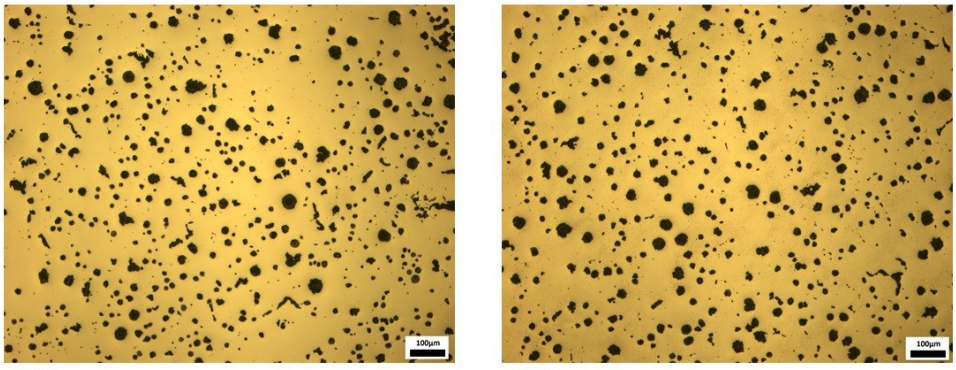

Figure 111 - Micrographs without etching from the casting's samples LT_1 and LT_9.

Table 38 - Main metallographic results from the micrographs from Figure 111.

	LT_1	LT_9
Nodularity [%]	73	82
Phase Area of Graphite [%]	8,1	9,3
Graphite particle density [1/mm^2]	266	295

The drop in the liquidus temperature from the melt used for pouring the casting LT_1 to the melt used for casting LT_9, was made due to the increase of carbon between the two base iron melts used (see **Table 33**). This increase in carbon in the melt, caused the percentage of graphite in the microstructure to increase from 8,1% to 9,3%. Once the test casting has a total volume of 427.625mm^3, this increase of carbon corresponded to a increase in graphite volume of 3.421mm^3. Once the total volume contraction on test casting LT_1 was 3.600mm^3 and on casting LT_2 was in total 4.350mm^3, the increase of carbon almost compensated all of the shrinkage volume in section 3. Nevertheless, it would not be enough to completely solve the open shrinkage and shrinkage defects at those sections, so other parameters might have change with the reduction of the liquidus temperature. One of those possible changes might be the dendritic structure that is formed during solidification.

To better understand the microstructure revealed by the colour etching, the AccuVo®-cup sample from test LT_1 was submitted to a SEM[15] analysis, in order to determine the solidification sequence of the phases coloured by the etching and validate the method before applying it to the casting's samples. The definition of the solidification sequence is made through the evaluation of the segregation of the Si and Mn in the different regions. It was presented previously, in **Table 3**, that Si concentrates in the austenite and Mn segregates to the liquid. Therefore it is expected that the austenite crystals that solidified first have a high presence of Si and low Mn and the austenite that solidified later has lower presence of Si and higher of Mn. Therefore, low Mn/Si ratio will correspond to areas that solidified earlier and high Mn/Si ratios to areas that solidified later.

Figure 112a shows the micrograph from the AccuVo®-cup sample LT_1 after application of the colour etching and **Figure 112b** the detail of the area where the SEM analysis was performed. Four different areas were marked, in region of the microstructure that are distinct, such as the

[15] SEM – Scanning Electron Microscope

area around the nodule (1 in **Figure 112b**), the different areas belonging probably to a dendrite arm (2 and 3 in **Figure 112b**) and one at the intercellular brown area (4 in **Figure 112b**). In **Figure 112b** is also identified the presence of the nodules and micro-hardness indentation used to mark the spot where the analysis should be made, once the etching has to be removed before the SEM analysis.

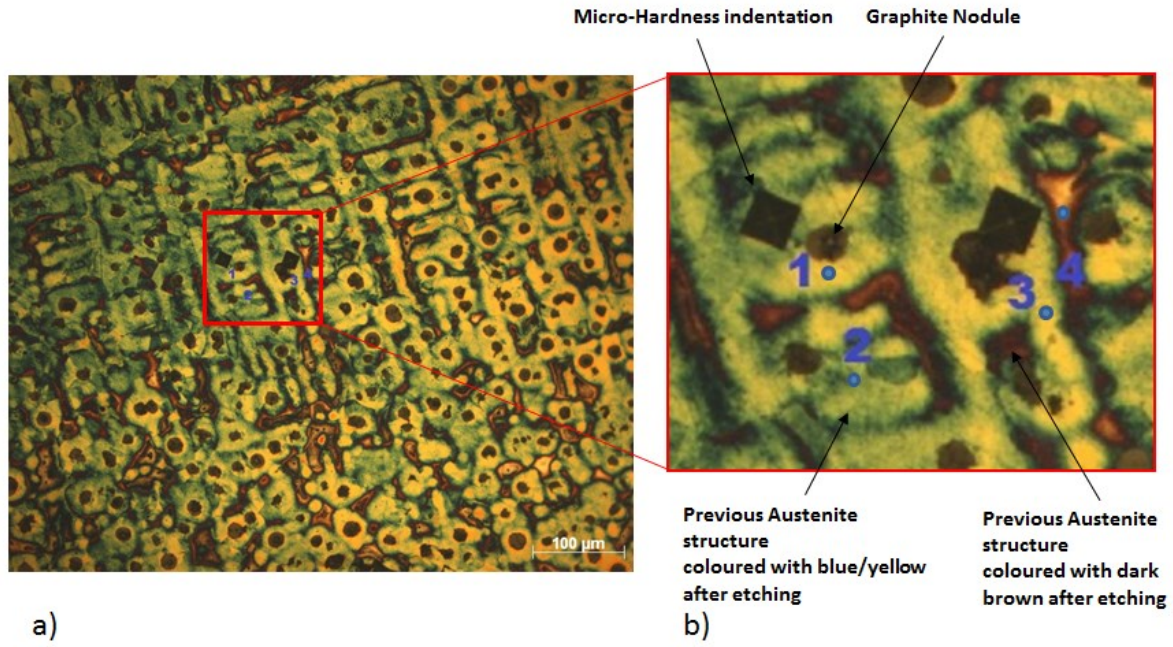

Figure 112 - Micrograph from AccuVo® sample LT_1 after colour etching with reagent 1 from Table 14 for 15 minutes; b) detail of the area where the SEM analysis was performed (marked by the points near the numbers).

The results from the SEM analysis, in the form of Mn/Si ration, are presented in the **Table 39**. The results indicate that the blue/yellow areas (point 1, 2 and 3 from **Figure 112b**) correspond to the first austenite structure to solidify. No relevant differentiation is visible at the image or by the SEM results to distinguish between the blue/yellow area around the nodule and the blue/yellow area that belongs to a dendrite arm. It is then considered that no distinguishes can be made between the primary austenite (dendritic structure) and eutectic austenite (smaller dendrites and hallo around the nodules) based on the microstructures segregation profiles. The brown intercellular area (point 4 in **Figure 112b**), is the one with the highest Mn/Si ration, corresponding therefore to the last region to solidify.

Table 39 - Relation Mn/Si, after evaluation of the sample by SEM, to determine the relative solidification order of the different coloured areas by colour etching.

	Point 1 Close to graphite nodule	Point 2 Dendrite arm	Point 3 Dendrite arm	Point 4 Intercellular region
Mn/Si	0,15	0,16	0,17	0,25

A micrograph from the test casting LT_1 in section 3, showing the phase identified in the structure after colour etching is presented in **Figure 113**. In the micrograph, dendrites and hallows surrounding the nodules appear with the same colour and are distinguishable only by the shape. The last freezing zones appear in darker orange colour.

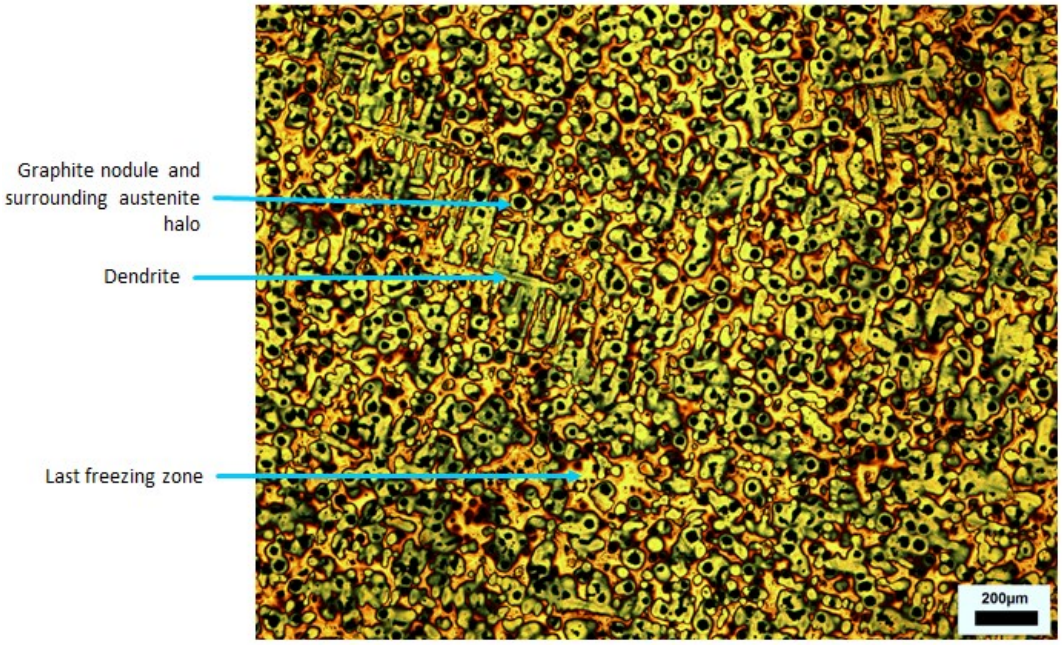

Figure 113 - Micrograph from test casting's LT_1 section 3, after color etching with reagent no.1 during 15 minutes.

The observation and qualitative comparison of the microstructures from sample LT_1 and LT_9 are presented in **Figure 114**, after application of colour etching reagent number 1 (from **Table 14**) for a time period of 15 minutes. From observation of the micrographs, the sample LT_1 presents more dendrites than sample LT_9. Although in the image only parts of the dendrites are visible, due to the fact that a dendrite is a 3 dimensional structure and the image is observed in only 2 dimensions, on sample LT_1 the presence of the dendrites is more easily recognizable, as a long

ramified branched phase morphology (**Figure 114a** and **b**). On sample LT_9, this long ramified phase morphology is not visible, and only short straight branched of a possible dendrite are recognizable (**Figure 114 d**).

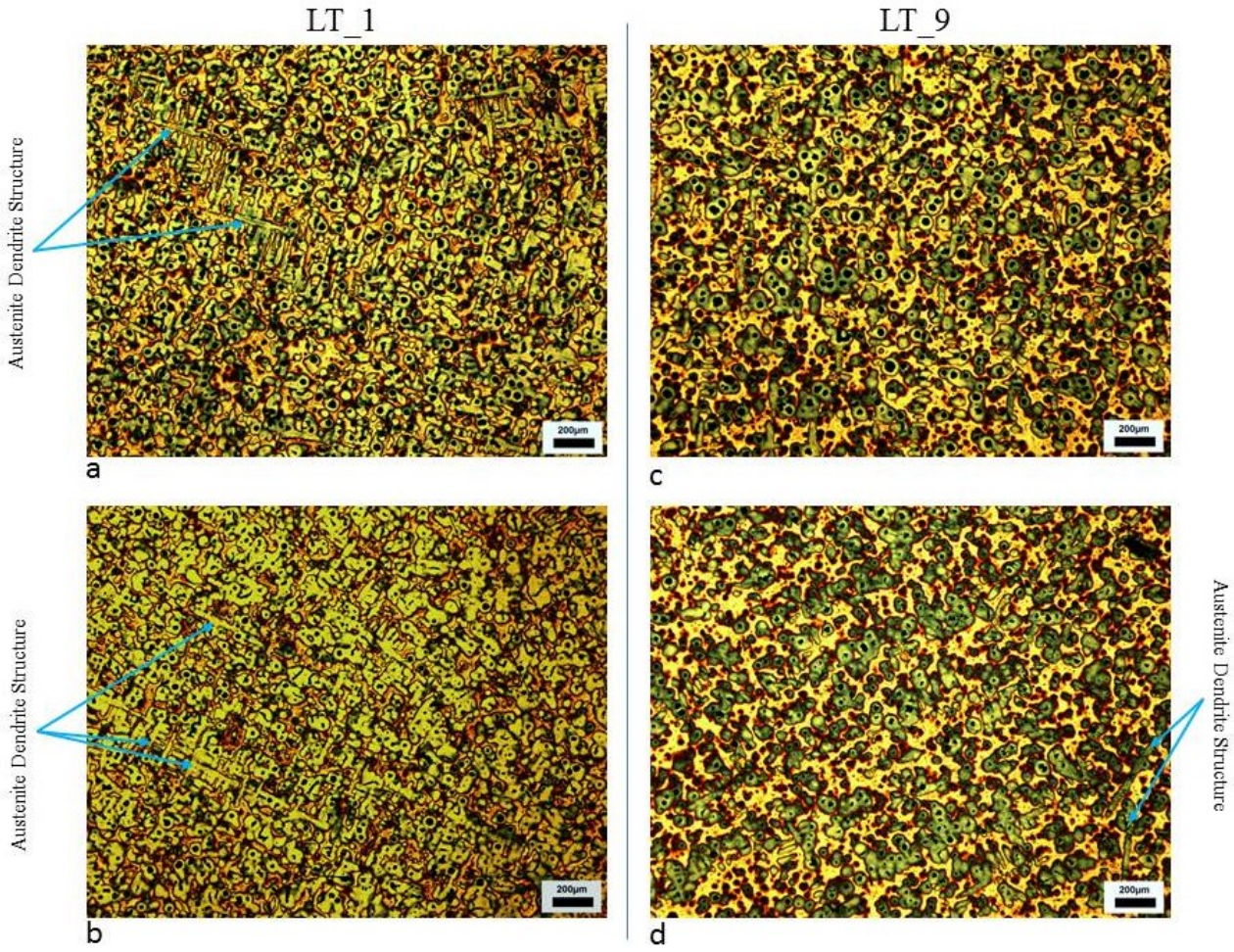

Figure 114 - Micrographs of the samples from section 3 from test casting number LT_1 and LT_9, after colour etching with reagent No.1 (Table 14) for 15 minutes.

In order to enhance the differences between the two microstructures and allow a better visualization of the dendritic structure, the same samples were subjected to a longer etching period. Therefore, the samples were further etched for 20 minutes, again with reagent number 1. The longer etching time caused the dendritic structure and the austenite hallows surrounding the nodules to be coloured with an intense green colour while the interdendritic regions are coloured with orange, as presented in **Figure 115a** and **c**. From the **Figure 115a** it is already visible the shape and length of some of the dendrite arms from the structure (intense green colour), that

where austenite when the sample solidified. To further enhance the visualization of the dendritic structure, the images from **Figure 115a** and **c**, were manipulated using the software InkScape, to isolate the intense green colour. To do so, the images were imported to the InkScape software, and a *vectorization*[16] (image tracing) algorithm was applied to create several graphic layers of the image according to the different colour in the original image. The vector graphic layers that did not correspond to the green colour were deleted and only the ones that were green were used. The result from this image manipulation is presented in **Figure 115b** and **d**, respectively from the etched images from **Figure 115a** and **c**. The images revealed by **Figure 115b** and d, presents with more clarity the differences in the dendritic structure from a sample with high liquidus (sample LT_1) temperature from one with lower liquidus temperature (sample LT_9). The sample with high liquidus temperature has a denser and longer dendrite arms structure compared to the one with lower liquidus temperature.

The existence of a highly ramified dendritic structure is indicated by the literature, previously presented in this work, as having a negative influence in the process of melt feeding to the casting. Once the samples observed were taken from the test casting's section 3, where for high liquidus temperature there was a high shrinkage volume, the dendritic size and complexity might have influence negatively the feeding of that section. For low liquidus temperature, where the dendritic structure is also smaller and less dense, no shrinkage defect was found.

The fact that the micrographs presented above reveal differences in the dendritic structure between samples with high and low liquidus temperature, there must be a noticeable influence on this on the solidification curve.

[16] In computer graphics, ***vectorization*** is the conversion of raster graphics into vector graphics.

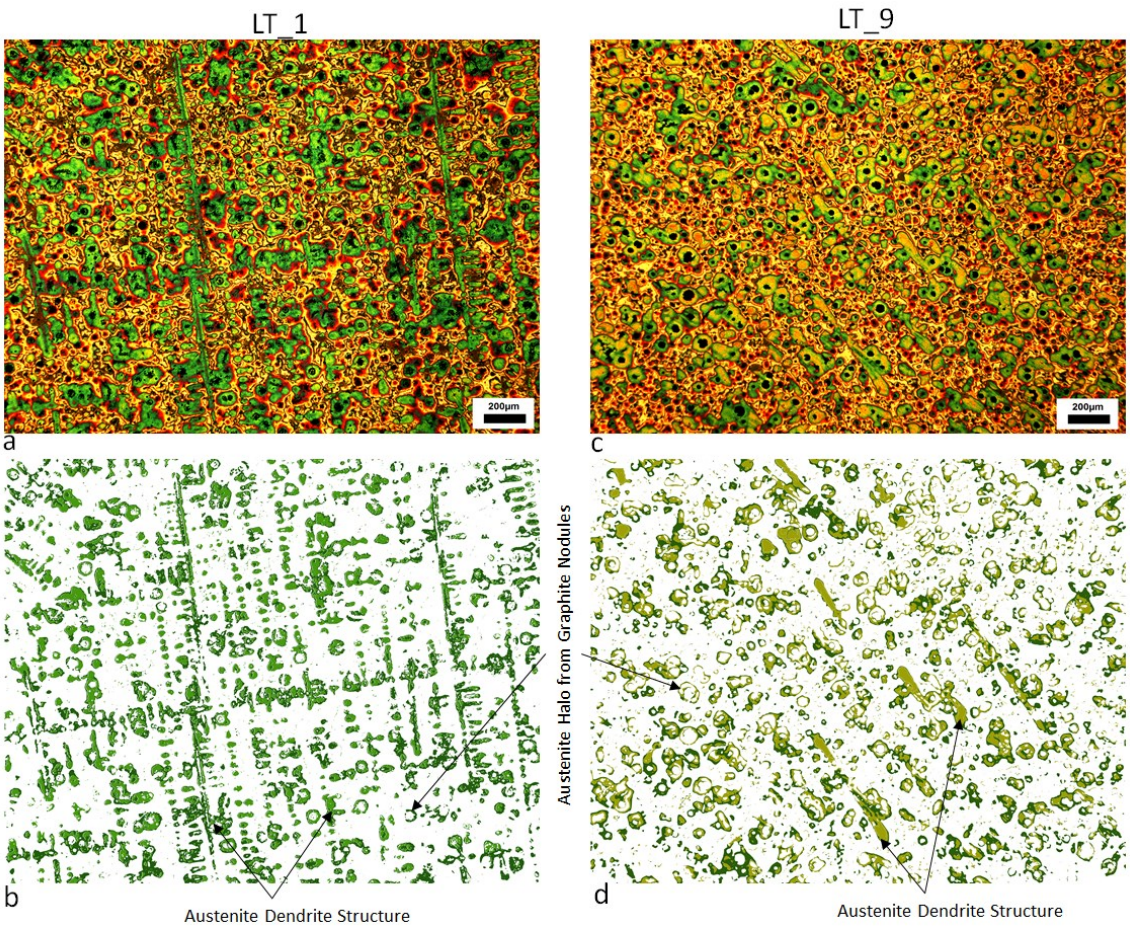

Figure 115 - Micrographs of the samples from section 3 from test casting number LT_1 and LT_9. a) and c) after colour etching with reagent No.1 (table 13) for 35minutes; b) and d) after vectorization and isolation of the green coloured areas.

All solidification curves from this test are presented in **Figure 116**, with identification of the main points, including the dendritic coherency point. Once the dendritic coherency point represents the moment until when the structure (dendrites specially) previously grows freely in the melt, it is understandable that the evaluation of the solidification curve from the start of solidification (liquidus temperature) until the DCP is important to estimate the characteristics of the dendritic structure. Therefore, variables like the temperature and time difference between the liquidus temperature and the DCP (DCP(ΔT) and DCP(Δt) respectively) and the cooling rate at the DCP point were evaluated. The values are presented in **Table 40**.

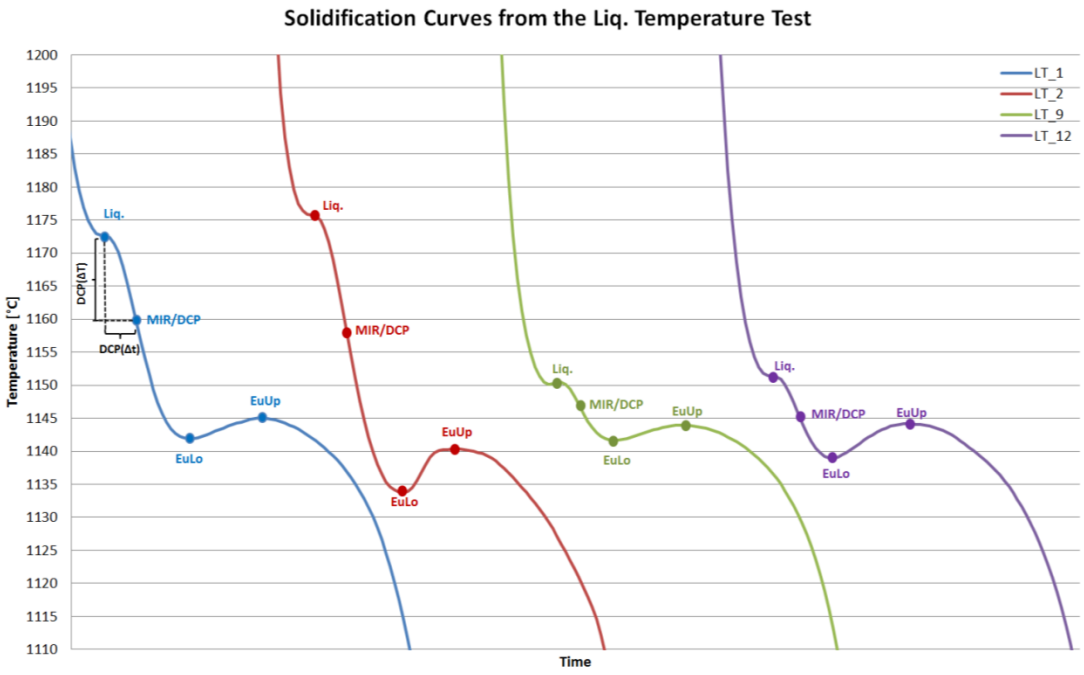

Figure 116 - Solidification curves from the liquidus temperature trials for hypoeutectic morphologies.

Table 40 - Table with the main characteristic points of the dendritic coherency point, taken from the solidification curve.

	LT_1	LT_2	LT_3	LT_4
DCP(ΔT) [°C]	13,0	17,4	3,1	5,5
DCP(Δt) [s]	7	8	6	6
DCP_(-dT/dt) [°C/s]	2,9	3,7	1,4	1,6

The evaluation of the data from **Table 40**, as well as the observation of the solidification curves from **Figure 116**, shows that although there is a significant change in the liquidus temperature between the two melts (approximately 25°C) the time of occurrence of the dendritic coherency point did not change significantly (approximately 1,5s), indicating that the time of occurrence of the DCP after beginning of solidification is not the main point to estimate the characteristic of the dendritic structure. The biggest variation is the temperature decrease that occurs in the 6 to 7 seconds from the liquidus temperature until the DPC, or in other words, the cooling rate at the DCP point. For high liquidus temperatures, the cooling rate of the melt at the DCP point more than doubles in comparison with melts with low liquidus temperature. The higher cooling rate caused the dendritic structure to develop more rapidly, resulting in a bigger and more heavily ramified structure than the ones from a melt with lower cooling rate (lower liquidus temperature).

5.6. Influence of the solidification morphology of the melt, measured by thermal analysis, on the feeding necessities

The following experiment, executed in foundry conditions, had the main objective to study the influence of the melt solidification morphology, on the feeding necessities of the melt. Once again, the solidification morphology type was determined through the use of thermal analysis rather than the traditional use of C.E. value.

For the trials, the test casting presented in the 4.2.1 was used, and a small model plate was created, to produce the moulds presented in **Figure 117**. The moulds were produced using resin bounded sand.

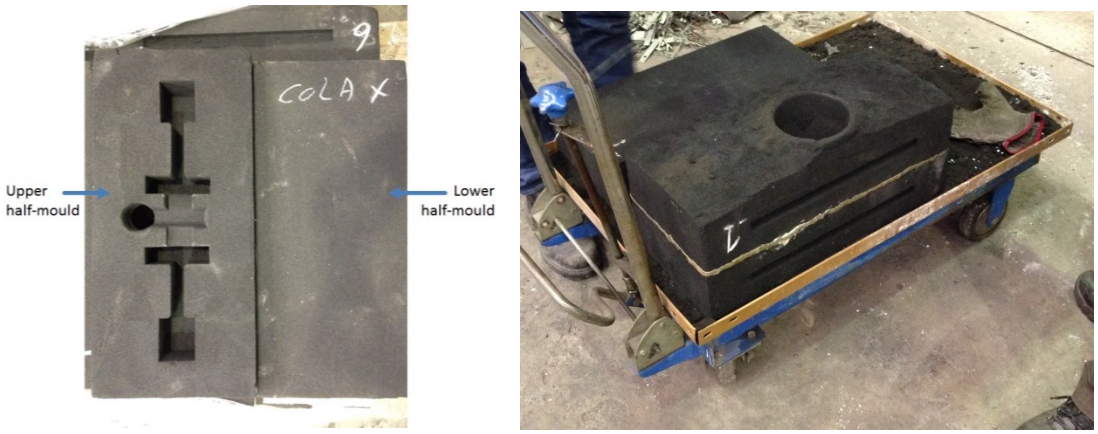

Figure 117 - Sand mould used in the solidification morphology trials to evaluate melt's feeding needs.

The trial was executed during normal production, on a foundry that produces nodular graphite cast iron. The foundry uses middle frequency electrical furnaces to melt, Sandwich method for treatment and pouring is performed directly from the treatment ladle into the moulds of a horizontal moulding line. The test performed did not use the horizontal moulding line, and the test moulds were placed at a car close to the pouring line.

Tests from three different base iron melts were made in order to achieve the desirable distribution of melt solidification morphologies. The melt was GJS400, prepared in middle-frequency

electrical furnaces, using a charge composed by low Mn steel scrap, returns, SiC, FeSi and graphite. The chemical compositions of the melts used are presented in **Table 41**.

Table 41 - Chemical composition from the base iron used on the trials to evaluation the impact of the melt's feeding needs.

Base iron nr.	C* [%]	Si [%]	Mn [%]	P [%]	S [%]	Cu [%]	Sn [%]	Ni [%]	Cr [%]	Pb [%]
1	**3,80**	1,82	0,41	0,013	0,005	0,026	0,011	0,063	0,032	0,002
2	**3,84**	1,76	0,40	0,015	0,006	0,022	0,009	0,063	0,037	0,002
3	**3,94**	2,07	0,42	0,012	0,006	0,036	0,012	0,065	0,031	0,002

* - The Carbon content presented in the table above is not prevenient from the LECO analyzer, and so a higher uncertainty can be associated to that measurement values.

The Sandwich treatment was performed using the alloys presented in **Table 42**.

Table 42 - Treatment alloys used for the sandwich treatment, on the trials to evaluation the impact of the melt's feeding needs.

	Si (wt%)	Ca (wt%)	Mg (wt%)	Ba (wt%)	Al (wt%)	RE (wt%)	Zr (wt%)	Mn (wt%)	Fe (wt%)
Nodularizer	44,6	1,19	6,2	-	0,64	0,64	-	-	balance
Inoculant	66,9	1,81	-	1,69	1,06	-	2,45	2,74	balance

The process data regarding the treatment of each ladle and pouring temperature are given in **Table 43**.

Table 43 - Treatment and pouring process data from the trials to evaluation the impact of the melt's feeding needs.

Ladle number	Base iron melt nr.	Treat. weight [Kg]	Tapping temp. [°C]	Nodularizer (% of treat weight)	Inoculant (% of treat weight)	Pouring temperature [°C]
DC_1	1	1162	1439	1,29	0,46	1364
DC_2	1	1080	1438	1,39	0,49	1380
DC_3	1	1040	1451	1,54	0,46	1377
DC_4	1	1000	1450	1,50	0,53	1370
DC_5	2	1100	1437	1,45	0,38	1380
DC_6	2	986	1438	1,52	0,54	1369
DC_7	3	1036	1437	1,45	0,41	1382
DC_8	3	1046	1435	1,43	0,40	1364
DC_9	3	1000	1437	1,5	0,42	1378

After treatment of each ladle, a thermal analysis sample and spectrometer sample was made from the melt. The results from the spectrometer samples are presented in **Table 44** . The thermal analysis curves are presented in **Figure 118** where they are ordered according to their solidification morphology, from the less hypoeutectic to the more hypereutectic, as if the C.E. value was always increasing.

Table 44 - Chemical composition from the melt after treatment for the trials to evaluation the impact of the melt's feeding needs.

Ladle number	C* [%]	Si [%]	Mn [%]	P [%]	S [%]	Cr [%]	Al [%]	Cu [%]	Mg [%]
DC_1	3,60	2,63	0,42	0,012	0,005	0,032	0,014	0,025	0,040
DC_2	3,56	2,7	0,42	0,012	0,005	0,032	0,014	0,024	0,043
DC_3	3,63	2,67	0,42	0,015	0,004	0,033	0,013	0,025	0,047
DC_4	3,54	2,68	0,42	0,013	0,005	0,032	0,015	0,025	0,046
DC_5	3,68	2,59	0,41	0,015	0,005	0,037	0,013	0,023	0,047
DC_6	3,70	2,54	0,42	0,015	0,005	0,038	0,014	0,024	0,043
DC_7	3,65	2,88	0,43	0,011	0,005	0,032	0,013	0,036	0,048
DC_8	3,56	2,89	0,42	0,010	0,004	0,032	0,011	0,036	0,053
DC_9	3,6	2,87	0,43	0,011	0,005	0,033	0,011	0,035	0,050

* - The Carbon content presented in the table above is not prevenient from the LECO analyzer, and so a higher uncertainty can be associated to that measurement values.

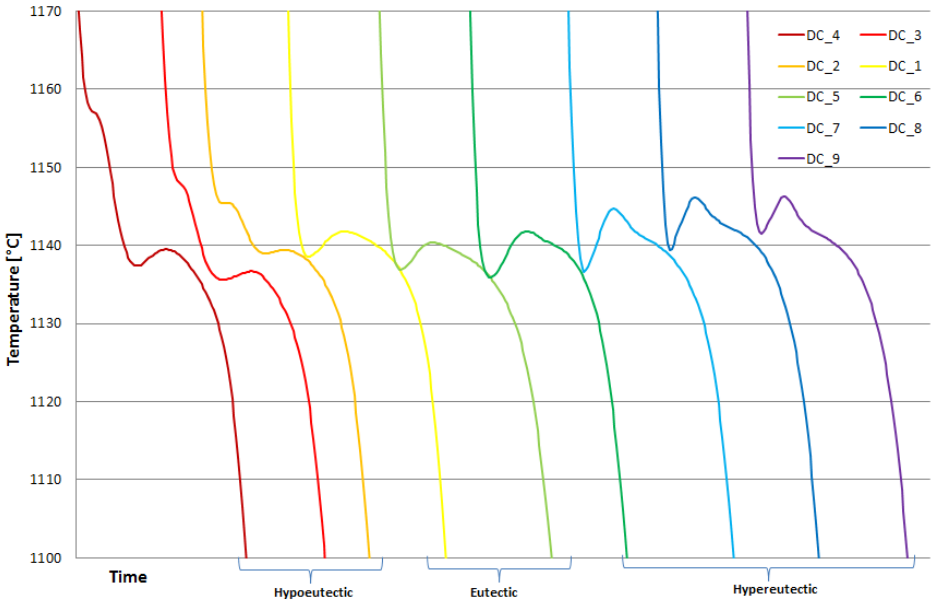

Figure 118 - Solidification curves from the trials to evaluation the impact of the melt's feeding needs.

From the poured moulds, the castings defects were evaluated according to the procedure described in 4.3.4 and the results are presented in **Table 45**.

Table 45 - Results from the shrinkage and porosity evaluation from the casting poured during the trials to evaluation the impact of the melt's feeding needs trials.

	Open shrinkage vol.			Shrinkage vol.			Porosity Index			**Contraction Defect Index**		
Ladle number	**S1 (mm^3)**	**S2 (mm^3)**	**S3 (mm^3)**	**S1 (mm^3)**	**S2 (mm^3)**	**S3 (mm^3)**	**S1**	**S2**	**S3**	**S1**	**S2**	**S3**
DC_1	0	0	0	0	0	0	613	0	15	613	0	15
DC_2	0	0	0	0	0	0	501	0	0	501	0	0
DC_3	0	0	0	0	0	0	184	0	822	184	0	822
DC_4	0	0	3700	0	0	0	54	0	0	54	0	3600
DC_5	0	0	0	0	0	0	612	0	0	612	0	0
DC_6	0	0	0	0	0	0	373	0	1033	373	0	1033
DC_7	0	0	0	0	0	1400	489	0	0	489	0	1448
DC_8	0	0	0	0	0	1800	907	0	0	907	0	1944
DC_9	0	0	0	0	0	2800	612	0	0	612	0	3175

Once again, at section number 2 no defects were found. The evaluation of the defects present in the section 1 of the test casting presented in **Figure 119**, show that only porosity was present. The results suggest that porosity in section 1 of the casting is lower for melts with lower liquidus temperature. For eutectic and hypereutectic solidification morphologies, the porosity is always present in the test casting with no tendency of variation. In **Figure 119**, the order of appearance of the test castings along the X-axis is made from the samples more hypoeutectic (theoretically lower C.E.) to the more hypereutectic (theoretically higher C.E.).

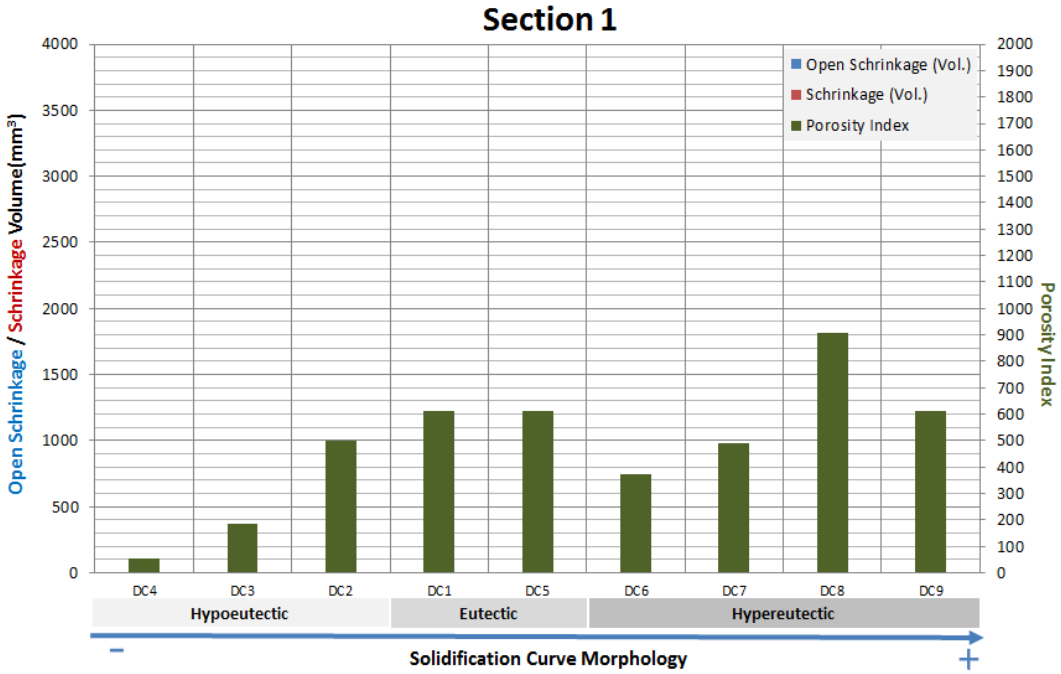

Figure 119 - Evaluation of the different defects in section 1 of the test casting from the trials to evaluation the impact of the melt's feeding needs.

The evaluation of the defects in section 3 showed different types of defects, although they varied strongly with the solidification morphology. Open shrinkage defects were found only once, for the casting DC_4 which was the sample with the highest liquidus temperature. Shrinkage defects were only found on test castings poured with melts that had hypereutectic solidification morphology. The samples that had no defects or very small defects were the ones poured with eutectic or slightly hypoeutectic (close to eutectic) solidification morphologies, as presented in the graphic from **Figure 120**. Porosity was found only in the test castings in the intermediate state from the ones that had high shrinkage and no shrinkage.

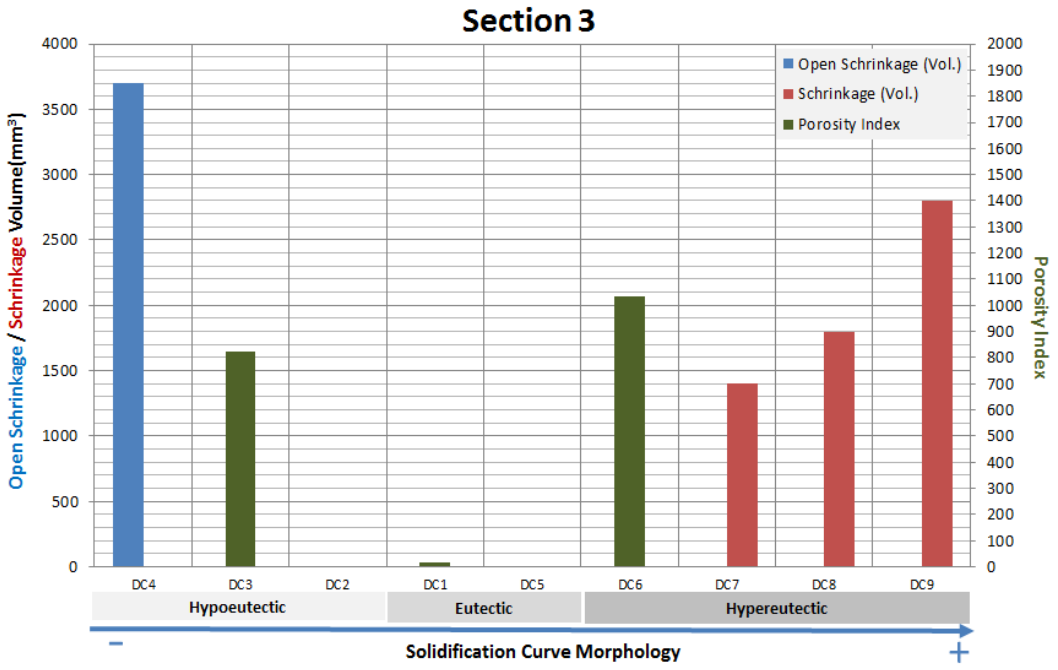

Figure 120 - Evaluation of the different defects in section 3 of the test casting from the trials to evaluation the impact of the melt's feeding needs.

In terms of overall contraction defect, regardless of any pre-defined classification, were only the magnitude of the defects counts, the effect of the solidification morphology is better represented in the real feeding needs of the different melts. This representation can be seen in the graphic from **Figure 121**, where the *Contraction Defect Index* is presented for both section 1 and 3.

For section 1, no defined tendency is found on the variation of the contraction defect for most of the solidification morphologies tested. There is only a slightly tendency for the melts that had a more strong hypoeutectic solidification to have slightly less contraction defects.

The higher sensibility to the variation of the melts solidification morphology is found for section 3. For melts with a eutectic solidification morphology, or slightly hypoeutectic solidification morphology with very low liquidus temperature and high inoculation state (close to eutectic), there are no (or minimum) contraction defects found. For hypoeutectic solidification morphologies, as the liquidus temperature increases (meaning presence of less carbon and stronger dendritic growth) the volume deficit after solidification increases. For hypereutectic compositions, the contraction defects increase and became higher as the solidification morphology becomes more hypereutectic.

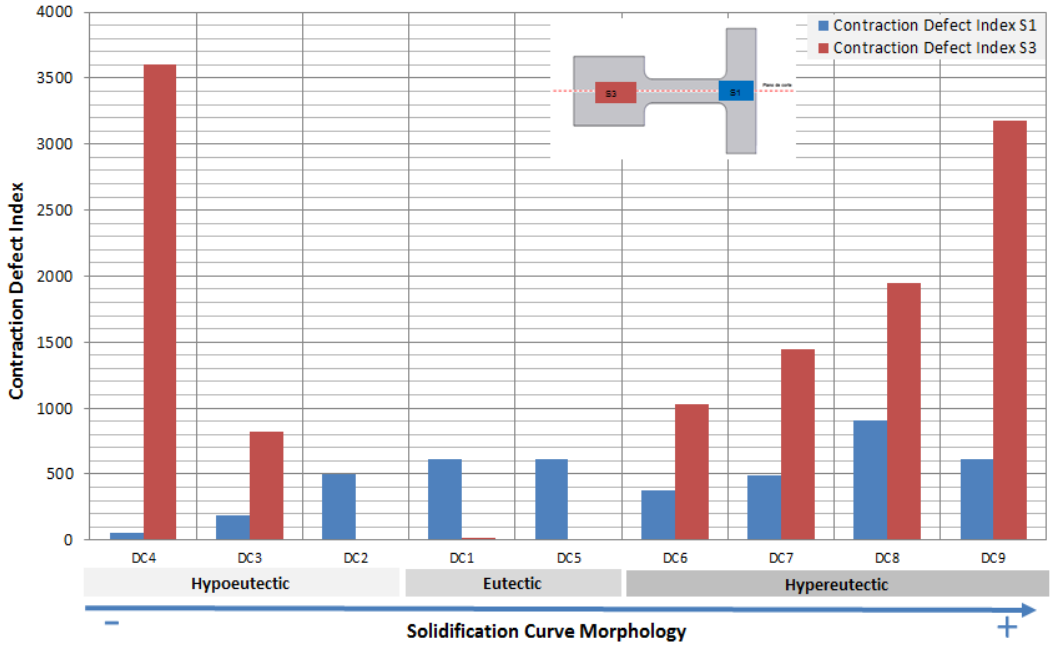

Figure 121 - Evaluation of defects in both section of the test expressed as a Contraction Defect Index, from the trials to evaluation the impact of the melt's feeding needs.

From all test castings, 3 representative samples, from section 3, for the 3 solidification morphologies obtained were selected for metallographic evaluation. The main metallographic results concerning to the graphite structure are given in **Table 46**. From the results it is visible that, the percentage of graphite increased from a more hypoeutectic to a eutectic melt, justifying the improvement on the self-feeding abilities of the casting (more graphitic expansion). Nevertheless, this rule does not apply for hypereutectic solidification morphologies where although the graphite percentage has increased, the volume contraction defects increased.

Table 46 - Graphite structure characteristics from samples DC_4, DC_5 and DC_9.

	DC_4	CD_5	DC_9
Nodularity [%]	76	78	86
Phase Area of Graphite [%]	8,4	9,1	11,0
Graphite Particle Density [1/mm^2] (Ø>20µm)	174	141	108

The same metallographic samples were also submitted to colour etching observation. For the test casting DC_4, the obtained micrographs are presented in **Figure 122**, where the network of dendrites in clearly visible and some primary dendrite arms reach more than 1mm of length (visible on the left micrograph from **Figure 122**).

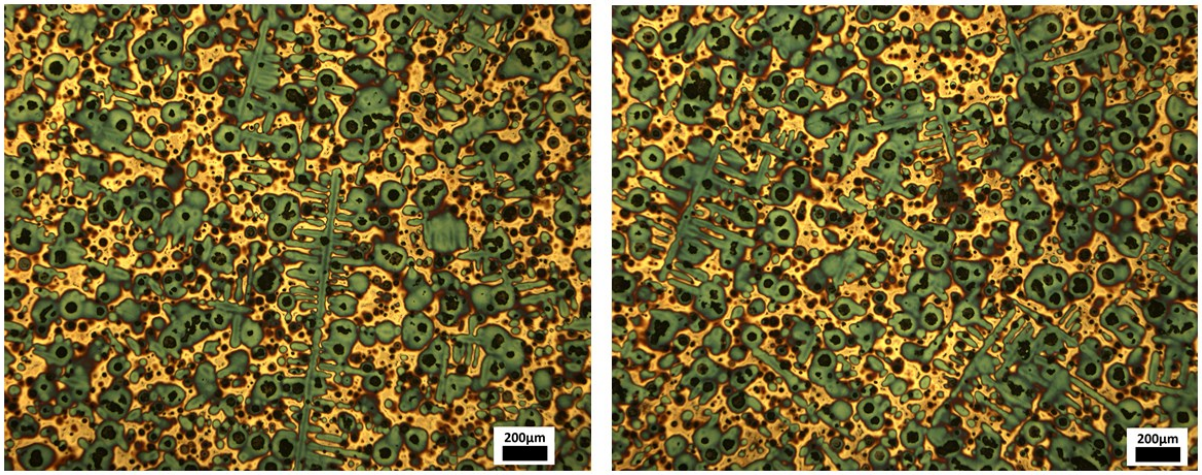

Figure 122 - Micrographs of the samples from test casting DC_4, at section 3, after colour etching with reagent No.1 (table 13) for 17minutes.

For sample DC_5, with eutectic solidification morphology, the micrographs with colour etching are presented in **Figure 123**. In comparison to the sample DC_4, there is no clear visible dendrite recognizable in the microstructure. This might indicate that in eutectic solidification morphologies, the independent dendritic growth does not occur often (possibly no off eutectic dendritic growth), and the solidification proceeds mainly by the solidification of austenite shells around the graphite nodules.

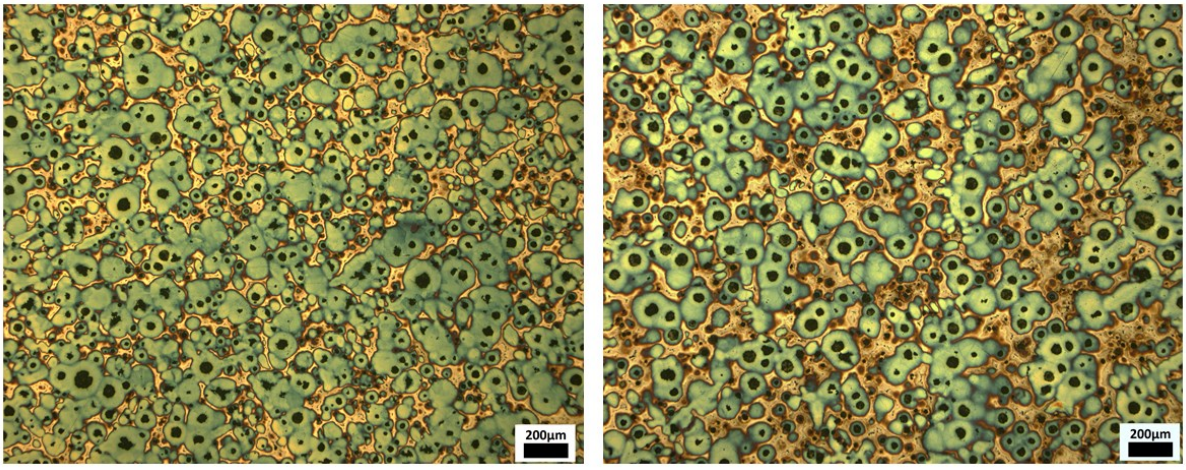

Figure 123 - Micrographs of the samples from test casting DC_5, at section 3, after colour etching with reagent No.1 (table 13) for 20minutes.

The micrographs obtained for the hypereutectic sample DC_9, presented in **Figure 124**, reveal again the presence of some dendritic structures. The dendrites visible in this sample are much smaller in length and not so brunched like the ones from hypoeutectic samples, but still their presence is noticeable. This dendrites form most likely, according to literature due to the decrease of carbon content in the melt due to the fast diffusion of carbon to the growing primary graphite nodules. When remaining melt reaches the solidification temperature and if the carbon content of the melt and inoculation potential allow it, the melt may solidify as a hypoeutectic melt.

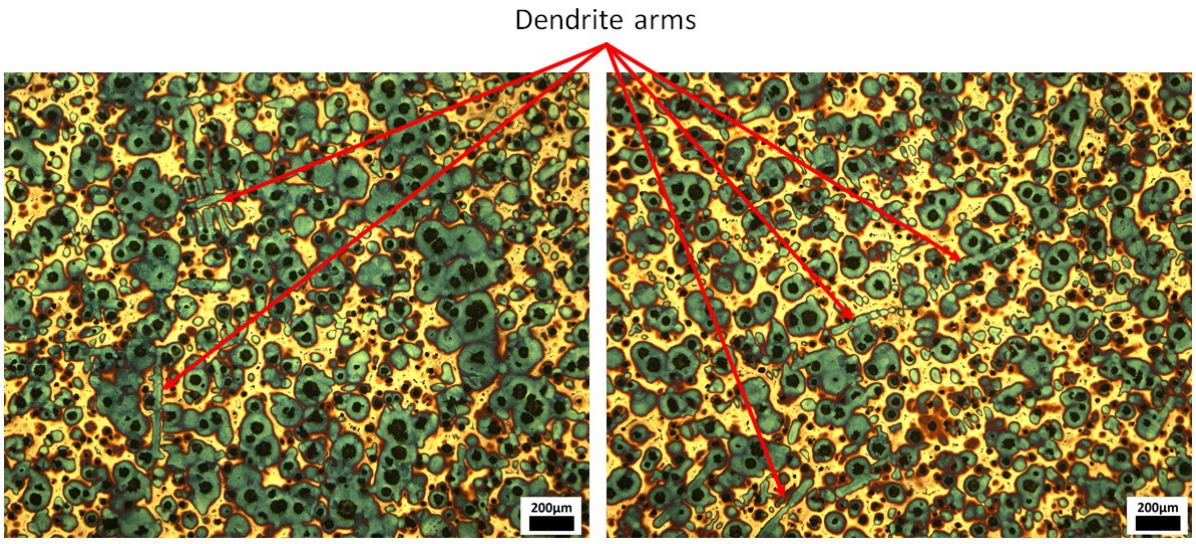

Figure 124 - Micrographs of the samples from test casting DC_9, at section 3, after colour etching with reagent No.1 (table 13) for 17minutes.

6. Discussion of Results

6.1. Solidification morphology and dendritic coherency point detected by thermal analysis

For the evaluation and discussion of the results obtained in this work, we start with the characterization of the solidification of nodular cast iron described using the thermal analysis technic, from the results obtained in the experiments from chapter 5.1and 5.2.

From the quenching trails of chapter 5.1, the differences between the microstructure evolution of the 3 different solidification curves shows that the curve shape represents indeed different solidification morphologies, for hypoeutectic, eutectic and hypereutectic. Especially the differences obtained for the hypoeutectic and hypereutectic solidification curves after quenching, presented in the micrographs from **Figure 82** and **Figure 84** for the hypoeutectic sample and **Figure 89** and **Figure 91** for the hypereutectic prove this classification.

In the curve with hypoeutectic morphology a bigger and wider dendritic structure exists (see **Figure 82a**), when quenched after the liquidus temperature. Surprizing was the observation of nodules with a diameter of up to 24µm that have nucleated alongside the dendrite arms. Literature indicates that nodules should only nucleate at the eutectic transformation temperature, but once the sample was quenched before that point, this shows that there is a small amount of nodules that start to solidify before the eutectic stage is reached. The phase of graphite in the hypoeutectic sample quenched after the liquidus temperature reaches 1,8%. For the sample quenched at the eutectic low temperature (see **Figure 82b**), it is visible that nodules start also to nucleate in the bulk liquid and the dendrites start to be more breached, indicating that the eutectic transformation is taking place.

For the hypereutectic curve morphology quenched just after the start of solidification (see **Figure 89a**), the graphite structure presents nodules that have already up to 44µm of diameter and total graphite phase percentage of approximately 4%, indicating that they have grown very fast astonishingly at a very early solidification stage, which only happens when graphite grows in contact with the liquid (primary nodule growth). The micrographs show also that there is an

agglomeration of nodules that occurs when graphite particles nucleate in the liquid and float until they find a barrier. The micrographs show also that the bigger graphite nodules precipitate independent of the small dendrites, directly in the bulk liquid. Although the dendritic structure observed in hypereutectic melts is already dense (the reason for this will be presented below), the main dendrite arms are not as long as in the hypoeutectic sample. When quenched at the eutectic point, the microstructure reveals coarsening and the maximum nodule size increased to 56 μm.

For the eutectic curve, due to the difficulty of cooling the sample during the recalescence, the microstructure from **Figure 86** shows that at the EuUp point the sample is almost completely solidified, so the observation of the structure development is not possible. But once the eutectic solidification curve was obtained for a intermediate carbon content between the hypoeutectic and the hypereutectic solidification curves and it exhibits only one plateaus during solidification, it is still believed to be the real eutectic solidification morphology.

The comparison from the normal solidification microstructure obtained for the 3 solidification morphologies (**Figure 82c**, **Figure 87b** and **Figure 89c**) shows that as the solidification curve morphology goes from hypoeutectic to hypereutectic, the percentage of graphite phase increases and the nodules have higher maximum diameter. In the hypereutectic case the graphite structure is characterized by the presence of the big primary graphite nodules beside smaller nodules that solidified later in the eutectic.

These evidences show that the curves morphologies presented in **Figure 77** indeed represent the solidification morphology of hypoeutectic, eutectic and hypereutectic melts.

The determination of the dendritic coherency point presented in **Figure 93** shows that the point occurs in different stages of the solidification for the different solidification morphologies.

For the hypoeutectic curves the DCP occurs approximately at the MIR point between the liquidus temperature and the eutectic low temperature. The micrographs from the quenching test in hypoeutectic morphology melts (**Figure 82a**), show that when quenching was done before the DCP (short before the MIR point) the dendritic structure has still wide intervals between arms, with primary dendrite arm spacing of approximately 270μm, almost no secondary arm branching and wide areas that were still liquid when the sample was quenched. This indicates that at that stage, there is yet no dendritic coherency. The sample quenched after the DCP (**Figure 82c**) shows that the dendritic structure is denser with lower primary dendrite arm spacing and strong

branching and the liquid regions are smaller, indicating that dendritic coherency point has already occurs. This observation confirm the determination of the DCP has being close to the MIR point in melts with a hypoeutectic solidification morphology.

For eutectic solidification morphologies, the DCP was determined to be at the first minimum of the inverse of the 1st derivative curve that occurs in the solidification curve short after the low eutectic point. The quenching performed to a eutectic sample after that point (**Figure 86**) shows that after it the dendritic coherency point had already occurred. A quenching of a sample before the suggested DCP point in eutectic melt compositions was not possible because the melt was still too close to the liquid state when inserted in the water.

For hypereutectic solidification morphologies the DCP occurs, according to the determination from **Figure 93d**, approximately at the upper Liquid temperature (more precisely 1st minimum of the 2nd derivative after the beginning of solidification), short after the beginning of solidification. The quenching test of hypereutectic morphology curves show that when the quenching was done after the start of solidification, approximately at the same point now indicated as the DCP, the microstructure (see **Figure 89a**) shows already a branched structure of small dendrites (possibly off eutectic dendrites) and already small areas of liquid, indicating indeed that is possible that DCP had just occurred.

Therefore, based on these results, it is hereby considered that the DCP approximately occurs at the points graphically represented in **Figure 93** and indicated in **Table 22**.

6.2. Comparison between the solidification morphology indicated by the C.E. value and the real solidification morphology, accounting the inoculation effect

The comparison between the solidification morphology determinate through calculation of the C.E. value from the equilibrium solidification diagram and the real solidification morphology can be done based on the results obtained for chapters 5.3 and 5.4.

The results from the experiment performed in chapter 5.3, and especially the results presented in **Figure 97** shows that it is possible to obtain curves with hypoeutectic solidification morphology, confirmed by the trials from chapter 5.1, for C.E. values of eutectic and hypereutectic melt compositions according to the equilibrium phase diagram.

Figure 98, shows that the solidification morphology, for melt composition with a C.E. value close and higher than the eutectic, is dependent on the inoculation characteristics of the melt and are therefore dependent on the inoculation potential. The figure shows that for a melt with a C.E. equal or higher than the eutectic value, with a liquidus temperature close or below 1150°C, the melt can solidify with a hypoeutectic morphology if the inoculation potential is low, or eutectic if the inoculation potential is high. Once this is a kinetic process, it is only recognizable through the use of thermal analysis measurement.

With low inoculation potential the precipitation of the graphite particles in the eutectic requires a higher undercooling after the liquidus temperature, causing the eutectic temperature to decrease. If the inoculation potential of the melt is low, the temperature for the eutectic solidification will decrease. If this eutectic temperature is below the liquidus temperature, this means that during cooling of the melt the liquidus temperature will be reached first and the eutectic later, causing a hypoeutectic solidification morphology.

On the contrary, if the eutectic temperature and the liquidus temperature are at the same temperature range, they will be reached simultaneously during cooling of the melt, resulting in a single eutectic solidification transformation. This concept is demonstrated in **Figure 104**, where to the same melt (same C.E. value) different inoculants were added with different inoculation potentials. In the figure the solidification curves are ordered as a function of the inoculation potential, increasing from left to right, and it is visible that as the inoculation potential increases, the eutectic temperature (more specifically the low eutectic temperature) start to rise and the difference to the liquidus temperature gets smaller. When the inoculation potential is strong enough to induce very small undercooling and the liquidus temperature and eutectic low temperature are the same, the solidification occurs according to eutectic solidification morphology.

The inoculation potential of the melt, can be therefore precisely controlled using the thermal analysis technic through the control of the undercooling (eutectic low temperature), for different

types of inoculants, as presented in the **Figure 103** and **Figure 105**. There is demonstrated that the estimation of a *Inoculant Index* based on quantitative and qualitative evaluation of the graphite structure has a high correlation with the thermal analysis curve variables, and specifically with the low eutectic temperature.

6.3. Evaluation of the melts feeding necessities as a function of the real solidification morphology determined by thermal analysis

The impact of the real solidification morphology of the melt determined by thermal analysis was evaluated in the trials and presented in chapter 5.5 and 5.6.

The results from the first trials (chapter 5.5), where the effect of liquidus temperature on the volume contraction defects in a test casting, for hypoeutectic solidification morphologies was tested, revealed that for high liquidus temperatures there are more shrinkage defects than for lower liquidus temperatures. The graphics from **Figure 109** and **Figure 110** show a tendency that the volume contraction effect is smaller if the liquidus temperature is lower (more carbon) for both sections. The metallographic changes in the samples between high and low liquidus temperature show that two factor might have contributed to the reduction of the contraction defect volume. First the increase of the percentage of graphite in the sample (from 8,1% to 9,3%) meaning that there will be more expansion due to graphite growth. Secondly, the dendritic structure in the sample is considerably smaller in lower liquidus temperature samples compared to high liquidus temperatures, as presented in the micrographs from **Figure 115**.

This means that having lower liquidus temperature increases both the amount of graphite that is the origin of expansion during solidification and reduces the dendrite network from the primary dendrites that improve the melt flow during solidification, especially when the solidification reached the mushy solidification stage and the melt has to flow through the interdendritic spaces. This way the melt expansion from the graphite is increased and this expansion effect on the melt can travel more freely in the castings cavity.

The performance of the trials from chapter 5.6 allowed the study of this some principles presented in the previous study from chapter 5.5, to all 3 types of solidification morphology of cast iron. Unfortunately, the comparison between the results obtained in the two trials cannot be

directly compared once they were performed using different sand moulds. So, although the defects obtained in both trials are not exactly the same, due to the influence that the different sand mould can have in the defect, the tendencies to have more or less volume defect can be similar.

From this trial, all 3 types of solidification morphologies were obtained (see **Figure 118**), according to the evaluation of the solidification morphology using the thermal analysis curves.

The evaluation of the defect in section 1 shows only the presence of porosity, as presented in **Figure 119**. The use of different solidification morphologies, within the ranges tested did not showed a significant influence in the defect as it is always present and its extension changes only slightly and randomly between the different castings. There is only a slight reduction of the defect as the liquidus temperature increase for hypoeutectic solidification melts, but not clear to take any conclusions. More tests with hypoeutectic melts with higher liquidus temperatures are required to take any conclusion. But in general, the defect exists for the 3 types of solidification morphology.

Concerning the section 3, it is observed through the graphic from **Figure 120** that for highly hypoeutectic solidification morphologies with high liquidus temperature, there is the occurrence of a big open shrinkage defect. As the liquidus temperature decrease the big open shrinkage defect turns into porosity and if the liquidus temperature decrease further, no more shrinkage or porosity defect is present.

For eutectic solidification curves the defect presence is minimal or non-existent in section 3.

As the solidification morphology starts to be hypereutectic, porosity starts to appear again and if the solidification morphology turns more hypereutectic, this porosity evolves into a shrinkage cavity that keeps growing as the melt is further hypereutectic.

Based on these observations, the melt morphology that gives less contraction volume defects are the eutectic and the hypoeutectic solidification morphologies close to eutectic with low liquidus temperature and very good inoculation potential.

The reason for the appearance of shrinkage for hypoeutectic melts with high liquidus temperature and low inoculation potential, are the same as presented for the conclusions of trials from chapter 5.5, and are related to the low percentage of graphite (see **Table 46**) and the presence of bigger dendrites in the microstructure, as presented in the **Figure 122**.

For close to eutectic solidification morphologies and eutectic solidification morphologies, the carbon content in the melt is higher (see **Table 46**) and the dendritic structure is smaller, as presented in the **Figure 123**.

For hypereutectic solidification morphologies, the shrinkage increases again, although it has even more carbon than the eutectic morphology samples, and the dendrites are again more visible in the structure, as presented in **Figure 124**.

The explanation to the fact that the volume contraction defects increase for hypereutectic curve morphologies, despite the higher amount of graphite in the structure, is due to the amount of graphite that nucleated and grows before the occurrence of the dendritic coherence point.

Reviewing again the results from the quenching test, at the approximate time of occurrence of the DCP in hypereutectic melts, approximately 47% of the total graphite had already nucleated. For a hypoeutectic melt this percentage if of approximately 25%. This means that half of the available graphite in the hypereutectic cast iron can grow before the point where it is really needed to compensate the local natural shrinkage of the melt, after the DCP. In terms of percentage of graphite area measured in the sample, the hypereutectic sample has 4,3% of graphite area that nucleates after the DCP and the hypoeutectic has 5,3%. The conclusion is that in hypereutectic solidification melts the amount of graphite that nucleates after the DCP can be smaller than at hypoeutectic solidification morphologies. This fact explains why the volume contraction in the casting increases again as the melt becomes more hypereutectic.

Although no information on the amount of graphite that had solidified until the DCP point in eutectic solidification morphologies was obtained, the observation of the microstructure from **Figure 87b** (for normal eutectic melt solidification) and **Figure 91c** (for normal hypereutectic melt solidification), shows that in the eutectic case the biggest graphite particles are approximately only 53% of the size of the biggest hypereutectic particles. Considering that the biggest graphite particles are big because they grow fast when in contact with the liquid before and while the DCP point occurs, it is assumed that in the eutectic melt there is not so much primary graphite nodule growth as in the hypereutectic, meaning that less graphite will grow before the DCP point.

The results obtained in this trial indicate that, in order to reduce the melt feeding necessities, the carbon content should be as high as possible and should nucleate and grow only after the DCP

point. This is achieved for eutectic or close to eutectic solidifications morphologies. Hypoeutectic morphologies tend to have to less carbon and too much dendrites that cause restrictions to the melt flow when expansion occur and hypereutectic morphologies loose great part of the expansion potential of the graphite because nodules starts to grow very fast still before the DCP is achieved.

7. Conclusions

The trials performed in the present work, allowed the analysis of relevant data to the subjects under investigation in this thesis and the conclusion are now presented.

The use of the thermal analyses, though the evaluation of the main plateaus of the solidification curve, allows the recognition of the real solidification morphology of a melt that solidifies hypoeutectic, eutectic or hypereutectic, according to the stable solidification of carbon forming graphite.

It was also demonstrated that the solidification morphology changes for the same C.E. value, influenced by the inoculation potential of the melt. If the melt has a low inoculated state, it can solidify with a hypoeutectic morphology even for C.E. values that are typically eutectic or hypereutectic. This means the inoculation state can cause the melt to exit or enter the non-symmetrical eutectic region defined previously by the literature on chapter 3.3.1.5, for the same chemical composition of the melt. The inoculation potential will change for different types of inoculants (for the same addition amount) and therefore can alter the solidification morphology.

The dendritic coherency point in cast iron melts with hypoeutectic compositions occurs between the liquidus and the eutectic transformation, approximately at the point identified as MIR, where the cooling speed in that section of the curve reached a maximum. The DCP occur therefore before the nucleation of the eutectic. Nevertheless the results from the quenching test for hypoeutectic samples revealed that the precipitation of graphite nodules occur along the primary dendrites, before the eutectic reaction plateau in the curve and even before the DCP. This observation goes against the conventional theories that the graphite particle start to grow only in the eutectic region of hypoeutectic morphology melts.

For eutectic morphology melts the DCP occurs after the low eutectic temperature at the point where the recalescence has its higher heating rate (1^{st} minimum in the inverse of the 1^{st} derivative after eutectic low point). For hypereutectic morphologies the DCP occurs at the upper liquidus temperature (1^{st} minimum of the 2^{nd} derivative after liquid low point).

The morphology of the solidification curve revealed to influence the feeding requirements of the melt, evaluated as the contraction volume measured in a test casting.

The minimum feeding requirements for a nodular cast iron melt are achieved for solidification morphologies that are eutectic or hypoeutectic close to eutectic.

Usual hypoeutectic melts have less percentage of graphite in the structure and a high developed dendritic structure. Both increase the feeding necessities due to the lack of carbon for expansion and the difficulties associated to the melt flow in the mushy zone, referred in the literature by Stefanescu.

For hypereutectic solidification morphologies, although they have higher carbon content and will have therefore higher amount of graphite phase in the microstructure, most of that graphite nucleated before the DCP was reached. This is caused by the fact that the primary graphite nucleates and grows very fast in the liquidus phase, before the DCP is reached, and when the DCP is reached the amount of graphite still to nucleate and grow is small, causing less expansion after the DCP. The feeding requirement will be higher as the melt becomes more hypereutectic.

Therefore, for eutectic composition and hypoeutectic compositions close to the eutectic is possible to have the highest amount possible of graphite nucleating after the DCP point, reducing the feeding necessities to the minimum.

Bibliographic References

[1] D. Wagner, Iron and Steel in Ancient China, Leiden - The Netherland: E.J.Brill, 1996, pp. 335-339.

[2] B. Gasgcoine, "History of Metallurgy," History World, 2001. [Online]. Available: http://www.historyworld.net/wrldhis/PlainTextHistories.asp?ParagraphID=ahh. [Accessed 03 06 2014].

[3] A. Handbook, Castings, vol. 15, ASM International, 2008, pp. 54-55,317-327, 835.

[4] DIN EN ISO 945-1:2009 + Cor. 1:2010, *Mikrostruktur von Gusseisen – Teil 1: Graphitklassifizierung durch visuelle Auswertung,* DIN, 2010.

[5] BDG, Gusseisen mit Kugelgraphit: Herstellung - Eigenschaften - Anwendung, Düsseldorf: Bundesverband der Deutschen Gießerei-Industrie, 2007, p. 2.

[6] AFS, "47th Census of World Casting Production 2012," *Modern Casting,* p. 19, December 2013.

[7] AFS, "39th Census of World Casting Production 2004," *Modern Casting,* p. 28, December 2005.

[8] AFS, "40th Census of World Casting Production 2005," *Modern Casting,* p. 29, December 2006.

[9] AFS, "41th Census of World Casting Production 2006," *Modern Casting,* p. 23, December 2007.

[10] AFS, "42th Census of World Casting Production 2007," *Modern Casting,* p. 25, December 2008.

[11] AFS, "43th Census of World Casting Production 2008," *Modern Casting,* p. 19, December 2009.

[12] AFS, "44th Census of World Casting Production 2009," *Modern Casting,* p. 25, December 2010.

[13] AFS, "45th Census of World Casting Production 2010," *Modern Casting,* p. 16, December 2011.

[14] AFS, “46th Census of World Casting Production 2011,” *Modern Casting,* p. 26, December 2012.

[15] J. Radzikowska, “Metallography and Microstructures of Cast Iron,” in *Metallography and Microstructures Vol.9 ASM Hanbook*, Ohio - USA, ASM International, 2004, pp. 565-587.

[16] V. Anjos, C. S. Ribeiro, J. Cunha and C. Gomes, “The Use of Thermal Analysis to Compare Solidification Pattern and Evaluate Performance of Several Inoculants in SG,” in *71st World Foundry Congress*, Bilbao - Spain, 2014.

[17] DIN EN 1563:2012-03, *Gießereiwesen – Gusseisen mit Kugelgraphit,* DIN, 2012.

[18] R. D. Forrest, “What is the Optimum Base Iron Sulphur Content Prior to Nodularization?,” *Sorelmetal Technical Service - Rio Tinto Iron & Titanium Inc.,* no. 95, March 2006.

[19] J. R. Brown, Foseco Ferrous Foundryman's Handbook, Oxford - Great Britain: Butterworth Heinemann, 2000.

[20] G. M. Hansen, C. Hartung and D. White, “The Ductile Iron Treatment Process Revisited,” in *71st World Foundry Congress*, Bilbao - Spain, 2014.

[21] P. Cabanne, “Magnesium Cored Wire Treatment Advantages and Disavantages Vis-À-Vis Other Processes,” *Sorelmetal Technical Service - Rio Tinto Iron & Titanium Inc.,* no. 109, 2006.

[22] W. Baumgart, J. Cunha and V. Anjos, “Het enten van gietijzer,” *Gietwerk Perspectief Magazine - No.5,* pp. 5-12, October 2010.

[23] Foseco, “INITEK Process Brochure,” Foseco International Limited, May 2011. [Online]. Available: http://www.foseco.com/fileadmin/_migrated/content_uploads/INITEK_16.pdf. [Accessed 12 August 2014].

[24] W. Baumgart and V. Anjos, Directors, *The OCC CGI Process.* [Film]. Mönchengladbach - Germany: OCC GmbH, 2013.

[25] W. Baumgart , “OCC GmbH Produktportfolio - Teile 3,” 2014. [Online]. Available: http://www.occ-web.de/fileadmin/download/OCC_Portfolio_2014_Deu_Teil_3.pdf. [Accessed 12 August 2014].

[26] OCC, “OCC GJS/GJV Navigator,” OCC GmbH, 2014. [Online]. Available at: www.occ-web.de/index.php?id=navigator&L=%25Findex.php%25Fsg%25D%25%20onfocus%3DblurLink%28this%29%3B. [Accessed 12 August 2014].

[27] W. Baumgart, “OCC GmbH Produktportfolio 2014 - Teile 1,” 2014. [Online]. Available: http://www.occ-web.de/fileadmin/download/OCC_Portfolio_2014_Deu_Teil_1.pdf. [Accessed 12 August 2014].

[28] OCC, “OCC GmbH AccuVo Doppelkammertiegel,” OCC GmbH, 2014. [Online]. Available: http://www.occ-web.com/index.php?id=accuvo&L=1%27%22. [Accessed 12 August 2014].

[29] SinterCast, “SinterCast System 3000,” SinterCAst AB, 2014. [Online]. Available: http://sintercast.com/technology/system-3000-2. [Accessed 12 August 2014].

[30] Foseco, “ITACA 8 Product Brochure,” May 2011. [Online]. Available: http://www.foseco.com/fileadmin/_migrated/content_uploads/ITACA_15.pdf. [Accessed 12 August 2014].

[31] NovaCast, “NovaCast System AB - Product Sheet - ATASmetstar,” 2014. [Online]. Available: http://novacast.se/wp-content/uploads/2013/06/PRODUKTBLAD-ATAS-Metstar.pdf. [Accessed 12 August 2014].

[32] D. M. Stefanescu, Science and Engineering of Casting Solidification, New York - USA: Springer Science+Business Media, 2009, pp. 1-4.

[33] J. A. Dantzig and M. Rappaz, Solidification, Lausanne - Switzerland: EPEL Press, 2009.

[34] G. Lesoult, M. Castro and J. Lacaze, “Solidification of Spheroidal Graphite Cast Irons - I Physical Modelling,” *Acta Metallurgica,* no. Vol.46 Nr.3, pp. 983-995, 1998.

[35] W. F. Smith, Structure and Properties of Engineering Alloys, 2nd Edition ed., McGraw Hill International, 1993, p. 340.

[36] J. Zhou, “Colour Metallography of Cast Iron - Chapter 1 Introduction (I),” *China Foundry,* vol. 6, no. 1, pp. 57-65, February 2009.

[37] W. R. Heine, The Fe-C-Si Solidification Diagram for Cast Iron, AFS Transactions, 1986, pp. 391-403.

[38] G. Rivera, P. R. Calvillo, R. Boeri, Y. Houbaert and J. Sikora, “Examination of the solidification macrostructure of sepheroidal and flake graphite cast irons using DAAS and ESBD,” *Materials Characterization Ed.59,* pp. 1342-1348, 2008.

[39] J. Zhou, “Colour Metallography of Cast Iron - Chapter 3 Spheroidal Graphite Cast Iron (I),” *China Foundry,* vol. 7, no. 1, pp. 183-189, May 2010.

[40] H. Nakae, S. Jung and T. Kitazawa, “Eutectic Solidification Mode of Spheroidal Graphite Cast Iron and Graphitization,” in *Science and Processing of Cast Iron VIII*, Beijing, 2006.

[41] L. Svensson, A. Diószegi and K. Z. Liu, “Inoculattion of Primary Austenite in Grey Cast Iron,” in *Science and Processing of Cast Iron VIII*, Beijing, 2006.

[42] N. L. Veldman, A. K. Dahle, D. H. StJohn and L. Arnberg, “Dendrite Coherency of Al-Si-Cu Alloy,” *Metallurgical and Materials Transactions A - ASM Transaction,* no. 32A, pp. 147-155, January 2001.

[43] M. B. Djurdjevic and J. H. Sokolowski, “Determination of dendrite coherency point characteristics using first derivative curve versus temperature,” *Journal of Thermal Analysis and Calorimetry - Springer,* pp. 875 - 882, 8 June 2012.

[44] T. Skaland, F. Grong and T. Grong, “A Model for the Graphite Formation in Ductile Cast Iron: Part I. Inoculation Mechanisms,” *Metallurgical Transactions A - Vo. 24A,* pp. 2321-2347, October 1993.

[45] D. M. Stefanescu, “Solidification and modeling of cast iron - A short history of the defining moments,” *Material Science and Engineering A 413-414,* pp. 322-333, 2 Ausgust 2005.

[46] D. D. Double and A. Hellawell, “The Nucleation and Growth of Graphite - The Modification of Cast Iron,” *Acta metall. mater. Vol.43 No.6,* pp. 2435-2442, 21 August 1994.

[47] W. Oldfield, “Trans of the ASM 59,” p. 945, 1966.

[48] G. Rivera, J. Sikora and R. Boeri, *AFS Transations,* p. 979, 2003.

[49] C. F. Yeung, H. Zhao and W. B. Lee, “The Morphology of Solidification of Thin-Section Ductile Iron Castings,” *Material Characterization Vol. 40,* pp. 201-208, April 1998.

[50] K. M. Pedersen, J. H. Hattel and N. Tiedje, “Numerical modeling of thin-walled hypereutectic ductile cast iron parts,” *Acta Materialia Vol.54,* pp. 5103-5114, 2006.

[51] D. M. Stefanescu, “State of the Art in Solidification modeling of Cast Iron,” in *Science and Processing of Cast Iron VIII*, Beijing - P.R.China, 2006.

[52] E. Scheil and W. Hütter, *Arch. Eisenhüttenwesen 4,* p. 24, 1953.

[53] J. Zhou, S. Engler and W. Schmitz, "Formation of Austenite Shell around Nodular Graphite and its Effect on Deterioration of Graphite," *AFS Transactions Vol.98,* pp. 783-786, 1990.

[54] S. Hasse, Guß- und Gefügefehler, Berlin: Schiele & Schön GmbH, 2003.

[55] I. Jimbo and A. W. Cramb, "The density of liquid iron-carbon alloys," *Metallurgical and Materials Transactions B Vol.24,* pp. 5-10, February 1993.

[56] W. Hemminger and S. M. Sarge, "Definition, Nomenclature, Terms and Literature," in *Handbook of Thermal Analysis and Calorimetry Vo.1*, Amsterdam - The Netherlands, Elsevier Science B.V., 1998, pp. 8-14.

[57] W. Baumgart, "Untersuchung des Phasenübergangs von flüssig nach fest am tertiären System Fe-C-Si unter Nichtgleichgewichtsbedingungen," Lehrstuhl für das gesamte Gießereiwesen und Gießerei-Institut der RWTH Aachen, Aachen - Germany, 2013.

[58] C. R. Loper, R. W. Heine and M. D. Chaudhari, "Principles Involved in the Use of Cooling Curves in Ducitle Iron Process Control," *Transactions of the American Foundrymen's Society Vol.82,* pp. 431-440, 1974.

[59] V. Anjos, W. Baumgart and J. Cunha, "Grundlagen der Thermischen Analyse," in *OCC Seminar - Metallurgishe Regelkreise*, Mönchengladbach, 2014.

[60] C. R. Loper, R. W. Heine and A. Shah, "AFS Trans. Vol.75," *AFS Transactions,* p. 541, 1967.

[61] C. R. Loper and P. K. Basutkar, "Predicting Graphite Nodularity in Heavy Section Ductile Iron By Thermal Analysis - Part I Correlation of Microstructures with Thermal Analysis in Heavy Section Ductile Iron Castings," *Transactions of the American Foundrymen's Society Vol.79,* pp. 169-175, 1971.

[62] L. Bäckerud, K. Nilsson and H. Steen, "The Metallurgy of Cast iron," St. Saphorin - Switzerland, Georgi Publishing Co., 1975, p. 625.

[63] D. M. Stefanescu, "The Physical Metallurgy of Cast Iron," Elsiver, 1985, p. 151.

[64] W. Baumgart and V. Anjos, "Thermal Analysis of Ductile Iron," in *OCC Seminar - Metallurgishe Regelkreise*, Mönchengladbach, 2009.

[65] V. Anjos, C. A. Silva Ribeiro and J. Cunha, "Produção de Ferro Fundido de Grafite Compacta com Auxilio de Análise Termica," *Fundição Vol. 257,* pp. 22-28, 2° e 3° trimestre 2010.

[66] V. Anjos, W. Baumgart, C. A. Silva Ribeiro, O. Kloetzen and J. Cunha, "The Modern Thermal Analysis Route to the Compact Graphite Iron Production," in *The Carl Loper Symposium*, Wisconsin - U.S.A., 2009.

[67] V. Anjos, C. A. Silva Ribeiro, W. Baumgart, F. Dias and J. Cunha, "Literature Survey on Porosity and Microporosity in Cast Irons Related to Expansion and Gas Entrapment Phenomena," *Key Engineering Materials Vol.457,* pp. 410-415, 2011.

[68] R. Hummer, "Beurteilung der Lunkerneigung von Gußeisen mit Kugelgraphit mittels Abkühl- und Längeänderungskurven," *Giesserei-Praxis Nr.9/10,* pp. 142-151, 1989.

[69] Z. Gedeonová, J. Dúl and S. Bódi, "Die Bewegung der Grenzfläche Metall/Form Wärend der Erstarrung von Gußeisen mit Kugelgraphit und Lamellengraphit," *Gießerei-Praxis Nr. 7/8,* pp. 150-155, 1996.

[70] W. Schmitz and S. Engler, "Ausdehnungsdrücke während der Erstarrung von Gußeisen mit Lamellen- und Kugelgraphit," *Giesserei 77 Nr.11,* pp. 372-375 , 28 Mai 1990.

[71] W. Schmitz and S. Engler, "Gestaltänderungen erstarrender Gußstücke in Sandformen - Teil 2," *Giesserei 74 Nr.20,* pp. 614-619, 28 September 1987.

[72] W. Schmitz and S. Engler, "Kunstharzgebundene Formen - Einfluß verschiedener Bindersysteme auf die Metallwand- und Formkastenbewegung," *Gießerei-Praxis Nr.7,* pp. 132-140, 1994.

[73] L. Bäckerud and B. Chalmers, *Trans. AIME Vol.245,* pp. 309-318, 1969.

[74] G. Chai, L. Arnberg and L. Bäckerud, Solidification Characteristics of Aluminum Alloys, Vol. 3: Dendrite Coherency, AFS - American Foundry Society, 1996.

[75] C. A. Silva Ribeiro, C. Sá, L. F. Malheiros, W. Baumgart, E. Wüller, M. Donhauser and C. Henke, "Relationship Between Image Analysis Graphite Shape Factors, Mechanical Properties and Thermal Analysis Solidification Behaviour of Compacted Graphite Cast Iron," in *Science and Processing of Cast Iron* , Beijing, P.R.China, 2006.

[76] J. Zhou, "Colour Metallography of Cast Iron - Chapter 1 Introduction (II)," *China Foundry,* vol. 6, no. 2, pp. 152-156, May 2009.

[77] ASK Chemicals Metallurgy GmbH, "SMW605 - Product data sheet," ASK Chemicals Metallurgy GmbH, October 2010.

[78] ASK Chemicals Metallurgy GmbH, “VP216 Product data sheet,” ASK Chemicals Metallurgy GmbH, October 2010.

Figure Index

Table Index

Attachment A: Test casting obtained for the trials from chapter 5.5.

Table 47 - Photographs from the cast castings poured for the trials presented in chapter 5.5

Sample Name	Casting photograph
LT_1	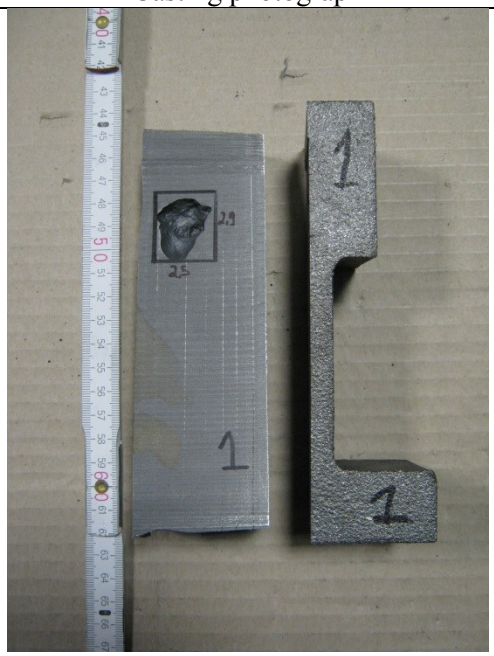
LT_2	

LT_9	
LT_12	

Attachment B: Test casting obtained for the trials from chapter 5.6.

Table 48 - Photographs from the cast castings poured for the trials presented in chapter 5.6

Sample Name	Casting photograph (the numbers written in the casting refers to the mound number given by the foundry when prepared the mounds, does not correspond to the sample name used in the report)
DC_1	 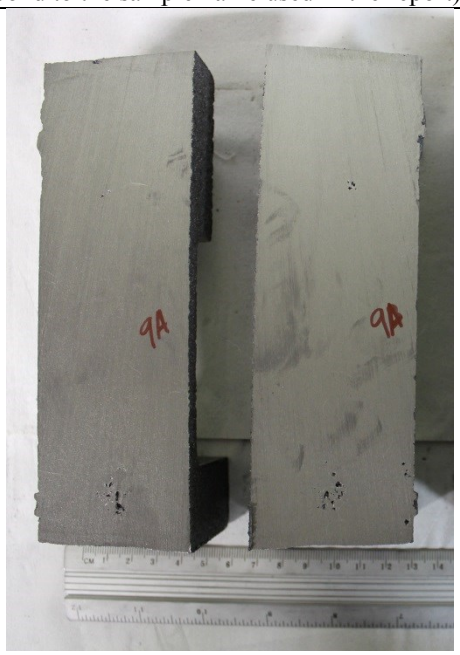
DC_2	 

DC_3	  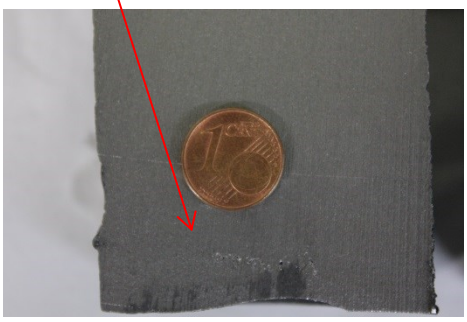

DC_4	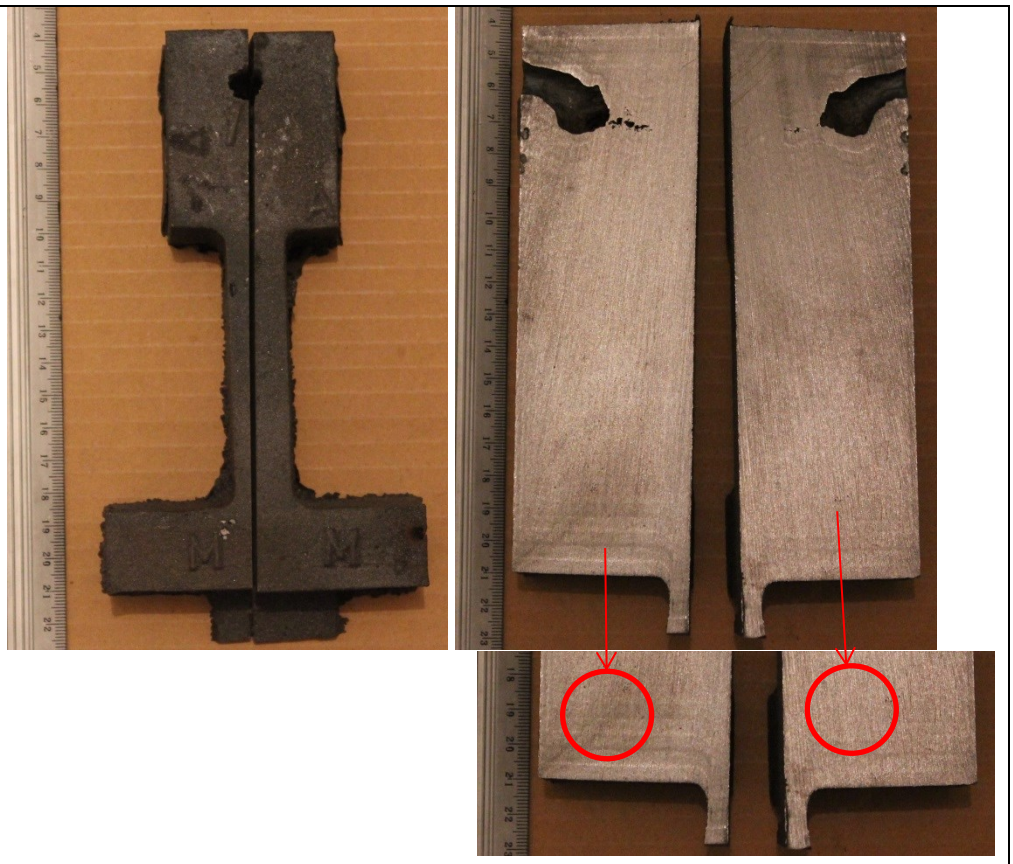
DC_5	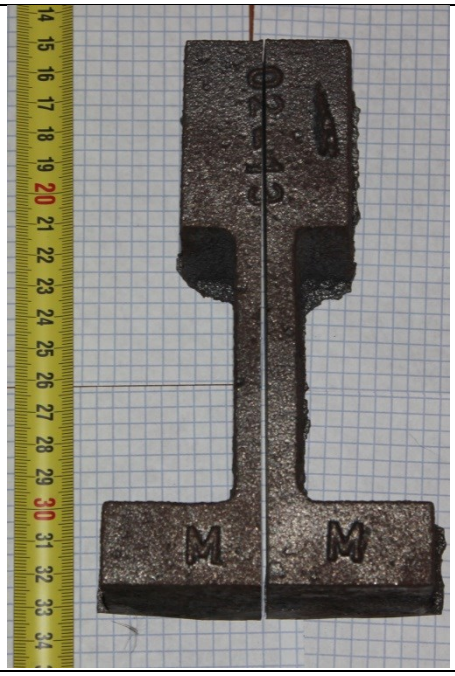

	
DC_6	 

DC_7	 
DC_8	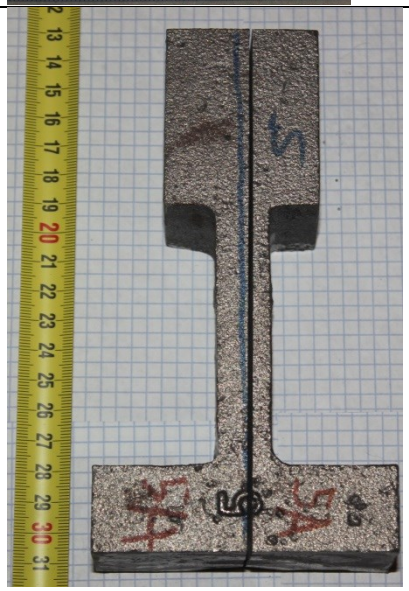 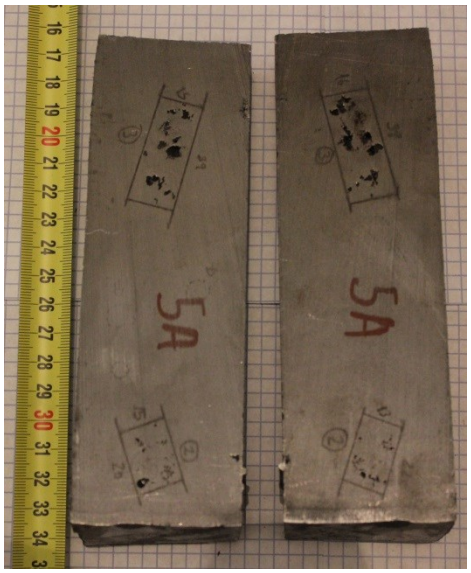

DC_9